Multiscale Modeling in Semiconductors: From Defect Formation to Device Performance

Yu Jin

A dissertation

submitted in partial fulfillment of the

requirements for the degree of

Doctor of Philosophy

University of Washington

2017

Reading Committee:

Scott Dunham, Chair

Manjeri Anantram

Marjorie Olmstead

Program Authorized to Offer Degree:

Electrical Engineering

University of Washington

Abstract

Multiscale Modeling in Semiconductors: From Defect Formation to Device Performance

Yu Jin

Chair of the Supervisory Committee:
Professor Scott T. Dunham
Electrical Engineering

This work is aimed to build a model framework to predict device performance based on the formation of defects in order to meet the demand for higher-performance integrated circuits and solar cells. We use a multiscale modeling technique to investigate the properties of some important defects. Those defects play important roles in the study of precipitation, diffusion and recombination in semiconductors. *Ab initio* (density functional theory, DFT) calculations are used to extract critical parameters at atomic scale and to verify key mechanisms, while continuum modeling is conducted to describe the defects' kinetics and interactions at device scale. Combining process/device simulation and the fundamental understanding at atomic scale, we can gain insight about how process conditions can affect defect formation and therefore

device performance. Thus, this multiscale modeling framework can provide useful guidance in performance optimization and cost reduction.

Based on this approach, we have developed models for carbon clustering and associated metal gettering, which can be used to reduce noise in advanced silicon CMOS image sensor. We have also advanced models for oxygen precipitation in silicon by considering morphology evolution, dynamic interactions with point defects, and doping dependency. The carbon and oxygen precipitation processes are modeled using the reduced moment-based model (RKPM) with improved computation efficiency.

The impact of charged grain boundaries on device performance, as well as electron beam induced current (EBIC) imaging measurement, of CdTe solar cell has been investigated in detail. Based on our simulation results, we propose that passivation with accumulated grain boundaries will be more beneficial to the performance of CdTe solar cell, while depleted grain boundaries generally degrade performance.

We also conduct a series of DFT calculations to investigate the light induced degradation (LID) related defects in silicon solar cell. Based on these calculations, a comprehensive model for light induced degradation is proposed which matches experimental observation under full range of conditions.

TABLE OF CONTENTS

LIST OF FIGURES

LIST OF TABLES

ACKNOWLEDGEMENTS

I must first express my deepest gratitude to my advisor, Professor Scott T. Dunham, for his excellent mentorship in the last several years. His wisdom and guidance have made me go through lots of challenges in my research and unfolded a new chapter for future career. He is always highly supportive to my professional and personal needs, allowing me to attend conferences and workshops, and to have flexibility to work remotely in China.

I would like to thank my committee members, Profs. Manjeri Anantram, Lih Lin, Marjorie Olmstead and Lucien Brush, for their valuable suggestions and assistance. Prof. Lih Lin was also my advisor for my first year of my PhD and I had great experience to work with and learn from her.

I also would like thank my extraordinary colleagues in the Nanotechnology Modeling Group (NTML) for their time, assistance and friendship: Wenjun Jiang, Renyu Chen, Bart Trzynadlowski, Daniel Mutter, Shifeng Zhu, David Sommer, Nate Hermann and Armin Yazdani. I also want to thank Prof. Daniel Gamelin and his group members, Pradip Chakraborty and Charles Barrows, for the fruitful discussion in the collaboration.

I'm lucky to have lots of friends in Seattle: Jingda Wu, Erin Sanehira, Chang-Ching Tu, Shifeng Zhu, Peifeng Jing, YunBo Liu, Xiongbo Peng, Hao Wu, Chen Zou, Danying Hu, Zhenni Wan, Renshu Gu, Jiayi Dou, Yuanyuan Shi, Yaxuan Zhou and Meng Zhong. Thanks to their help, I have wonderful experience in last several years.

Funding for my research was generously provided by Sony, the Silicon Wafer Engineering and Defect Science (SiWeds), the Semiconductor Research Corp. (SRC), Bay Area Photovoltaic Consortium (BAPVC) and NSF.

Most of all, I would like to express and love and gratitude to my parents in China, Baolin Jin and Lishu Peng, for their unconditional love and support.

Chapter 1. INTRODUCTION

Following the prediction by Gordon Moore in 1965, the feature size of transistors keeps shrinking exponentially over time [1-2]. The rapid scaling of transistor is one of the major driving sources for the rapid development of silicon technology in the last several decades. The industry is still trying to push the limits of scaling despite increasing difficulty. Device configurations change from bulk MOSFET, to thin body SOI FET [3-4] and FinFET [5], to recently gate-all-around (GAA) nano-sheet FET [6]. The processes to fabricate those devices become extremely complex and expensive. To optimize device performance and enhance yield, lots of issues need be considered, such as formation of ultra-shallow junction, defect engineering, strain engineering, parasitic capacitance and resistance, and reliability [7]. Technology computer aided design (TCAD) is a powerful technique to deal with those issues economically. For RF and power semiconductor devices, TCAD is also quite useful to optimize the switching property and on resistance by improving the device design. Coupled with optical simulation, TCAD can also play important roles in the photovoltaic industry by improving solar cell efficiency. Lots of continuum models are included in the commercial TCAD tools, such as Synopsys Sentaurus and Silvaco, but demand in the semiconductor for more accurate models, especially those with specific applications, is still very high and continues to grow.

Continuum process and device simulation are a very powerful method to study process and device physics at the macroscopic level, while *ab initio* calculation, such as density functional theory (DFT), can provide a theoretical basis at atomic level for higher level models. DFT calculation provide the initial guidance for continuum model development which can provide critical parameters and verify mechanisms for certain processes. We adopt the so-called “multiscale modeling” approach to apply important parameters obtained from *ab initio* calculations in continuum simulation in order to study certain systems as shown in Fig 1.1.

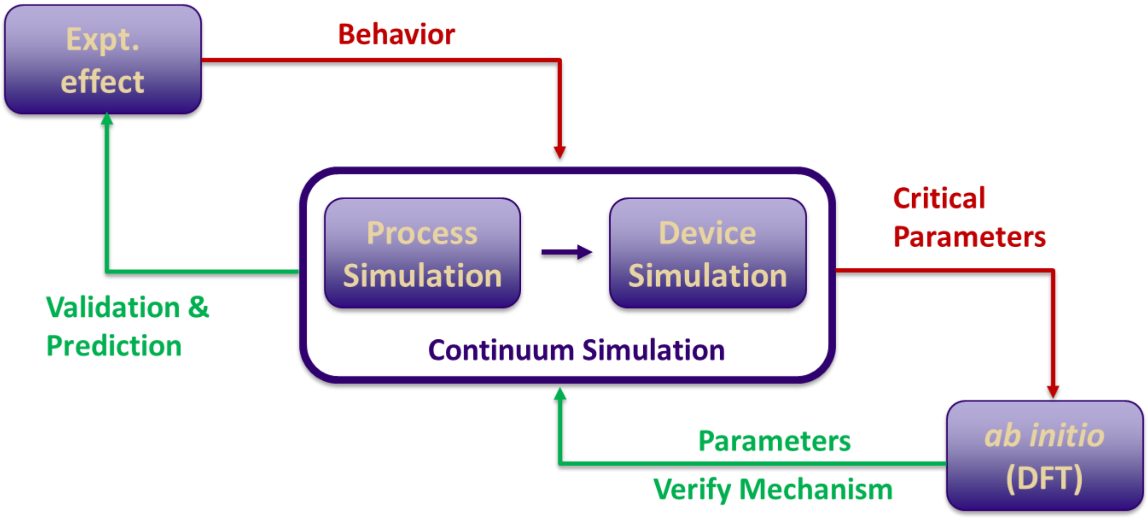

Figure 1.1. Schematic for multiscale modeling method.

Defects play important roles in semiconductors. For example, intrinsic point defects in silicon interact with dopants during their diffusion process [8-9]; interstitial oxygen helps to enhance the mechanical strength of silicon substrates [10]; extended defects can capture harmful metal impurities but can also cause slip and warpage [11]; oxygen vacancy migration is the key mechanism for resistive random-access memory (RRAM) [12]. The impact of defect formation on semiconductor device performance can be profound. So, we are aimed to develop a framework which can predict the device performance based on the defect formation.

The methodology we use is the “multiscale modeling” and the scope includes precipitation, diffusion and recombination. Within this scope we have studied different defects including carbon and oxygen precipitates in silicon, grain boundaries in CdTe solar cell, and light induced degradation (LID) related defects in silicon solar cell. Carbon and oxygen are two of the most common defects in silicon wafers. Understanding and modeling their precipitation processes is very challenging but quite useful for many applications, such as “internal gettering” [48]. Grain boundaries are the most important defects in polycrystalline semiconductors, such as CdTe. Understanding the impact of the grain boundaries on device performance is crucial for device optimization. The light induced degradation in silicon solar cell also involves the defect formation processes. Investigating these defects is very important for understanding the mechanism of LID and improving the solar cell performance.

Metals are usually detrimental impurities in devices, as they introduce traps that limit carrier lifetime. One important method used to remove metal impurities from device active region is called "gettering." There are different gettering methods, such as gettering by phosphorus diffusion and extended defects. One of the recent approaches for gettering is using carbon implantation. In Chapter 2, we have developed a moment-based carbon precipitation model based on *ab initio* calculations of the energetics of carbon interstitial clusters and silicon carbide precipitates. A metal gettering model is also built using results of DFT calculations for metal binding to carbon species in silicon. By combining process and device simulations, we can model the device performance of lifetime sensitive devices, such as CMOS image sensors.

Oxygen is unavoidably introduced in the growth of Czochralski silicon. Typically, oxygen concentrations from 10^{17}-10^{18}/cm^3 have been applied in modern IC fabrication processes. Such high concentrations of oxygen often lead to strong supersaturation and then precipitation during thermal processing. The impact of the resulting oxygen precipitates can be either beneficial or detrimental to device performance. In Chapter 3, we have developed a moment based precipitation model for oxygen with consideration of morphology evolution and dynamic incorporation of point defects. In addition, by including a boron/interstitial clustering model and Fermi level effects on point defect behavior, the impact of boron is also considered in modeling oxygen precipitation.

CdTe solar cells offer a low-cost way to reach high conversion efficiency. Chapter 4 shows our two-dimensional simulations of device structures that are typical in EBIC (Electron Beam Induced Current) imaging and solar cell structures for p-type CdTe absorber layers with charged grain boundaries. A large signal enhancement is found near positively-charged (depleted) grain boundaries in EBIC simulations, but, in contrast to previous claims [98-101], solar cell performance drops. In contrast, little EBIC contrast is seen, but the cell performance improves when negatively charged (accumulated) grain boundaries are introduced. We explore the impact of doping levels, lifetimes, and grain boundary charge to provide insights on designs that improve thin film solar cells' performance.

It has been long observed that the performance of Si solar cells degrades under initial exposure to light via a drop in bulk carrier lifetime. This phenomenon has been termed light induced degradation, and a wide range of models have been proposed to explain it, but none are fully satisfactory. In Chapter 5, we use DFT calculations to study the interaction of oxygen dimers with Ga and B and to verify the recombination mechanism for LID, and then propose a comprehensive model of light induced degradation of Si solar cells doped with B, Ga and P. The proposed model accounts for experimental observation under full range of conditions.

1.1 METHODOLOGY

We use multiscale modeling methods, combining *ab initio* calculations and continuum simulations, to study different semiconductors. This section is a brief overview of these two powerful methods.

1.1.1 *Density Functional Theory (DFT)*

Density functional theory provides an *ab initio* method to calculate material properties at atomic scale. It’s widely used in physics, chemistry and material science to solve many-electron problems. There are many different DFT codes available. For calculations in our study, we use the plane wave basis code VASP (Vienna *Ab-initio* Simulation Package) [13-14]. Here, we mainly go through the application of DFT to get important parameters that can be used in higher level simulation. A detailed discussion of DFT can be found in previous work [15-16].

1.1.1.1 Calculating the formation energy

DFT can be used to obtain the formation energy of defects. A simple example is extracting the formation energy of native point defects from DFT calculations within a size-64 silicon supercell as follows:

$$E_V^f = E_V - \left(E_{Si64} - \frac{1}{64} E_{Si64} \right) \tag{1.1}$$

$$E_I^f = E_I - \left(E_{Si64} + \frac{1}{64} E_{Si64} \right) \tag{1.2}$$

Here, E_V^f and E_I^f represent the formation energy of vacancy and interstitial respectively. E_V and E_I are the calculated total energies for supercells containing vacancy (63 Si atoms) and interstitial (65 atoms), and E_{Si64} is the energy for supercell of perfect bulk structure. The larger the formation energy here implies it costs more energy to form the defect.

1.1.1.2 Calculating the binding energy

Binding energy is an important parameter to describe the reaction between different species. The binding energy between A and B, $E_{A/B}^b$, can be calculated in DFT as:

$$E^{b}_{A/B} = E_{AB} + E_{Si64} - E_{A} - E_{B} \quad (1.3)$$

where E_X is the total energy of defect X in the supercell. Large (negative) binding energy indicates that there is a substantial driving force for the AB complex to form. Binding energy calculations are widely used in cluster formation and metal gettering models. It's also useful to study the interactions between different impurities.

1.1.1.3 Calculating the migration barrier

The migration barrier is the key parameter for both diffusion and defect structure reconfiguration. The approach to get the migration barrier in VASP is called the *nudged elastic band* (NEB) method [17-18]. In the simulation, the initial state, final state, and intermediate configuration which is based on the interpolation between initial and final states are defined. The method works by optimizing a number of intermediate states along the reaction path, which can help identify the transition state and associated barrier energy.

1.1.1.4 Identifying a localized defect

Charge density is an important output of the DFT calculation. By comparing the charge density difference between a defect's two charge states, we can determine whether the defect is a localized defect. If the charge density difference distribution in the system is almost uniform, the defect should be non-localized defect as can be seen in Figure 1.2 where substitutional boron (B_S) in silicon works as a shallow acceptor but not a localized defect. For localized defects, the charge density difference should be localized around the defect which indicates the defect can effectively capture carriers as shown in Figure 1.3 where iron interstitial (Fe_i) in silicon works as trap center for recombination. In the calculation of charged systems, a neutralizing background charge is assumed by VASP as required for convergence.

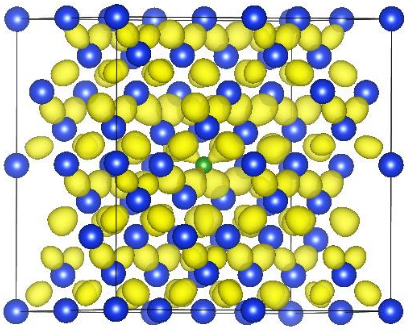

Figure 1.2. Charge density difference between B_S^0 and B_S^- in silicon. Example for non-localized defect. The green atom in the center is boron and the blue atoms are silicon. The iso-surfaces for charge density difference are yellow (positive).

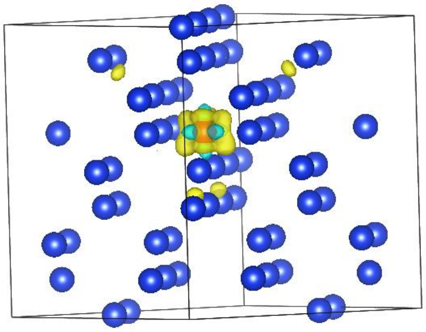

Figure 1.3. Charge density difference between Fe_i^+ and Fe_i^0 in silicon. Example for localized defect. The red atom in the center is iron. The iso-surfaces for charge density difference are yellow (positive) and cyan (negative).

1.1.1.5 The reliability of DFT calculations

There are some limitations of DFT calculations which have been discussed in detail in Refs. [134-136]. For example, DFT tends to underestimate the bandgap for semiconductors and insulators. It also neglects strong correlations and van-der Waals interactions. For the DFT calculation in silicon using VASP specifically, the situation is reasonably optimistic. Depending on the pseudo-potential we choose, the calculated bandgap has about a 10 percent difference (~0.1 eV) from the experimental value. The error in the bandgap calculation impacts the accuracy of the defect level calculation. Other DFT calculation errors may come from small supercell size. Because the calculation uses a periodic boundary condition, the interaction between defects and their images introduce calculation errors. The error for Si/SiC interface energies introduced by using different supercell size (slab size) has been calculated in Ref. [44], which indicates that there is up to a 15 percent error in the interface energy calculation when using a small slab size (e.g., 5 layers SiC/5 layers Si).

1.1.2 *Continuum simulation*

1.1.2.1 Process simulation

Process simulation uses a continuum method to study defect formation kinetics and distribution in a device at a given process condition (time-temperature profile). The defects evolution and redistribution are described by a set of continuity equations. The following equation is an example of a continuity equation for a specific defect, A.

$$\frac{\partial C_A}{\partial t} = -\nabla \bullet J_A + R_A^{+} - R_A^{-} \tag{1.4}$$

Here J_A is the flux of A including the contributions from both drift and diffusion, which is meaningful only for mobile species. R_A^{+} and R_A^{-} are generation rates and consumption rates for A.

For a specific reaction,

$$A + B \Leftrightarrow AB, \tag{1.5}$$

the reaction rate can be expressed by:

$$R_{A/B} = 4\pi a\left(d_A + d_B\right) \times \left(C_A C_B - \frac{C_{AB}}{K^*}\right) \tag{1.6}$$

Here a is the capture distance depending on the geometry of the defects, d_A and d_B are the defects' diffusivities, and C_X is the concentration of a species X. K^* is the equilibrium constant for the reaction which depends on the binding energy as:

$$K^* = \frac{\theta}{C_s} \exp\left(-E^b / k_B T\right) \tag{1.7}$$

where C_s is the density of matrix atoms (5×10^{22} cm^{-3} for silicon), and θ is the number of possible configurations per lattice site to form AB complexes.

1.1.2.2 Device simulation

Device simulation describes the behavior of electron and holes in device, which can be used to extract the overall electrical characteristics for the device. The bases for device simulation are Poisson's equation and the continuity equations [19]. Poisson's equation correlates the electrostatic potential with charge distribution:

$$\nabla^2 \Phi = \frac{-q\left(p - n + N_D^{\ +} - N_A^{\ -}\right)}{\varepsilon} \quad \text{with } E = -\nabla\Phi \tag{1.8}$$

Here Φ is the electrostatic potential, E is the electrical field, q is the electron charge, ε is the dielectric constant of material, p/n are the hole/electron concentrations, and N_D^+/N_A^- is the concentration of the ionized donor/acceptor.

Continuity equations describe the change rate of carrier concentrations, which is composed of the difference between flux in and flux out (flux gradient), and the difference between generation (G) and recombination (R) (net generation rate):

$$\frac{dn}{dt} = \frac{1}{q} \nabla \bullet J_n + G - R \tag{1.9}$$

$$\frac{dp}{dt} = -\frac{1}{q} \nabla \bullet J_p + G - R \tag{1.10}$$

The carrier transport depends on drift and diffusion as expressed by:

$$J_n = q\left(\mu_n nE + D_n \nabla n\right) \tag{1.11}$$

$$J_p = q\left(\mu_p pE - D_p \nabla p\right) \tag{1.12}$$

Here μ_n and μ_p are motilities for electrons and holes, and D_n and D_p are diffusivities for each. The relationship between mobility and diffusivity can be described by the Einstein relation:

$$D = \frac{kT}{q}\mu \tag{1.13}$$

There are three basic types of carrier recombination mechanisms, as discussed in Section 1.2.3.

1.2 SCOPE

Using a multiscale modeling method, we have studied different systems. The core problems we investigated can be summarized as precipitation, diffusion and recombination.

1.2.1 *Precipitation*

Precipitation is a kind of phase transformation where a separate phase is formed in a solution (matrix material). The formation of rain droplets is an example of precipitation where the liquid phase forms in water vapor. Similarly, in a solid, such as semiconductor, certain species can also diffuse and precipitate; oxygen and copper precipitation are common examples.

Precipitation has been investigated in detail using the classical kinetics of phase transformation theory [20]. The essential driving force for precipitation is the difference in the free energies of the initial and final configurations. The change in free energy, ΔG, when adding an atom, A, from a solution into a very large precipitate is:

$$\Delta G = \Delta G_p - k_B T \ln\left(\frac{C_A}{C_s}\right) \tag{1.14}$$

where ΔG_P is the formation energy including enthalpy and entropy components. The second term is the entropy of mixing which depends on the concentration of a solute, $C_{A,}$ and the sites it can occupy, C_s. If $\Delta G>0$, a precipitate will shrink; if $\Delta G<0$, precipitates will tend to grow together with a decrease of the solute concentration until $\Delta G=0$. The critical concentration for $\Delta G=0$ is the solid solubility, C_{SS}, which is the concentration of solute in the presence of a very large precipitate:

$$C_{SS} = C_s \exp(\frac{\Delta G_P}{k_B T}) \tag{1.15}$$

The solid solubility is the saturation concentration the solute can reach. If exceeded, precipitates will eventually form.

ΔG_P is the energy cost to add an atom to a very large (infinite) precipitate. In considering small precipitates, we also need to consider the surface energy or strain energy for precipitation in real system. The free energy change upon forming a size n precipitate can be expressed as:

$$\Delta G_n = -nk_B T \ln\left(\frac{C_A}{C_S}\right) + n\Delta G_P + \Delta G_n^{exc} = -nk_B T \ln\left(\frac{C_A}{C_S}\right) + \Delta G_n^f \tag{1.16}$$

where ΔG_n^{exc} is the excess energy including surface energy and strain energy and ΔG_n^f is the precipitate formation energy. Surface energy and strain energy both increase monotonically with size. The surface energy for a spherical precipitate is proportional to $n^{2/3}$ and for a disk-shaped precipitate is proportional $n^{1/2}$. The strain energy is normally proportional to n or n^2.

Combining the definition of solid solubility in Equation (1.15), the above equation can be expressed as:

$$\Delta G_n = -nk_B T \ln\left(\frac{C_A}{C_{SS}}\right) + \Delta G_n^{exc} \tag{1.17}$$

When $C_A < C_{SS}$, $\Delta G_n>0$ and the formation of a precipitate is energetically unfavorable. When the solute become supersaturated ($C_A > C_{SS}$), the energy tends to be reduced and precipitation is likely to occur. If we plot the energy against *n* as shown in Figure 1.4, we find the energy may increase first until the critical size, n_c, and then decrease. Thus, small precipitates ($n<n_c$) tend to shrink and large precipitates ($n<n_c$) tend to grow. For a supersaturated solute, though the energy in a large precipitate is smaller than dissolved atoms, it needs to overcome an activation barrier because the interface energy is dominant in small precipitates.

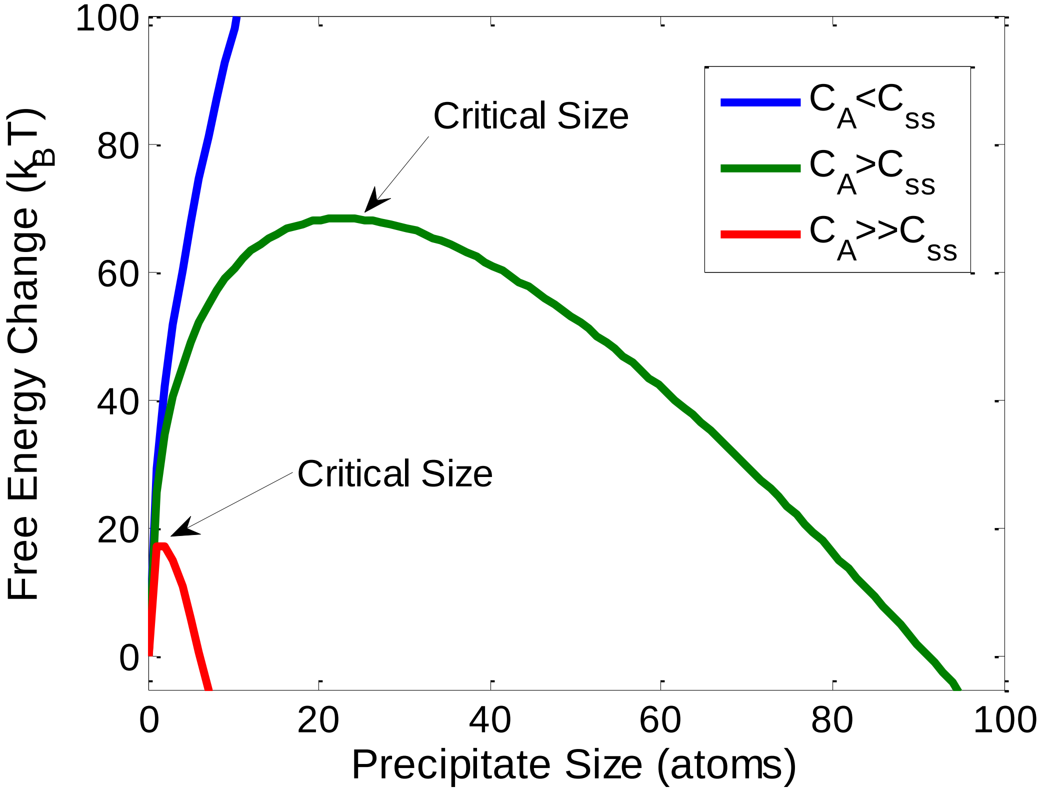

Figure 1.4. Free energy change at different solute concentrations for the formation of planar precipitates.

The classical model for precipitation is the nucleation and growth model [20]. The models can capture basic physics reasonably well but may not account for certain situations, such as *Ostwald ripening*. In Chapter 2 and 3, we try to develop a more accurate precipitation model using the kinetic rate equations. Our precipitation model involves a comprehensive understanding of a complex dynamic system, where we consider the interaction with point defects, the impact of strain and the evolution of morphology. In addition, a moment based model is developed to improve computational efficiency.

1.2.2 *Diffusion*

Diffusion is the movement of molecules, atoms or carriers driven by a concentration gradient. The study of diffusion in solids is very important for understanding the current of carriers, the distribution of dopants and the interaction between impurities. There are two types of diffusion: self-diffusion and impurity diffusion. We focus on the diffusion of impurities in this section.

In a macroscopic scope, we can describe the diffusion process using Fick's laws. Fick's first law describes the diffusion flux (J_X) depending on the gradient of concentration (C_X):

$$J_X = -D_X \nabla C_X \tag{1.18}$$

where D_X is the diffusion coefficient, the diffusivity. Fick's second law describes the change rate of the concentration due to the diffusion:

$$\frac{\partial C_X}{\partial t} = D\nabla^2 C_X \tag{1.19}$$

For a better understanding of diffusion, the atomic diffusion picture is often necessary. Impurities must overcome an energy barrier to diffuse, which is called the migration barrier, $E_X{}^m$, as illustrated in Figure 1.5. The rate of hopping, $v_X{}^m$, depends on the attempt frequency, v^0, and activation barrier:

$$v_X^m = v^0 \exp\left(\frac{-E_X^m}{k_B T}\right) \tag{1.20}$$

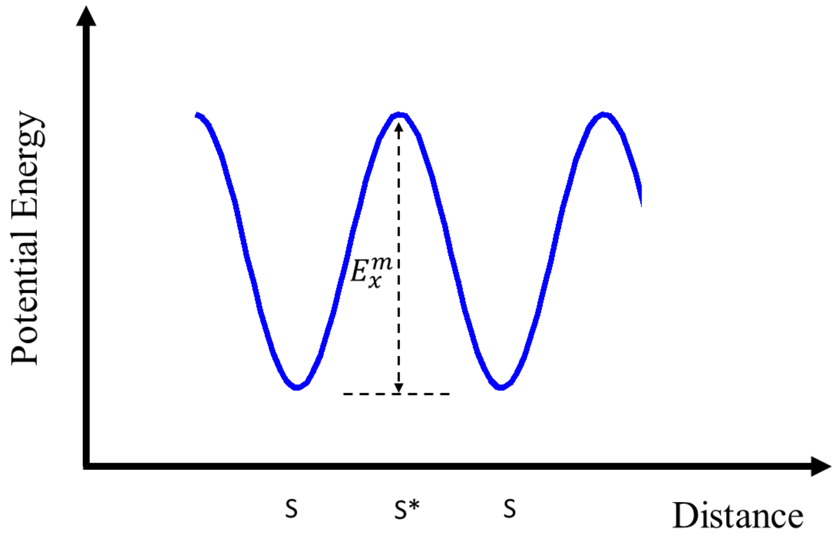

Figure 1.5. Schematic for migration barrier.

The attempt frequency has relatively weak dependency on temperature and is on the order of 10^{13}/s.

Diffusivity is proportional to hopping frequency:

$$D_X = \lambda^2 v_X^m / 6 = D_X^0 \exp\left(-Q_X / k_B T\right) \tag{1.21}$$

where λ is the hopping distance between two energy minima; 6 is used here for a three-dimensional system. D_X^0 and Q_X can be obtained by fitting the experimental data in the Arrhenius plot, where we plot diffusivity in logscale vs 1/T.

Diffusion is normally mediated by point defects, interstitials and vacancies. Vacancies are empty lattice sites and interstitials are atoms situated between (or sharing) lattice sites as shown in Figure 1.6.

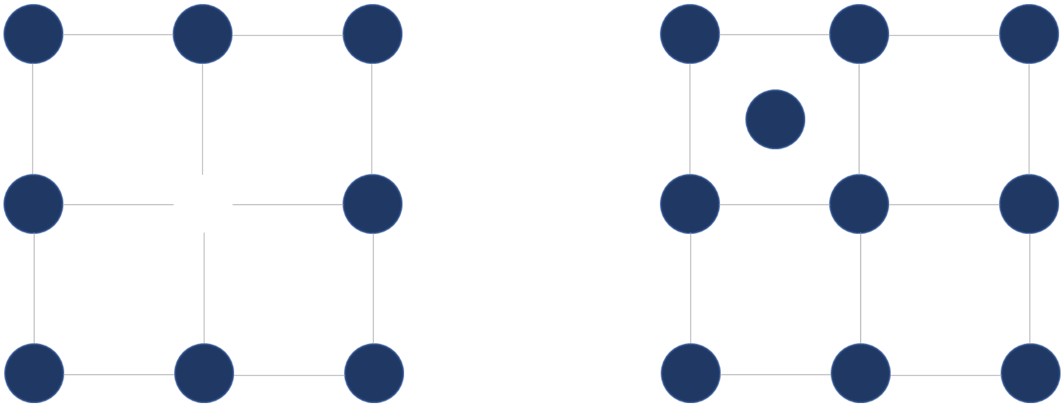

Figure 1.6. Schematic of a vacancy (left) and interstitial (right) in a simple cubic lattice

The self-interstitial may kick out a substitutional dopant from it lattice site and make it easier to diffuse in the relatively open channels. After diffusing for a certain distance, the interstitial dopant may come back to the lattice site by kicking out a substitutional lattice atom or finding a vacancy. This is called the “kick-out” mechanism. It can also be possible that a dopant atom and self-interstitial may form a pair and migrates as a mobile species. This is called interstitialcy mechanism; however, both mechanisms are mathematically identical and are together called interstitial mediated diffusion [21] (Figure 1.7). In Ref. [22], the NEB calculation is conducted in VASP to find the overall diffusion barrier for both the kick-out and interstitialcy mechanisms for the diffusion of phosphorus in silicon.

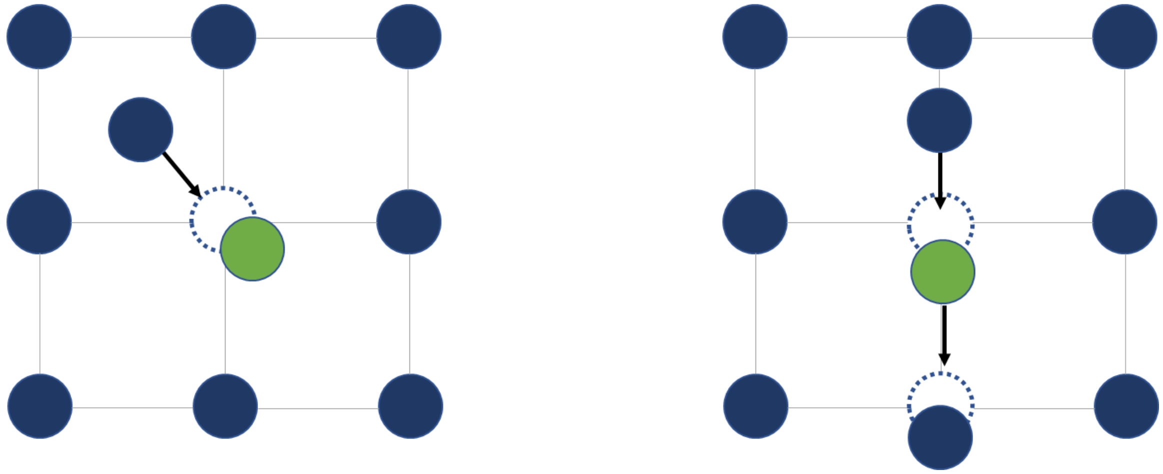

Figure 1.7 Schematic of interstitial mediated diffusion. The left is the kick-out mechanism the right is the interstitialcy mechanism.

The simplest vacancy diffusion mechanism is the direct exchange between vacancy and dopant, which is also called uncorrelated diffusion. The other important vacancy diffusion mechanism is the ring mechanism, where the dopant and vacancy pair must dissociate to the third-nearest neighbor to have long range migration in silicon as shown in Figure 1.8 [23]. Ref. [24] shows the DFT calculation results for the migration barrier of the ring mechanism for arsenic diffusion in silicon.

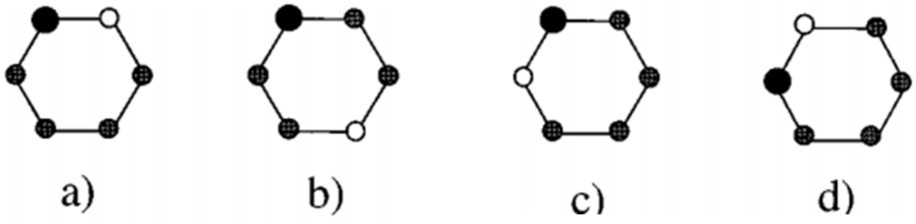

Figure 1.8. Schematic of impurity-vacancy migration on a diamond lattice via ring mechanism. The filled circle represents the impurity, and the empty circle is the vacancy. The starting configuration is (a) and then the vacancy moves to the third-nearest-neighbor site as shown in (b). (c) shows vacancy approaches the impurity from the new direction, allowing the impurity to migrate as shown in (d). Reproduced from Ref. [24].

The other important diffusion mechanism is the dissociative mechanism first proposed by Frank and Turnbull. In this mechanism, the substitutional atom can dissolve into a vacancy and an interstitial impurity, which drives the diffusion.

Since diffusion is normally mediated by point defects, the interaction between point defects and dopants or other impurities are very important to model diffusion. In Chapter 2, we present a carbon precipitation model with co-implanted boron. Since boron mostly diffuses via interstitials, the reduction of interstitial concentration by carbon precipitation reduces the diffusion of boron. Carbon also relies on interstitial to diffuse, so the carbon diffusion and carbon precipitation would compete during the annealing after implantation.

In Chapter 5, we report a diffusion mechanism for oxygen interstitial dimer (O_{2i}), where the bi-stability of the O_2 dimer at different charge states plays an important role. By capturing electrons and holes, the oxygen dimer can change between staggered and square structure. The enhanced reconfiguration frequency with assistance of carrier capture will greatly increase the mobility of the oxygen dimer.

1.2.3 *Recombination*

Recombination in semiconductors is a process where electrons and holes annihilate each other. Recombination can be classified into three types: direct recombination, Auger recombination and indirect recombination through trapping level.

1.2.3.1 Direct Recombination

Direct recombination is often referred to band-to-band recombination, and occurs when a conduction band electron and valence band hole annihilate each other. Depending on whether there is photon emission in the process, direct recombination can be either radiative recombination or non-radiative recombination. Direct recombination is efficient in direct bandgap materials such as GaAs. In an indirect bandgap material, such as silicon, direct recombination is much slower because it requires the involvement of phonons.

1.2.3.2 Auger Recombination

Auger recombination occurs when excess energy after recombination of an electron and a hole is transferred to a third carrier. Auger recombination can be considered the inverse of impact ionization. Auger recombination is also non-radiative recombination, and is most important when the carrier concentration is very high.

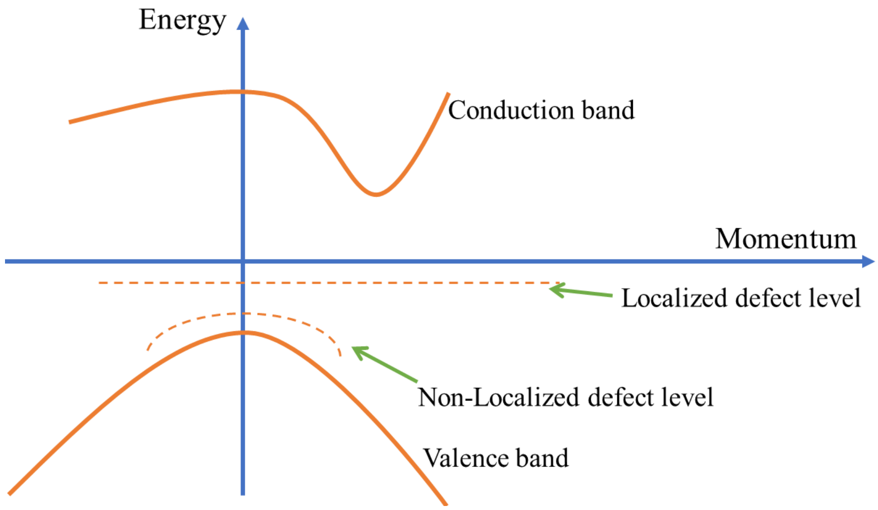

Figure 1.9. Schematic for localized defect and non-localized defect.

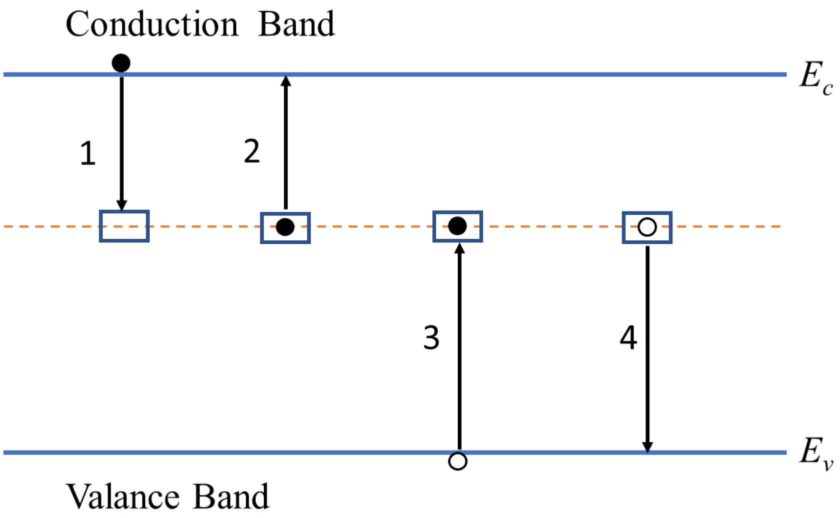

Figure 1.10. Schematic for trap assisted recombination.

1.2.3.3 Indirect Recombination through trapping level

In Section 1.1.1, we discussed how to use a DFT calculation to distinguish between localized defect and non-localized defects. The difference between the defect levels is shown in Figure 1.9. For an indirect bandgap material, such as silicon, electrons and holes can recombine when a localized defect of uniform energy in a wide momentum space captures both. Figure 1.10 is an example of a defect with trap level in the bandgap to capture electrons and holes. There are four processes involved in the recombination-generation process: 1) electron capture, 2) electron emission, 3) hole capture and 4) hole emission. R_1- R_4 are used to represent their rates, respectively:

$$R_1 = V_{th}\sigma_n n N_t \left(1 - f_t\right) \tag{1.22}$$

$$R_2 = V_{th}\sigma_n n_i \exp\left(\frac{E_t - E_i}{kT}\right) N_t f_t \tag{1.23}$$

$$R_3 = V_{th}\sigma_p p N_t f_t \tag{1.24}$$

$$R_4 = V_{th}\sigma_p n_i \exp\left(\frac{E_i - E_t}{kT}\right) N_t \left(1 - f_t\right) \tag{1.25}$$

Here, $V_{th} \sim 10^7 cm/s$ is the thermal velocity of carriers, σ is the capture cross-section, E_t is the trap level, E_i is the intrinsic Fermi level, and f_t is the probability of electron occupation in the trap level, given by Fermi-Dirac statistics in equilibrium:

$$f_t = \frac{1}{1+\exp\left(\frac{E_t - E_f}{k_B T}\right)} \tag{1.26}$$

with E_f as the Fermi level.

In a steady state with light illumination exciting electron and hole pairs, the number of electrons and holes are constant:

$$G_L = R_1 - R_2 = R_3 - R_4 \tag{1.27}$$

where G_L is the generation rate. Combining Equations 1.22 to 1.27, we can solve the net recombination rate $U=R_1-R_2$ as:

$$U = \frac{pn - n_i^2}{\tau_p\left(n + n_i \exp\left(\frac{E_t - E_i}{k_B T}\right)\right) + \tau_n\left(p + n_i \exp\left(\frac{E_i - E_t}{k_B T}\right)\right)} \tag{1.28}$$

with $\tau_p = \left(V_{th}\sigma_p N_t\right)^{-1}$ and $\tau_n = \left(V_{th}\sigma_n N_t\right)^{-1}$. Equation 1.28 is named the Shockley-Read-Hall (SRH) recombination equation

In Chapter 2, we have developed a carbon clustering model for metal gettering that removes harmful metal impurities in CMOS image sensors. The metal impurities work as trap centers for recombination and removing metal impurities can help reduce the dark current for the photodiode. In Chapter 4, we use SRH recombination to analyze the impact of charged grain boundaries on CdTe solar cell performance.

Ref. [26] proposes a recombination mechanism for bi-stable structures, oxygen dimer and boron/oxygen dimer clusters to study the origin for light induced degradation for boron doped silicon solar cells. In Chapter 5, we further investigate this problem and find that the recombination mechanism in Ref. [26] neglects the fact that the steady state concentration of recombination centers is dependent on the injection level. Also in Chapter 5, we propose and discuss in detail a comprehensive model to match a wide range of experimental observations.

.

Chapter 2. CARBON CLUSTERING AND ASSOCIATED METAL GETTERING

Carbon is an important defect in silicon introduced during crystal growth. There is great interest in the study of carbon kinetics because carbon can work as an effective trap for silicon self-interstitial. Introducing a high concentration of carbon (> 10^{18}cm^{-3}) leads to the undersaturation of silicon self-interstitial, which reduces boron diffusion. This effect can be used to reduce the transient enhanced diffusion (TED) of boron after implantation [27]. Also, the reduction of interstitial will result in the less formation of boron interstitial clusters (BICs) which increases boron activation.

The other important application of carbon is carbon implantation which has significant potential for reduction of dopant diffusion [28-30] and proximity gettering [31-33] for low thermal budgets and SOI structures. In this chapter, we present a carbon clustering/precipitation model and calculations and models for metal gettering by carbon clusters. We consider a range of small C/I clusters and a moment-based precipitation model to describe precipitation of larger SiC precipitates. The energetics of C/I clusters are based on DFT calculations. This chapter is adapted from a publication in 2014 ECS transaction [34].

2.1 CARBON PRECIPITATION MODEL

In our model, substitutional carbon (C) is assumed to be immobile and carbon can only diffuse as carbon/silicon interstitial pair (CI) or carbon/vacancy pair (CV). For carbon diffusion and small clusters formation, the following reactions are considered:

$$C + I \leftrightarrow CI \tag{2.1}$$

$$C + V \leftrightarrow CV \tag{2.2}$$

$$CI + V \leftrightarrow C \tag{2.3}$$

$$CV + I \leftrightarrow C \tag{2.4}$$

$$CV + CI \leftrightarrow 2C \tag{2.5}$$

The binding energies of C/I and C/V and their diffusivities will be discussed in the following section.

Since SiC (0.0209 nm^3) has nearly the same volume per silicon atom as Si (0.0203 nm^3) based on our DFT calculation, SiC precipitate formation requires the incorporation of roughly one interstitial per carbon (or silicon). To simplify the model, we keep the ratio of interstitials to carbon incorporated equal to 1 and neglect the strain energy for the precipitate. Thus, since CI pairs dominate the diffusion of carbon, we can consider carbon precipitation as the aggregation of CI complexes. The following reactions are considered:

$$CI + CI \leftrightarrow C_2 I_2 \tag{2.6}$$

$$C_2 I_2 + CI \leftrightarrow C_3 I_3 \tag{2.7}$$

$$\ldots$$

$$C_n I_n + CI \leftrightarrow C_{n+1} I_{n+1} \tag{2.8}$$

$$\ldots$$

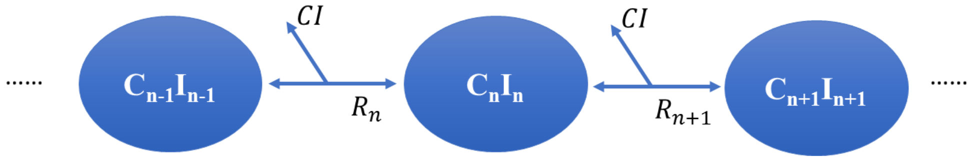

Figure 2.1. The schematic for the formation of carbon precipitation.

CI pairs aggregate to form C_nI_n complexes and then continue to grow or dissolve one carbon atom at a time as shown in Figure 2.1. The system can be described by kinetic rate equations as follows:

$$\frac{\partial[C_nI_n]}{\partial t} = R_n - R_{n+1} \qquad n = 2,\ 3\ldots\ \ldots \tag{2.9}$$

Here [C$_n$I$_n$] is the concentration of C$_n$I$_n$ and R_n is expressed as the difference between growth rate and dissolution rates:

$$R_n = g_{n-1}[C_{n-1}I_{n-1}] - d_n[C_nI_n] \tag{2.10}$$

where g_n is the growth rate from size n to n+1 and d_n is the dissolution rate from size n to n-1. The expressions for diffusion limited growth and dissolution rate are:

$$g_n = \lambda_n D_{CI}[CI] \tag{2.11}$$

$$d_n = g_{n-1}\exp\left(\frac{\Delta G_n - \Delta G_{n-1}}{k_BT}\right) = \frac{g_{n-1}}{[CI]}C_{ss}^{CI}\exp\left(\frac{\Delta G_n^{exc} - \Delta G_{n-1}^{exc}}{k_BT}\right) \tag{2.12}$$

$$\begin{aligned}\Delta G_n &= -nk_BT\ln\left(\frac{[CI]}{C_s}\right) + \Delta G_n^f = -nk_BT\ln\left(\frac{[CI]}{C_s}\right) + n*\Delta G_p + \Delta G_n^{exc}\\ &= -nk_BT\ln\left(\frac{[CI]}{C_{ss}}\right) + \Delta G_n^{exc}\end{aligned} \tag{2.13}$$

Here, λ_n is the kinetic factor depending on the geometry of the precipitates and interface reaction rate (in this work, SiC precipitates are modeled as spheres). D_{CI} is the diffusivity of CI. ΔG_n is the change in free energy when forming the size n precipitates from n *CI* pairs. ΔG_n^f is called the precipitate formation energy, ΔG_p is the energy change on adding CI in infinite precipitate (SiC), and ΔG_n^{exc} is the excess energy including the formation energy of interface and strain terms. C_{ss} is the solid solubility of CI. The derivation for growth and dissolution rates can be found in Appendix A.

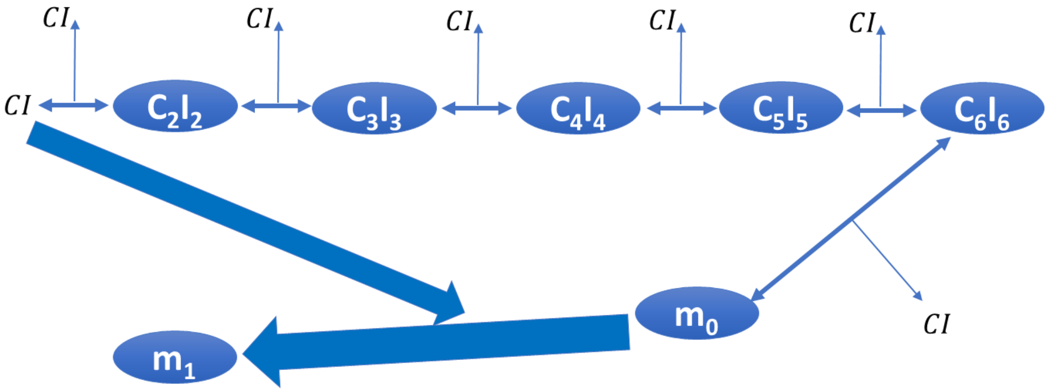

Figure 2.2. The schematic of moment based precipitation model (RKPM) for carbon.

We use a reduced kinetic precipitation model (RKPM) to describe carbon precipitation, where only the moments of large clusters are considered [35-37]. We consider clusters up to size 6 with discrete rate equations and those with 7 or more carbon atoms as part of the distribution to be captured by its moments, as illustrated in Figure 2.2. The resulting expressions for moment evolution are given by:

$$m_i = \sum_{n=7}^{\infty} n^i * [C_n I_n] \tag{2.14}$$

$$\frac{\partial m_0}{\partial t} = R_7 \tag{2.15}$$

$$\frac{\partial m_1}{\partial t} = 7 * R_7 + d_7 * [C_7 I_7] + D_{CI} m_0 * ([CI] * \gamma_2 - \gamma_3) \tag{2.16}$$

$$\gamma_2 = \frac{g_{n_{avg}}}{D_{CI}[CI]} \tag{2.17}$$

$$\gamma_3 = \frac{d_{n_{avg}}}{D_{CI}} \tag{2.18}$$

where m_i is the *i*th order of moment for precipitate distribution and n_{avg} is the average size of carbon precipitates with the definition:

$$n_{avg} = \frac{m_1}{m_0} \tag{2.19}$$

In the equations about, m_0 stands for the total density of large carbon cluster ($n \geq 7$), and m_1 stands for total carbon in the large carbon clusters. The changing rate of m_0 only depends on R_7, the difference between growth of C_6I_6 and the dissolution of C_7I_7. The changing rate of m_1 depends on R_7 and the interaction between CI and large carbon clusters. The delta function approximation is used for derivation in the model where the behavior of precipitates is assumed to be given that for the average size: [38]

$$[C_nI_n] = m_0 \cdot \delta\left(n - n_{avg}\right) \tag{2.20}$$

In the end, we can obtain the differential equation for CI by considering all the related species together:

$$\frac{\partial [CI]}{\partial t} = D_{CI} \nabla^2 [CI] - \frac{\partial m_1}{\partial t} - \sum_2^6 n \frac{\partial [C_nI_n]}{\partial t} + R_{C/I} - R_{CI/V} - R_{CI/CV} \tag{2.21}$$

where $R_{C/I}$, $R_{CI/V}$ and $R_{CI/CV}$ are reaction rates for C/I, CI/V and CI/CV binding, respectively.

Because the time dependent concentration of C_7I_7 cannot be solved directly within the delta function approximation, we use an empirical expression to estimate it. The estimator is obtained by investigating a wide range of experimental condition using the full kinetic precipitation equations and finding the relationship between C_7I_7, m_1 and m_0. We find the following estimator works well:

$$[C_7I_7] = \left[\left(\frac{n_{avg}}{7} \right)^{a_1} + \frac{{n_{avg}}^{a_2}}{\exp(b_2)} \right] * m_0 \tag{2.22}$$

where we choose $a_1 = -5.0$, $a_2 = -1.0$ and $b_2 = 7.0$ by comparing to solutions of the full set of kinetic rate equations under typical annealing conditions.

2.2 DFT CALCULATION

2.2.1 *Energetics of Small Carbon Clusters and Precipitates*

The energies for small carbon clusters were determined by DFT calculation using VASP. In our calculations, a 64-atom supercell with an energy cutoff of 340 eV and 2^3 Monkhorst *k*-point sampling method with generalized gradient approximation (GGA) were used. The calculated binding energy for C/V is 0.43 eV, and for C/CI is 1.48 eV. The properties for point defects and carbon diffusion we used are listed in Table 2.1, along with citations to the experiments on which they are based. The binding energy of CI in the table (1.61 eV) is from direct calculation using the experimentally-derived parameters in the upper part of the table, and is close to our DFT calculation result of 1.75eV. Since CI pair diffusion dominates in the carbon diffusion process, the diffusion of CV pairs has minimal impact. We use D_V as the diffusivity of CV pair.

Table 2.1. Prefactors and activation energies for point defects and carbon diffusion in our simulation

Parameters	D_0, C_0	E_m, E_f (eV)	**Ref.**
D_I	8.10×10^1 cm^2/s	0.9	[39]
C_I^*	9.16×10^{22} cm^{-3}	3.78	[39, 40]
D_V	1.00×10^{-4} cm^2/s	0.43	[39]
C_V^*	3.17×10^{28} cm^{-3}	4.43	[39, 40]
D_{C_s}	0.95 cm^2 /s	3.04	[41]
$C_{C_s}^*$	4×10^{24} cm^{-3}	2.3	[42]
d_{CI}	0.44 cm^2/s	0.87	[43]
C_{C_I}	8.64×10^{24}	4.47	
k_{C_I}	0.86	1.61	

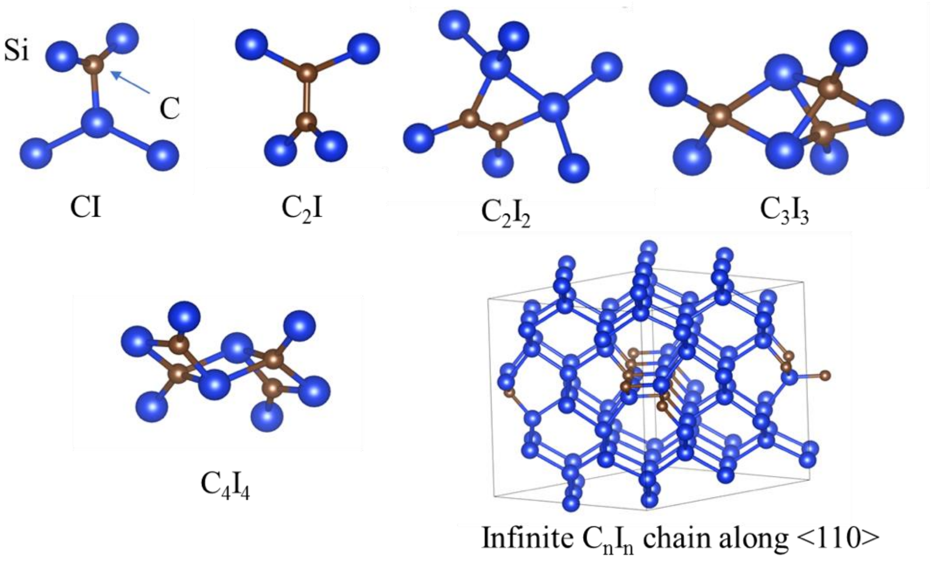

Figure 2.3. Some examples of most energetic favorable small carbon clusters structure obtained by using VASP

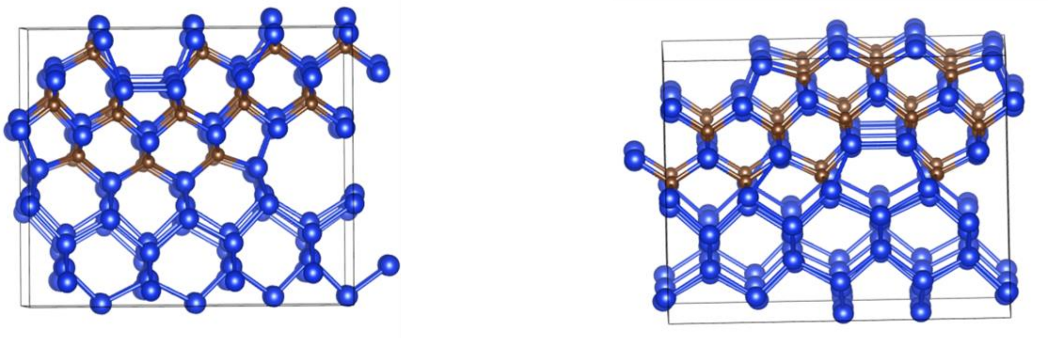

Figure 2.4. The configuration for SiC/Si interface along <110> direction (left), and SiC/Si interface along <1-10> direction (right) obtained by using VASP based on the method of Ref. [44].

To obtain the formation energy of C_nI_n, we use two different but complementary methods. One is from bottom to top, based on DFT calculation of small clusters (Figure 2.3), the other is from top to bottom, based on the calculated formation energy of bulk SiC and of SiC/Si interfaces (Figure 2.4).

Table 2.2. Formation energy for C/I clusters

Configurations	**System energy (eV),** $E_{C_nI_n}$	**Formation energy (eV),** $E^f_{C_nI_n}$
C_2I_2	-361.87	-2.671
C_3I_3	-370.44	-5.484
C_4I_4	-378.50	-7.784
Infinite Chain (8 CI in 64 atom cell)	-410.00	-16.252

Energies for C_2I_2, C_3I_3 and C_4I_4 were determined by DFT calculation directly. For the DFT calculation, we tried different configurations for each cluster. We find that for small clusters the most energetically favored structure is elongated along a chain. The DFT calculation results are listed in Table 2.2.

The formation energies in Table 2.2 use CI as the reference, and the expression is:

$$E^f_{C_nI_n} = E_{C_nI_n} + (n-1)*E_{Si_{64}} - n*E_{CI} \tag{2.23}$$

where E_{Si64} (-347.68eV) is the energy for a 64 atom Si supercell and E_{CI} (-353.44eV) is the energy of system with CI in a supercell with 64 Si and 1 C atom. However, to get the energy for C_5I_5, C_6I_6 and C_7I_7, larger supercells and more complex structures should be considered. For simplicity, we propose an empirical equation for the formation energy of small clusters by considering strain energy and surface energy, based on the calculation results for small clusters:

$$E^f_{C_nI_n} = n*E_\infty + 0.5*k*n*\left(\frac{1.85*n-2.7332}{n} - 1.93\right)^2 + E_{end},\ n \ge 3 \tag{2.24}$$

where the parameters we use are E_∞ = -2.03 eV, $k = 0.159\mathrm{eV}$ and E_{end} = 0.334 eV. The other approach for the energy of C_nI_n is by using the formation energy of SiC and its interface energy with silicon. The resulting expression is:

$$E^f_{C_nI_n} = n*E_{SiC\infty} + 4\pi*r^2*\sigma \tag{2.25}$$

$$E_{SiC\infty} = (E_{Si_{64}C_{64}} + 63 * Si_{64} - 64 * E_{CI}) / 64 \tag{2.26}$$

where the calculated value for $E_{\mathrm{SiC}\infty}$ is -3.92 eV, defining the formation energy for SiC from CI as an infinite carbon precipitate. All the energy values are based on DFT calculations. In a simple analysis, assuming the precipitate has a spherical shape. σ (1.55-1.58 J/m^2) represents the associated interface energy per unit area [44]. Combining the two approaches, we choose the lower energy value at each size in our simulations. We use the energies in Table 2.2 for size from 2 to 4 by directly calculation, and the energy for size 5 and 6 are from the Eq. 2.24. The energies for larger clusters (n≥7) are obtained using Eq. 2.25, and only the moments for the larger sizes are considered in the reduced model as described in Section 2.1.

2.2.2 *Energetics of Metal Binding to Carbon Clusters*

Using the most stable structures we found for small clusters, we put a metal atom in different 1NN or 2NN tetrahedral sites to the carbon clusters as interstitial to find the strongest binding sites. The binding energy E_b is calculated based on the equation:

$$E_b = E_{metal/C_nI_n} + E_{Si_{64}} - E_{metal} - E_{C_nI_n} \tag{2.27}$$

where E_{metal} is the system energy for an interstitial metal atom in silicon supercell and E_{metal/C_nI_n} is the energy for system with a metal atom binding to C_nI_n in supercell. E_b is further modified by considering the Fermi level difference between the metal in supercell and C_nI_n in supercell. Since the structures for C_5I_5 and C_6I_6 in our model are quite similar to C_4I_4, we use the binding energy to C_4I_4 for C_5I_5 and C_6I_6.

Larger precipitates are considered as SiC in our model. To find out the metal binding energy to SiC, the first step is to generate the SiC/Si interface. Since the ratio between the lattice constant for SiC (0.4375 nm) and Si (0.5457 nm) is about 4:5 based on our DFT calculation. We generate slab structure for SiC with 5 atoms × 5 atoms in *xy* plane, and for Si with 4 atoms × 4 atoms in *xy* plane. After taking out 3 rows of carbon atom as suggested in Ref. [44] and allowing full relaxation, we successfully built the most stable SiC/Si interface as illustrated in Figure 2.4. The interface we obtain in our DFT calculation has a surface energy 1.6 J/m^2 which is close to the 1.55-1.58 J/m^2 value calculated in Ref. 44. Then we tried different sites to place a metal atom to find the strongest binding sites. The final results are shown in Table 2.3. We can see that there is moderate binding of most metals to small C/I clusters and strong binding to SiC precipitates.

Table 2.3. Binding energy for metal to different carbon complexes

Metal	**Binding to C_2I_2 (eV)**	**Binding to C_3I_3 (eV)**	**Binding to C_4I_4 (eV)**	**Binding to SiC (eV)**
Cu	-0.32	-0.67	-0.66	-2.32
Fe	-0.23	-0.78	-0.60	-3.16
W	-0.27	-0.58	-0.64	-3.36
Ni	-0.63	-1.1	-0.74	-1.16
Ti	-0.34	-0.73	-1.21	-2.58
Cr	-0.60	-1.25	-1.53	-1.14
Mo	-0.18	-0.16	-0.40	-3.22

2.3 COMPARISON OF MODEL TO EXPERIMENT

The model for carbon precipitation is implemented into Sentaurus process module to simulate the experiments. The first experiment we compared to is carbon implantation at energy of 1.2MeV with a dose of 5×10^{15} cm^{-2} followed by 1200 ^{o}C annealing for 3 hours [45]. The initial implantation profile in our model is generated by Monte Carlo method with "+1" model. A 311 model for point defects is also included [46]. As can be seen from Fig. 2.5(a), there is an immobile peak of precipitated carbon, combined with an increase for the background carbon concentration, which is due to the diffusion of unprecipitated carbon.

We also use our model to simulate the boron and carbon co-implantation, for which 5 streams model for boron diffusion is also used. In the experiments of Uematsu we compared to, carbon is implanted at energy of 25 keV with a dose of 10^{15} cm^{-2}, followed by boron implantation with a dose of 2×10^{14} cm^{-2} at energy of 20 keV. The sample is annealed in a furnace at 800 ^{o}C for 30min and by rapid thermal annealing (RTA) at 1000 ^{o}C for 5s or 30s. As illustrated in Fig. 2.1(b), there is an obvious diffusion tail for 30s RTA beyond the implantation region above $10^{17}cm^{-3}$. While for 5 s annealing, there is no such diffusion tail.

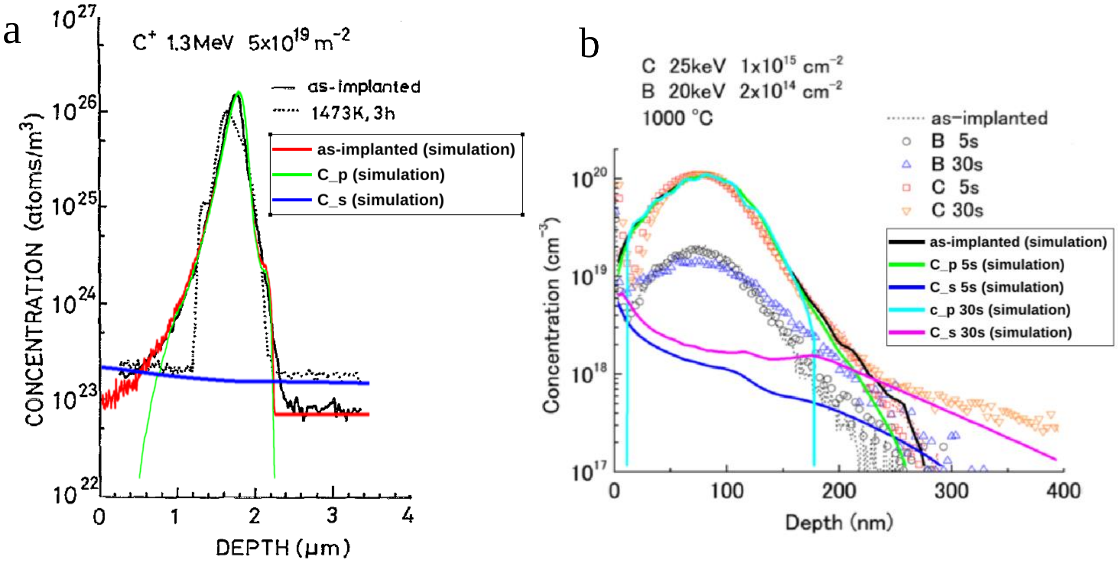

Figure 2.5. Comparison between simulation and experiment. Here we use C_s to represent substitutional Carbon, and C_p for carbon precipitates. The background figures for experimental data are taken from (a) Isomae et al. [45] and (b) Uematsu [30].

2.4 INTEGRATED WITH DEVICE SIMULATION

From the Shockley-Read-Hall theory, the recombination rate of electron-hole pairs is given by Equation (1.28). Under reverse-bias conditions for a photodiode, where the mobile carrier concentration in the depleted space-charge region can be neglected, the SRH recombination equation becomes:

$$U = \frac{-n_i^2}{\tau_p\left(n + n_i \exp\left(\frac{E_t - E_i}{k_B T}\right)\right) + \tau_n\left(p + n_i \exp\left(\frac{E_i - E_t}{k_B T}\right)\right)} = \frac{-n_i}{\tau_g} \tag{2.28}$$

where τ_g is the carrier generation lifetime which can be largely reduced when introducing recombination/generation centers, such as metal impurities. If the dark current is dominated by thermal generation, which is often the case in metal contamination, the expression for dark current is [47]:

$$I_r = qn_i WA / \tau_g \tag{2.29}$$

where W is the width of deletion region, and A is the cross-section area. As a result, by reducing metal concentration we can increase the generation life time. Therefore, the dark current can be reduced.

One of the important techniques to remove unwanted impurities, such as metal contamination in depletion region, is gettering. Gettering is a process by which harmful impurities are removed by providing an alternative location (a “getter”) where they prefer to reside with lower energy and have minima harm. Different gettering methods have been used previously [48]. As can be seen from the above experiments and simulation, carbon implantation can result in a sharp immobile peak due to carbon precipitation. Based on our DFT calculation, there is very strong binding between carbon precipitates and metal species, as listed is Table III. This indicates that carbon implantation can be a very effective method for metal gettering, which has been verified by a range of previous gettering experiments via carbon implantation [31-33].

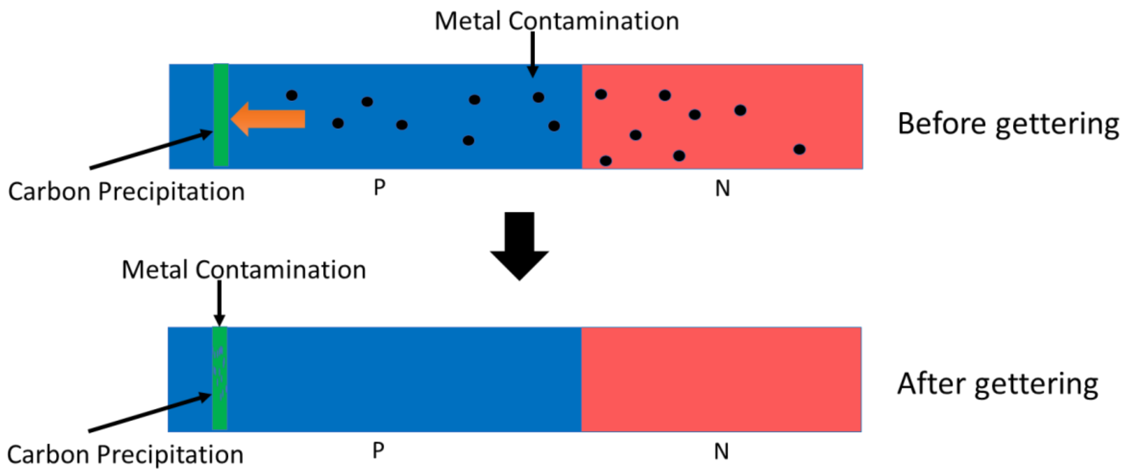

Figure 2.6. Schematic for gettering of metal contamination by carbon precipitation.

Table 2.4. Parameters of Iron for Sentaurus Device simulation

Properties	**Value**	**Ref.**
Diffusivity	$0.0013\exp(-0.68/k_BT)$	[137]
Defect Type	Donor	[138]
Location (eV)	$E_V + 0.39$	
Electron Capture Cross section (cm^{-2})	5×10^{-14}	
Hole Capture Cross section (cm^{-2})	7×10^{-17}	

Initial dark current simulation is conducted in Sentaurus Device using the gettering simulation results from Sentaurus Process with the parameters in Table 2.4. The initial iron concentration is set to be 10^{13} cm^{-3}. After 10 min 1000 ^{o}C furnace annealing, most of iron atoms are gettered by carbon precipitation. The dark current of the photodiode after gettering is only about 7% of initial value. The reduction of dark current can be quite beneficial for larger dynamic range and less noise for advanced silicon CMOS image sensor.

Chapter 3. MOMENT-BASED MODELING OF OXYGEN PRECIPITATION

Oxygen precipitates can serve as gettering sites to remove unintentional impurities, while they can also result in the generation of extended defects that may be harmful to the yield and device performance [11, 49-53]. Thus, it would be desirable to have a computational model which can guide the development of processes to generate oxygen precipitate in a more controlled manner.

Oxygen precipitation has been studied for a long time under different processing conditions [54-58] and different models has been proposed to understand the precipitation behavior. Oxygen precipitation was first modeled using nucleation theory [59-61] and growth law [62-63]. Then, the impact of point defects and strain energy were included in some models [64-68]. Later, models based on kinetic rate equations (KREs) and Fokker-Planck equation (FPE) were adopted to model oxygen precipitation more accurately. However, models based on only KRE [69] are often computationally expensive since hundreds of coupled differential equations needed to be solved, which may not be feasible in large scale 2D or 3D process simulation; Models based on FPE often requires the use of custom solvers [70-72] and introduction of empirical fitting parameters [73].

In our previous work, a moment based model for oxygen precipitation was proposed [37], which can efficiently describe the precipitation process and maintain good computation efficiency. However, precipitates are presumed to incorporate the optimal (energy-minimizing) number of vacancies at all times. This assumption is not valid for fast ramping and lower temperature processes, where the number of vacancies in precipitate doesn’t reach equilibrium in real time. In addition, only spherical precipitates are considered in the model, but morphology evolution of oxygen precipitate has been observed [65, 66, 73, 74] which has great influence in the precipitation kinetics as well as the gettering efficiency [75].

In this chapter, the reduced kinetic precipitation model (RKPM) is further developed building on the approach of Ref [37], with the consideration of morphology evolution, and dynamic incorporation of point defects. In addition, by including Fermi level effects and a boron/interstitial clustering model [76], the impact of boron doping is also considered in modeling oxygen precipitation.

3.1 MODEL DESCRIPTION

In Chapter 2, we discuss a moment based model for carbon precipitation in detail. To model oxygen precipitation we need to rethink some of the assumption we have made for carbon precipitation. For oxygen precipitation, we need to consider the strain energy, the interaction between precipitates and point defects, and the shape evolution. Instead of considering the spherical shape precipitate as C_nI_n, we model the oxygen precipitate with oblate spheroidal shape as O_nV_m.

To describe the oxygen precipitate, we introduce a set of parameters as follows:

n: Precipitate size (the number of oxygen atoms in precipitate);

m: Net vacancy incorporation (the number of vacancies – the number of interstitials incorporated in a precipitate);

f_n: Concentration of oxygen precipitates with size n;

$f_{n,m}$: Concentration of oxygen precipitate with size n and net vacancy incorporation m;

h_n: The total concentration of net vacancies incorporated in all size n precipitate;

m_n: The average net vacancy incorporation in a size n precipitate, with $m_n = h_n/ f_n$.

β: Aspect ratio of oblate spheroidal precipitate.

C_X: The concentration of X;

C_X^*: The equilibrium concentration of X;

NetC_I: Net interstitial concentration in silicon matrix, with NetC_I= C_I - C_V and $C_\mathrm{I} C_\mathrm{V} \approx C_\mathrm{I}^* C_\mathrm{V}^*$.

The schematic of proposed oxygen precipitation model is illustrated in Figure 3.1. In this model, the rapid recombination for interstitials and vacancies is assumed, so only one point defect species needs to be considered in excess energy and reaction rates. Here net vacancy incorporation is used in oxygen precipitate and net excess interstitial concentration is used in silicon matrix. By consuming interstitial oxygen, the size of oxygen precipitate, n, will increase. The oxygen precipitate is assumed to have a phase of SiO_2 in our study, as in many previous report. Since the atomic volume per silicon of SiO_2 is about 2.2 times larger than that of crystalline Si, the growth of the oxygen precipitate is accompanied with large compressive strain from the surrounding Si matrix. The compressive strain can be relieved by consuming vacancies or ejecting interstitials. As a result, the net vacancy incorporation, m, in the precipitate will also increase. However, we cannot completely describe the two-dimensional system by having $\mathrm{m} \times n$ equations, as that is not feasible for computation. Thus, we simplify the system by only considering the average net incorporation of vacancies at a certain size, i.e. m_n in Figure 3.1. In addition, to consider the shape evolution of the precipitate, we model the precipitate as an oblate spheroid with aspect ratio, β. Spherical precipitates modeled in previous publications are equivalent to fixing $\beta = 1$ in the present model.

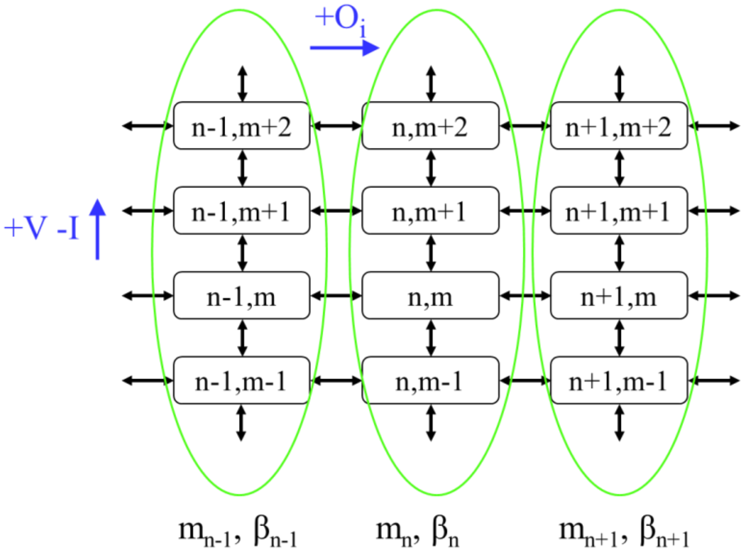

Figure 3.1. Schematic of oxygen precipitation model. Precipitates grow by incorporating O interstitials (to the right in figure) and relieve strain by incorporating vacancies (up in figure). At any given size n, we define an average number of V incorporated (m_n) and aspect ratio (β_n).

.

3.2 ENERGY OF OXYGEN PRECIPITATE

The total free energy change, $\Delta G_{n,m,\beta}$, upon precipitate formation can be written [37]:

$$\Delta G_{n,m,\beta} = -nk_BT\ln\left(\frac{C_O}{C_{ss}}\right) - mk_BT\ln\left(\frac{C_V}{C_V^*}\right) + \Delta G^{surface}_{n,m,\beta} + \Delta G^{strain}_{n,m,\beta} \tag{3.1}$$

where surface energy $\Delta G^{surface}_{n,m,\beta}$ is expressed by:

$$\Delta G^{surface}_{n,m,\beta} = \frac{\alpha}{\beta} * \left(\frac{3*\sqrt{\pi}V_n}{4}\right)^{2/3} * \left(2+\frac{\beta^2}{(1-\beta^2)}*\ln\left(\frac{2-\beta^2}{\beta^2}\right)\right) \tag{3.2}$$

$$V_n = \frac{n}{2}*\Omega_{SiO_2} \tag{3.3}$$

Here, Ω_{SiO_2} is the molecular volume of SiO_2, V_n is the volume of precipitate with size n, and α is the surface energy coefficient. Strain energy $\Delta G^{strain}_{n,m,\beta}$ is calculated by considering an incoherent oblate spheroid inclusion of SiO_2 in silicon matrix based on Eshelby's inclusion theory [77-79]:

$$\Delta G_{n,m,\beta}^{strain} = 6V_n \mu_{Si} \frac{e_T^{\,2}(n,m)}{1+4\mu_{Si}/(3K_{SiO_2})} f(\beta) \tag{3.4}$$

$$e_T(n,m) = \left(\frac{\Omega_{SiO_2} * n/2}{\Omega_{Si} * (n/2+m)} \right)^{1/3} - 1 \tag{3.5}$$

where $f(\beta)$ is a function of β based on the inclusion theory, Ω_{Si} is the atomic volume of silicon, μ_{Si} is the shear modulus of silicon and K_{SiO_2} is the bulk modulus of SiO_2. e_T is the transformation strain (or linear misfit strain) indicating the mismatch between perfect silicon matrix and precipitate with size (n, m). If we use the parameters in Table 3.1, $f(\beta)$ can be calculated numerically as shown in Figure 3.2 and is fitted by an exponential function. The method to calculate strain energy can be found in Appendix B.

The surface energy is minimized when $\beta=1$ (Equation (3.2)) while the strain energy is minimized at $\beta=0$. The sum of the strain energy and surface energy is defined as excess energy. In our model, oxygen precipitates always tend to stay with optimal aspect ratio, β, to minimize the excess energy.

Since we only consider the average net vacancy incorporation at a given size, m_n, we can modify the expression as:

$$\Delta G_{n,\beta} = -nk_B T \ln\left(\frac{C_O}{C_{ss}} \right) - m_n k_B T \ln\left(\frac{C_V}{C_V^{\,*}} \right) + \Delta G_{n,m_n,\beta}^{surface} + \Delta G_{n,m_n,\beta}^{strain} \tag{3.6}$$

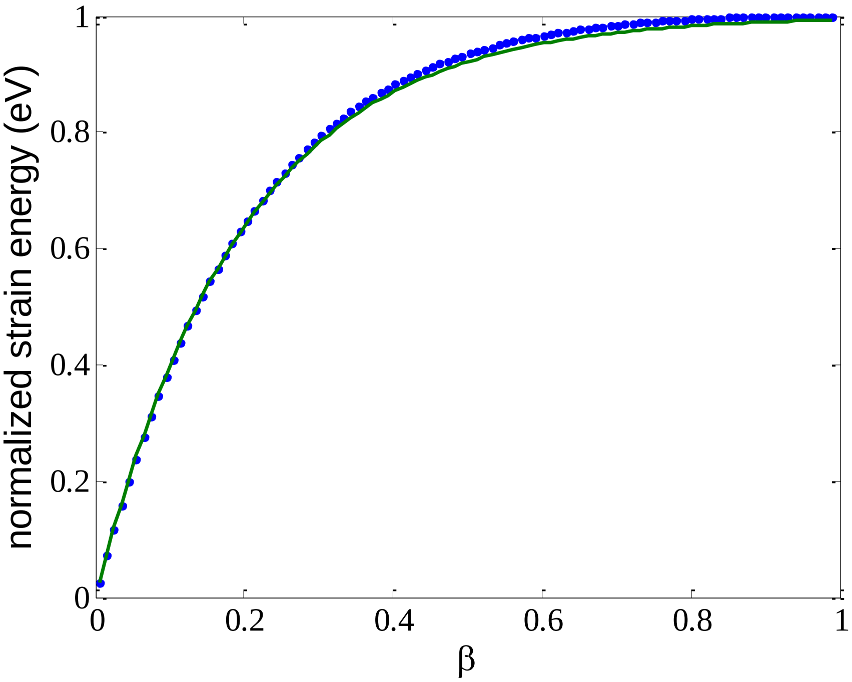

Figure 3.2. Normalized strain energy vs aspect ratio. Dots are results for numerical calculation and solid line is fitted exponential function, *f(β)=(1-exp(-5.078 β))*.

3.3 KINETIC RATE EQUATIONS:

We use kinetic rate equations to describe the dynamic behavior for small oxygen clusters with $n<72$. The equations we formulate to solve f_n are:

$$\frac{\partial f_n}{\partial t} = R_n - R_{n+1} \qquad n = 2,\ 3\ldots\ \ldots \tag{3.7}$$

$$R_n = g_{n-1} f_{n-1} - d_n f_n \tag{3.8}$$

where g_n is the growth rate from size n to n+1 and d_n is the dissolution rate from size n to n - 1.

The expressions for diffusion limited growth and dissolution rate are similar to that in Chapter 2:

$$g_n = \lambda_n D_O C_O \tag{3.9}$$

$$d_n = g_{n-1} \exp\left(\frac{\Delta G_{n,\beta} - \Delta G_{n-1,\beta}}{k_B T}\right) \tag{3.10}$$

Here C_O is the concentration of oxygen interstitial, D_O is the diffusivity of oxygen interstitial, k_B is the Boltzmann's constant, and λ_n is a kinetic factor that depends on the geometry and interface reaction distance, which can be expressed as [73]:

$$\lambda_n = \frac{4\pi r_n^2}{a + r_n} \frac{\sqrt{1-\beta^2}}{\arccos(\beta)} \beta^{-\frac{1}{3}} \tag{3.11}$$

where r_n is the radius of size n precipitate and a is on the order of the silicon lattice constant.

We use $h_n = f_n m_n$ to track the evolution of point defect incorporation. The related equations are:

$$\frac{\partial h_n}{\partial t} = R_n{}^h - R_{n+1}{}^h + f_n \frac{\partial m_n}{\partial t} \qquad n = 2,\ 3\dots\dots \tag{3.12}$$

$$R_n{}^h = g_{n-1} h_{n-1} - d_n h_n \tag{3.13}$$

$$\frac{\partial m_n}{\partial t} = \lambda_n D_V (C_V - C_V^E) - \lambda_n D_I (C_I - C_I^E) \tag{3.14}$$

Here C_V^E and C_I^E are the concentrations of intrinsic point defects in local equilibrium with the precipitate, defined as:

$$C_V^E = C_V \Big|_{\frac{\partial \Delta G_{n,m,\beta}}{\partial m} = 0} \tag{3.15}$$

$$C_V^E * C_I^E = C_V^* * C_I^* \tag{3.16}$$

As can be interpreted from the above equations, interstitial and vacancy tend to approach their local equilibrium concentration, which would make m_n approach the optimal value to minimize energy. In the previous model [37], a first order approximation is used to estimate the optimal value for m_n, which simplifies the model and works reasonably well. However, when point defects are far away from equilibrium, the first order approximation would result in substantial error in predicting the optimal m_n. Moreover, in fast ramp and low temperature processes, m_n may not always have the chance to reach the optimal value. Thus, considering the dynamic evolution of point defect incorporation is expected to be helpful in predicting the precipitation behavior during fast ramp and low temperature processes.

3.4 MOMENT-BASED MODEL

We use a reduced kinetic precipitation model to describe oxygen precipitation, where only the moments of large precipitates are considered [36, 37]. The delta function approximation is used in the model where the behavior of precipitates is assumed to be given that for the average size (n_{avg}). We consider clusters up to size *k-1* with discrete rate equations, while we use the moments to capture the distribution for clusters with *k* or more oxygen atoms. *k*=72 is used for simulation on the basis of Ref. [37]. The *i*th moment is defined as:

$$m_i = \sum_{n=k}^{\infty} n^i f_n \tag{3.17}$$

The method to get m_0 and m_1 have been previously described in Chapter 2 for carbon precipitation and Ref. [37] for oxygen precipitation. In addition, we also need to consider the 0th moment of h_{n} which is

$$m_0^h = \sum_{n=k}^{\infty} h_n \tag{3.18}$$

$$\frac{\partial m_0^h}{\partial t} = R_k{}^h + m_0 \frac{\partial m_{n_{avg}}}{\partial t} \tag{3.19}$$

$$n_{avg} = m_1 / m_0, \quad m_{n_{avg}} = m_0^h / m_0 \tag{3.20}$$

with $m_0{}^h$ represent the total net vacancy amount in all the larger oxygen clusters. The rate of change of total vacancy incorporation $m_0{}^h$ contains the formation of minimum size clusters considered in the moments and point defect exchange with the matrix to minimize energy.

As can be interpreted from Equations (3.4) and (3.5), n_{avg} and m_{navg} determine the magnitude of the transformation strain (e_{T}) of large oxygen clusters. In oxygen precipitation process at relatively lower temperature ($700 \leq \mathrm{T} \leq 900$ °C), $D_{\mathrm{O}}C_{\mathrm{O}}^{*} > D_{\mathrm{I}}C_{\mathrm{I}}^{*}$, so the background silicon matrix commonly has a substantial interstitial supersaturation, which would make the ratio between m_{navg} and n_{avg} smaller than the equilibrium value (~0.56). With a fixed n_{avg}, the smaller the ratio, the larger the transformation strain and thus the strain energy. When the strain is a large enough portion of the total excess energy, the precipitate shape would change from sphere toward platelet to reduce strain energy. At high temperature (T>1000 °C) $D_{\mathrm{O}}C_{\mathrm{O}}^{*} < D_{\mathrm{I}}C_{\mathrm{I}}^{*}$, the interstitial concentration would remain close to equilibrium. So $m_{\mathrm{navg}} / n_{\mathrm{avg}}$ ratio is close to equilibrium and the strain will be largely relaxed. Thus, platelet shaped precipitates are generally observed at lower temperatures.

The overall picture for oxygen precipitation is illustrated in Figure 3.3. Oxygen supersaturation ($C_O/C_{SS} > 1$) in silicon leads to the formation and growth of oxygen precipitates. As they grow, these precipitates will accumulate compressive strain, which is relieved by interstitial ejection (or vacancy absorption) and results in the supersaturation of interstitials ($C_I/C_I^* > 1$). The increase of interstitial supersaturation reduces the net vacancy to oxygen ratio (m/n) which in turn will increase the strain energy. If the strain energy becomes more dominant than surface energy in the total excess energy, the aspect ratio (β) of oblate spheroid precipitate will reduce. The reduction of the aspect ratio may reduce the total free energy required (ΔG) to form precipitate and thus promote the further growth of the precipitate. In addition, the supersaturated interstitials will also tend to aggregate to form dislocation loops, facilitated by the local tensile strain in silicon lattice surrounding compressively-strained oxide precipitate. The dislocation loops serve as a sink for interstitials, thereby cultivating precipitate growth.

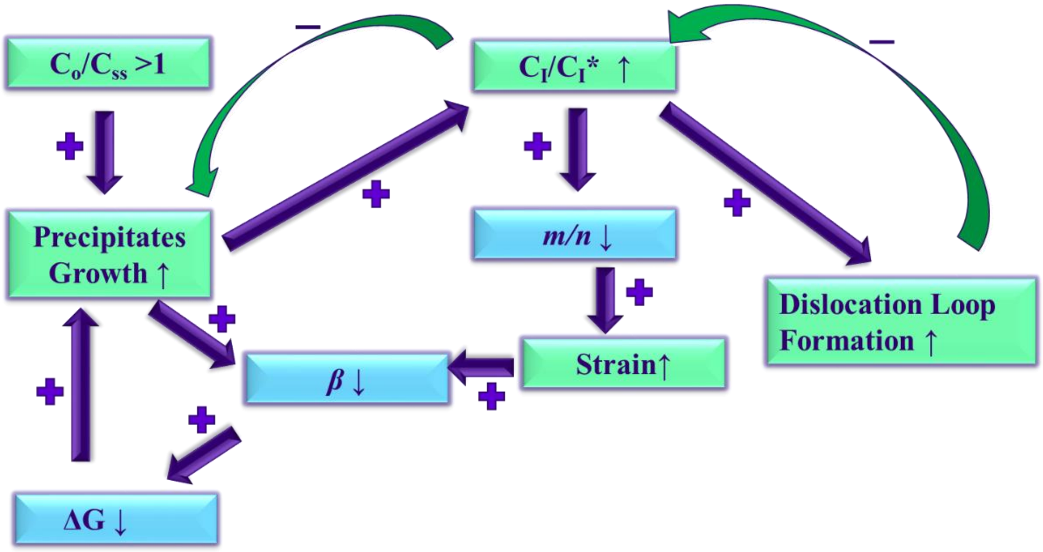

Figure 3.3. Schematic for the process of oxygen precipitation. "+" indicates effect for promoting and "-" indicates effect for retarding.

3.5 THE IMPACT OF BORON DOPING.

Boron is generally believed to enhance the oxygen precipitation process and some models have been proposed to describe the process [80-83]. Here we adopt previously reported boron/interstitial cluster model and integrate it with our moment based oxygen precipitation model. In our model, boron doping impacts the oxygen precipitation process in two ways: a) change the equilibrium point defect concentrations (and thus their transport capacity (e.g., $D_I C_I^*$)) by affecting the Fermi level; and b) form boron interstitial clusters to consume excess interstitials and thus promote O precipitation.

There are multiple charge states for intrinsic point defects. The equilibrium concentration of neutral point defect is independent of Fermi level, while the charged point defects have Fermi level-dependent equilibrium concentrations. Thus, the total equilibrium concentration of point defects should be changed at different doping level as:

$$C_X = \left(C^*_{X^0}\right) + \left(C^*_{X^-}\right)_i \left(\frac{n}{n_i}\right) + \left(C^*_{X^{--}}\right)_i \left(\frac{n}{n_i}\right)^2 + \left(C^*_{X^+}\right)_i \left(\frac{p}{n_i}\right) + \left(C^*_{X^{++}}\right)_i \left(\frac{p}{n_i}\right)^2 \tag{3.21}$$

Here X stands for vacancy or interstitial, C^* is the intrinsic equilibrium concentration for that species, n_i is the intrinsic carrier concentration in silicon and n (p) indicates electron (hole) concentration.

As reported in previous research [76, 84], there is significant bonding between boron and interstitials. When boron concentration is high enough, boron-interstitial clusters form. The formation of B/I clusters reduces the interstitial supersaturation caused by oxygen precipitation, which will in turn promote the oxygen precipitation process.

For a simplified model, we can assume that the concentration of all the small B/I clusters (e.g., BI, B_2I) rapidly equilibrate with the free boron and interstitial concentrations [76]. B_3I is the dominant cluster and is the only species that needs to be solved numerically since it is present in non-equilibrium quantities. The corresponding reaction and rate are:

$$B_2I + BI \leftrightarrow B_3I + I \tag{3.22}$$

$$R_{B_2I/BI} = 4\pi a D_{BI} \left(C_{B_2I} C_{BI} - \frac{C_{B_3I} C_I}{K_{B_2I/BI}} \right) \tag{3.23}$$

In the expression, $K_{A/B}$ is the equilibrium constant for the clustering reaction between A and B, and $R_{A/B}$ represents the clustering rate. Here we use the equilibrium concentration of C_{B_2I} and C_{BI} in the above equation, which are obtained by:

$$C_{BI} = K_{B/I} C_B C_I \tag{3.24}$$

$$C_{B_2I} = K_{B/BI} C_B C_{BI} \tag{3.25}$$

All the equilibrium constants we use are listed in Table 3.1. We also need equations for the evolution of interstitial oxygen C_{O} and NetC_{I} to solve the entire set of equations. These are expressed as follows:

$$\frac{\partial C_O}{\partial t} = D_O \nabla^2 C_O - \frac{\partial m_1}{\partial t} - \sum_2^k n \frac{\partial f_n}{\partial t} \tag{3.26}$$

$$\frac{\partial [NetC_I]}{\partial t} = D_{CI} \nabla^2 C_I - D_{CV} \nabla^2 C_V + \frac{\partial m_0^h}{\partial t} + \sum_2^k \frac{\partial h_n}{\partial t} - \frac{\partial C_{B_3I}}{\partial t} \tag{3.27}$$

The boundary conditions and model for dislocation loops and small oxygen clusters are the same as in Ref. [37].

Table 3.1. Model parameters

Parameter	**Value**	**Reference**
D_O	0.13 exp(-2.53 eV/k_BT) cm^2/sec, T>750 ^{o}C	[88]
	2.16×10^{-6} exp(-1.55 eV/k_BT) cm^2/sec, T<750^{o}C	[89]
a	5.0 Å	
C_{SS}	3.04×10^{22} exp(-1.317 eV/k_BT) cm^{-3}	
D_I	51.4 exp(-1.77 eV/k_BT) cm^2/sec	[90] [91]
C_I^*	2.9×10^{24} exp(-3.18 eV/k_BT) cm^{-3}	
D_V	3.07 exp(-2.12 eV/k_BT) cm^2/sec	
C_V^*	1.4×10^{24} exp(-2.44 eV/k_BT) cm^{-3}	
C_{Si}	5.0×10^{22} cm^{-3}	
a_{Si}	5.431 Å	
V_{Si}	2.0×10^{-23} cm^3	
μ_{Si}	64.9 GPa	[92]
V_{SiO2}	4.35×10^{-23} cm^3	
K_{SiO2}	36.9 GPa	[93]
α	0.1735 J/m^2, T<800 ^{o}C	

	0.2400 J/m^2, T>900 ^{o}C	
$K_{B/I}$	exp(0.7 eV/k_BT)/ C_{Si}	[76]
$K_{B/Bi}$	exp(1.3 eV/k_BT)/ C_{Si}	
$K_{B2I/Bi}$	exp(1.2 eV/k_BT)	
D_{Bi}	0.036 exp(-1.09 eV/k_BT) cm^2/sec	
K_I^+	11.91 exp(-0.456 eV/k_BT)	
K_I^{++}	122.6 exp(-0.687 eV/k_BT)	
K_I^-	2×10^{-3}	
$K_I^=$	4×10^{-3}	
K_V^+	11.84 exp(-0.505 eV/k_BT)	
K_V^{++}	4×10^{-3}	
K_V^-	0.0926 exp(-0.146 eV/k_BT)	
$K_V^=$	0.0071 exp(-0.252 eV/k_BT)	

Table 3.2. Fitted initial conditions used to replicate experimental data.

Source	**Initial m_0** (cm^{-3})	**Initial n_{avg}**	**Initial N_I (cm^{-3})**
Schrems, et al [86]	1.0×10^6	1×10^3	-1×10^{11}
Chiou and Shive [54]	9.7×10^8	7.8×10^3	-7.36×10^{12}
Sueoka, et al. [74]	1.0×10^8	1×10^4	-4×10^{12}
Ono, et al. [87]	1.0×10^8	1×10^4	-4×10^{12}

3.6 SIMULATION RESULTS

The oxygen precipitation simulation is conducted in Matlab using the PDE solver. The parameters used in the simulation are summarized in Table 3.1 and Table 3.2. There are several different calibration factors for FTIR measurement for interstitial oxygen. We use the latest ISO-88 standard in our simulation [85]. All the measured interstitial oxygen concentrations across different experiments are normalized to this standard for consistency.

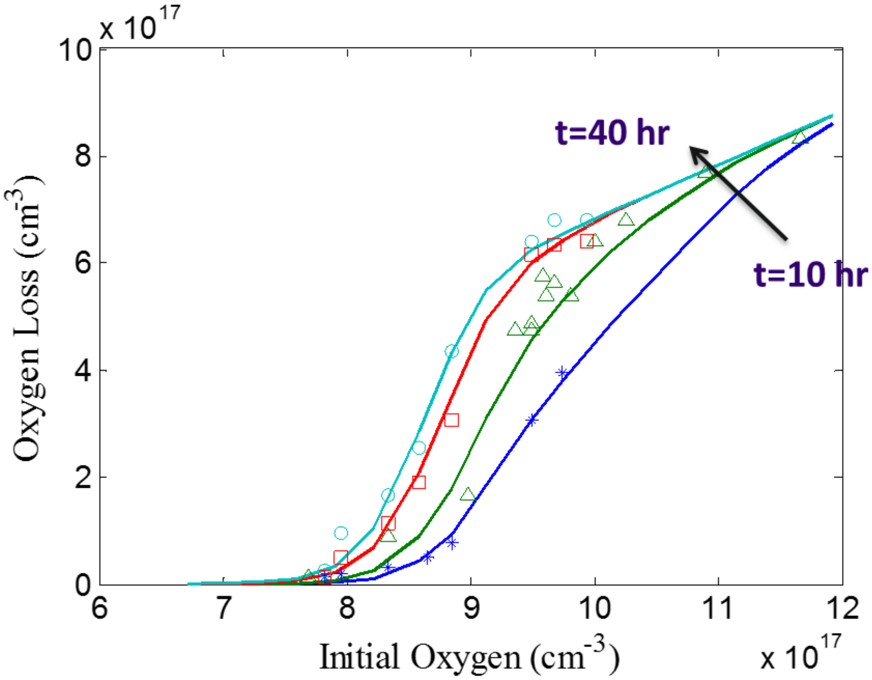

Figure 3.4. Comparison of the model to experimental observation of O precipitation due to two-step anneals by Schrems, et al [86]

The data in Figure 3.4 is extracted from Ref [86], where two-step annealing was conducted, first 750C for 4 hours and then 1050C for 10-40 hours. With reasonable initial conditions, our model can match the experimental data very well. The transition slopes and the turning points to form observable amounts of precipitation for different high temperature annealing times are well predicted by the model. The data in Figure 3.5 extracted from Ref. [54]. The difference in precipitation behavior with different nucleation and growth duration is also well described in our model.

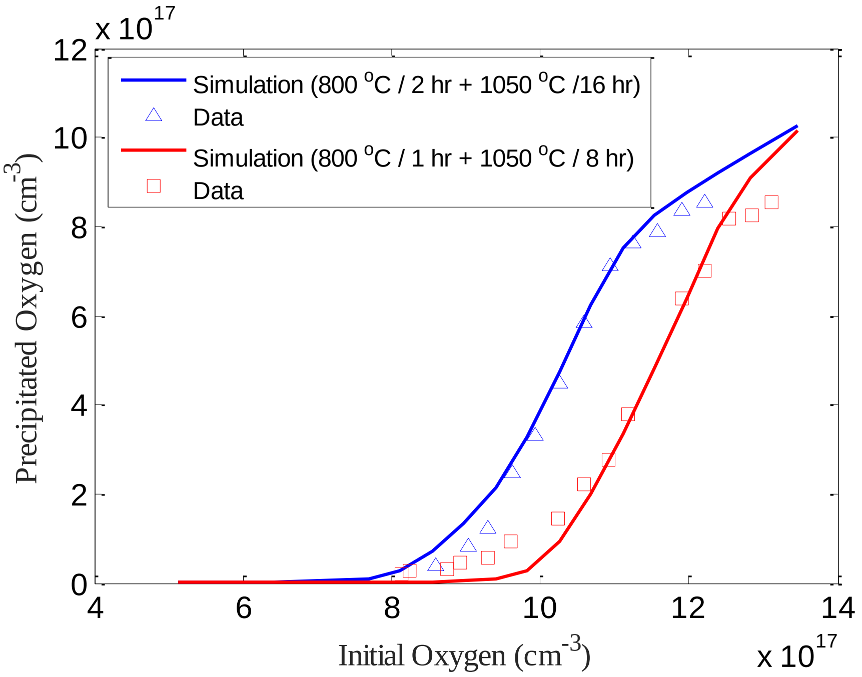

Figure 3.5. Comparison of the model to experimental observations of O precipitation due to two-step anneals by Chiou and Shive [54]

In addition, we use our model to predict the shape evolution as shown in Figure 3.6. Isothermal anneals at different temperatures were conducted in Ref [74] with same initial O concentration. The precipitate shape and interstitial oxygen concentration were recorded at 64, 200, 400 hours and 700 hours. At 700C, precipitates shape change from *sphere* to *oblate spheroid* at annealing time between 64 hours and 200 hours. While at 800C and 900C, the morphology becomes *oblate spheroid* well before the 64 hours' record time. Our model predicts the same phenomenon as seen in the experiment. The shape changes from 400 hours and 700 hours at 800C and 900C are attributed to the morphology instability, so we didn't include this in our model. It can be found that the predicted aspect ratio of the oblate spheroid is larger than the observed value. One possibility is that when the precipitates become plate shape, they tend to stay at <100> plane of silicon matrix [75] which may reduce the interface energy per area compare to the spherical precipitates. The reduction of interface energy per area would make the strain energy more dominant in excess energy. Thus, the reduction of aspect ratio to reduce strain energy can be expected. In addition, the model can also match the interstitial oxygen concentration at different annealing time, as shown in Figure 3.6(a).

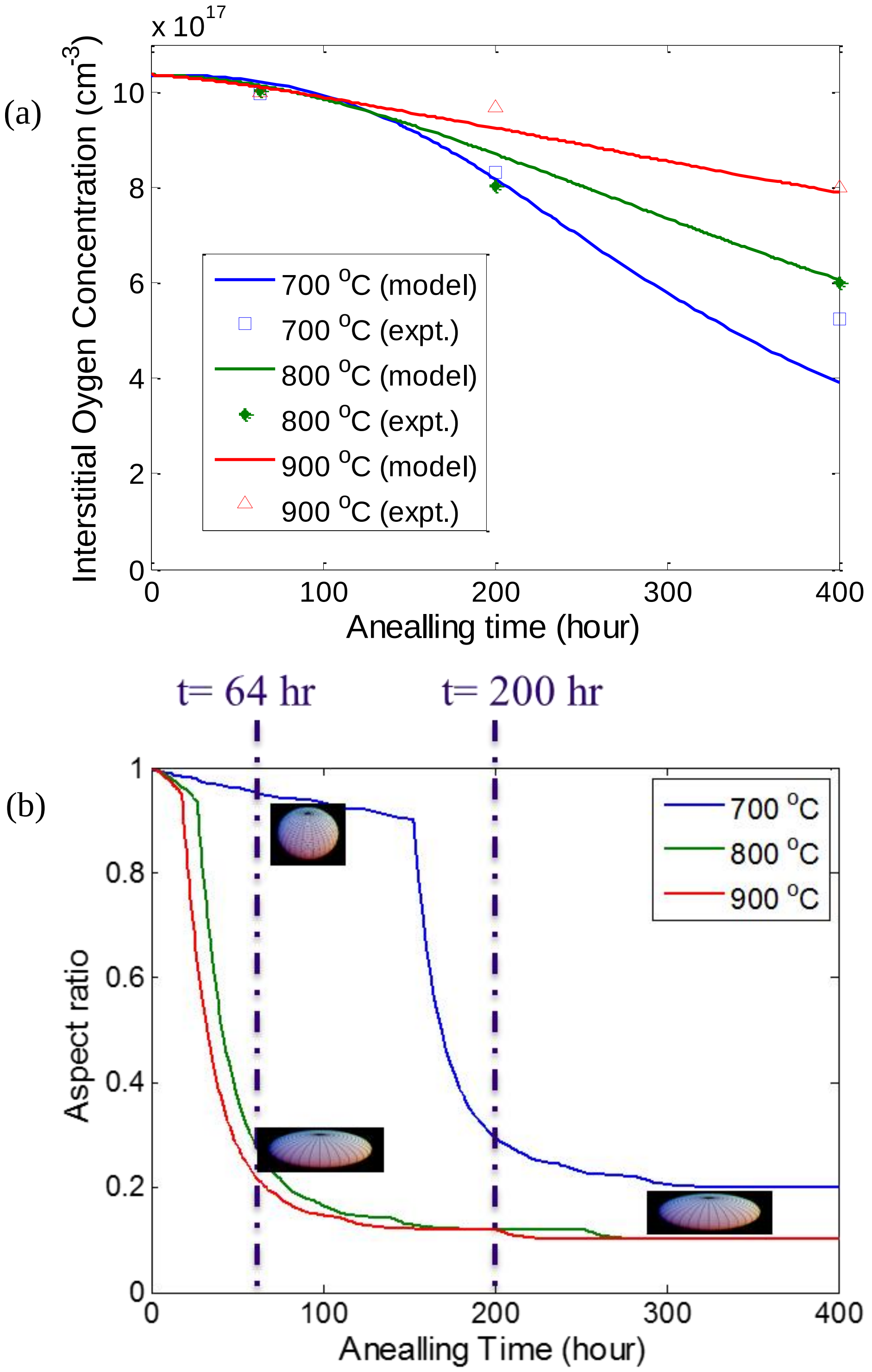

Figure 3.6. Comparison of the model to observations of O precipitation by Sueoka, et al. [74]. (a) shows drop in interstitial O over time, as O precipitates form, while (b) shows predicted aspect ratio versus time and comparison to observations at 64, 200, and 400 h.

The model predictions for the impact of Boron are shown in Figure 3.7. The experimental data is extracted from Ref [87]. Two step annealing, 900 C/4 h + 1000 C/16 h, was conducted with different boron doping. The general trend of enhancing oxygen precipitation is observed with boron doping up to 2.4×10^{19} cm^{-3}. Our model with boron/interstitial clustering well predicts the experimentally-observed behavior.

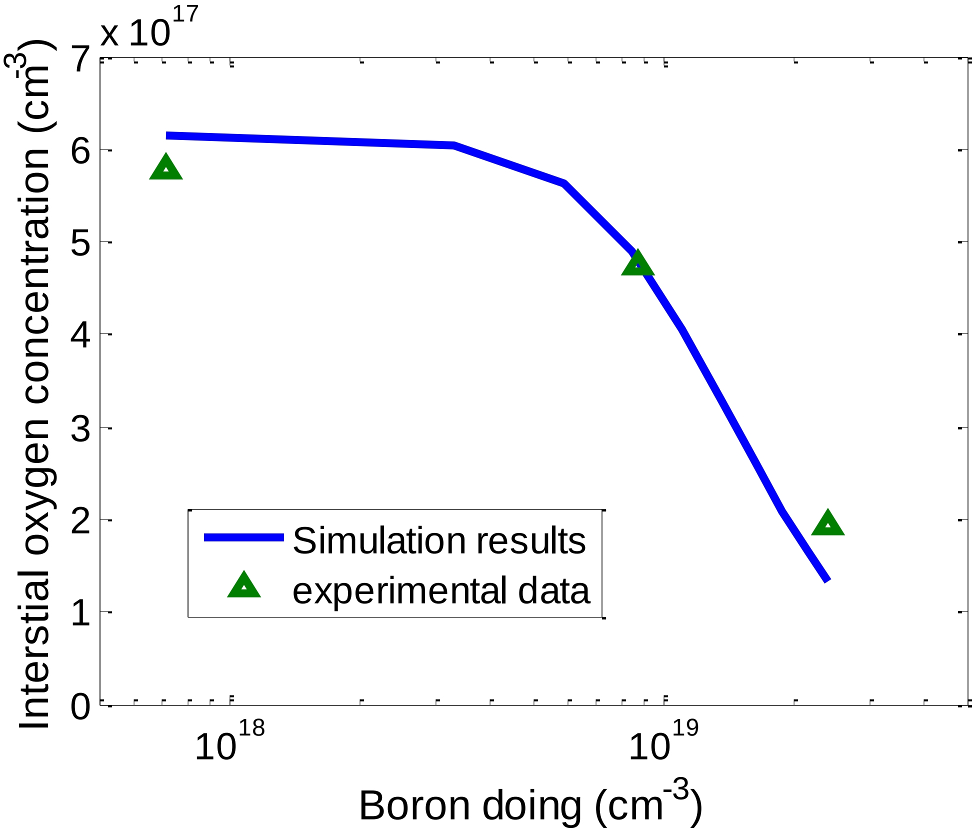

Figure 3.7. Comparison of the model to observed drop in interstitial O due to precipitation after two-step annealing for various B doping levels by Ono, et al. [87]

3.7 SUMMARY:

We develop a moment based oxygen precipitation model with the consideration of morphology evolution and dynamic incorporation of point defects. We also take into consideration the impact of B via a boron/interstitial clustering model as well as Fermi level effects, so that doping-dependent oxygen precipitation is also included in our model. The moment based precipitation model can replicate experimental data reasonably well and more computationally efficiently than models based on full set of KREs or FPE. Because of fewer required equations and the computational efficiency, our oxygen precipitation model has the potential to be integrated with other defect formation models and used in large scale TCAD simulations.

Chapter 4. IMPACT OF CHARGED GRAIN BOUNDARIES ON CDTE SOLAR CELL

CdTe solar cells offer a low-cost way to reach high conversion efficiency. $CdCl_2$ treatment is commonly used as grain boundary passivation process to enable CdTe cells to achieve high performance [94-96]. Experimental observations and theoretical calculations both suggest that CdTe grain boundaries (GBs) become positively charged after $CdCl_2$ treatment [97-101], becoming depleted or inverted for p-type material. Electron-beam induced current (EBIC) imaging [98] as well as other similar experimental techniques [99-101] suggest stronger carrier collection close to the grain boundary. Combining those facts, it has been suggested [98-101] that depleted grain boundaries are actually beneficial to CdTe solar cell performance because they can help to separate carriers, suppress recombination and improve carrier collection.

However, in this chapter we will show that while there is obvious enhancement of the EBIC signal near depleted grain boundaries, the solar cell response shows substantial reduction in the open circuit voltage and a small decrease or increase (depending on doping level) in short circuit current when grain boundaries are introduced. Counter-intuitively, larger band bending actually gives reduced short circuit current for typical CdTe cells due to the resulting enhancement of recombination near CdTe/CdS interface. While there is no obvious increase of EBIC signal near accumulation type grain boundaries (with negative charge for p-type bulk), such grain boundaries can modestly enhance the solar cell performance.

Our results indicate that EBIC signal enhancement or reduction near charged grain boundaries is not at all predictive of the impact of the grain boundaries on actual cell performance or even on short circuit current. The device simulation results suggest that a passivation process that leads to accumulation at grain boundaries is actually more desirable. This chapter is adapted from previous publications. [102, 103]

4.1 EBIC SIMULATION

EBIC imaging is a powerful technique which can resolve a material's electrical response at a scale much smaller than the grain size [104]. It can be used for the measurement of minority carrier diffusion length and surface recombination of a sample material. In the measurement, a focused electron beam impinges on the material and generates electron-hole pairs. Those carriers can travel to the contact and get collected or recombine before they reach the contact. The ratio, η, between the collected carriers to the generated carriers is the collection efficiency for the EBIC measurement.

Each electron can generate approximately $E_{beam}/(3E_g)$ electron-hole pairs, where E_{beam} is the energy of the electron beam and E_g is the material bandgap. The average experimental generation rate can thus be estimated as [105]:

$$G = (1-b)\frac{(I_{beam}/q)\times(E_{beam}/E_0)}{3\times(E_g/E_0)}\frac{1}{V} \tag{4.1}$$

Here, I_{beam} is the electron beam current, b is the backscattering coefficient, and V is the generation volume. For simplicity, we consider constant generation in a box with width w and depth d. Thus $V = dw^2$.

The generation rate in Equation (4.1) is defined in a three-dimension system, which is generally true for the experimental measurement. In our simulation, we use a two-dimensional system to model the EBIC signal response in three-dimensional structure. As discussed by Haney et al. [106], the ratio between critical generate rate to establish high ejection effect in 3D and 2D is $4L$, where L can be considered as the grain size in our simulation. Note that the unit of generation rate in reference [106] is $s^{-1}cm^{dim-3}$, while in present paper we use the units $s^{-1}cm^{-3}$. Thus we can use the following equation to estimate the equivalent generate rate in 2D, G^{2D}, to approximately model 3D EBIC signal response with generate rate G:

$$G^{2D} = G\frac{w}{4L} \tag{4.2}$$

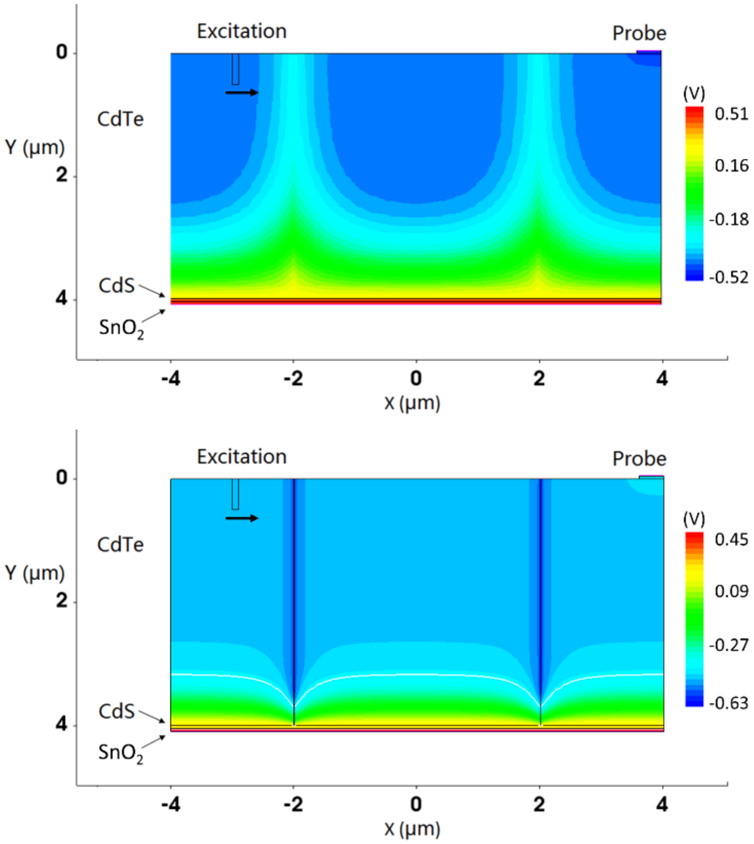

Figure 4.1. Electrostatic potential distribution in CdTe absorbers for EBIC simulation structure. (a) 0.25 V band bending near depleted grain boundary. (b) 0.11 V band bending near accumulated grain boundary.

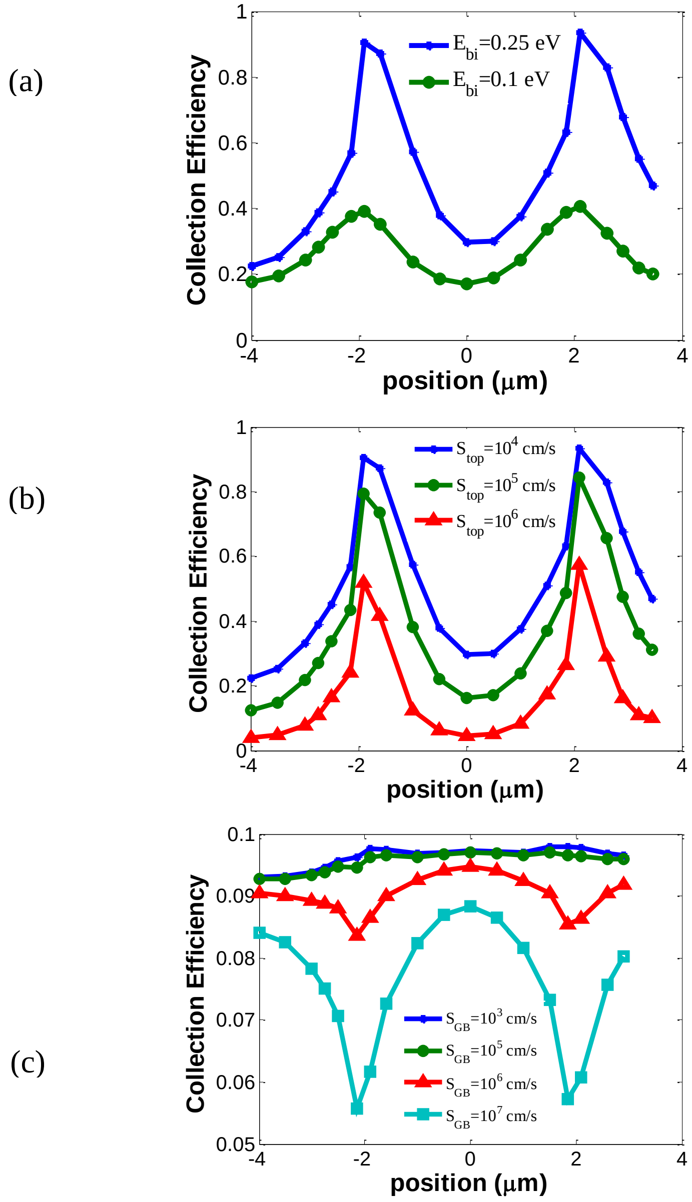

Figure 4.2. Simulated EBIC collection efficiency versus position with 2D generation rate $G^{2D}=1.8\times10^{24}cm^{-3}/s$ for CdTe with depleted grain boundaries (a-b) and accumulated grain boundaries (c). (a) Collection efficiency with different band bending (E_{bi}). Top surface recombination velocity, Stop=10^4 cm/s and grain boundary recombination velocity, $S_{GB}=10^3$ cm/s. (b) Collection efficiency with different top surface recombination velocities. E_{bi} =0.25 eV and $S_{GB}=10^3$ cm/s. (c) Collection efficiency with different grain boundary recombination velocities. E_{bi} =-0.11 eV and $S_{top}=10^4$ cm/s. Here we use positive value to represent depleted GB which is positive charged in p-type CdTe.

We constructed a thin film absorber structure for simulation as shown in Fig. 4.1 and simulated in Sentaurus Device. Constant carrier generation to an estimated penetration depth of $d = 0.2\mu m$ over width of $w = 0.1\mu m$ is defined to represent the electron beam excitation. The excitation point is scanned from x=-4 μm to x = 3.5 μm, while the grain boundaries are defined at x = -2 μm, and 2 μm. The probe contact is defined at the top surface from x=3.6 μm to x=4.0 μm Reflecting boundary conditions are applied on the left and right sides of the simulation structure. The device parameters are listed in Table 4.1. Grain boundaries are modeled as 2 nm wide regions with fixed charge. The fixed charge can be considered to come from shallow donor/acceptor independent of common generation level. The relation between charge density and band bending is shown in Table 4.2. The recombination centers in grain boundaries and grain interiors are both using Shockley-Read-Hall model with midgap traps for simplicity. The recombination velocity at GBs is, $S_{GB}=2nm/\tau_{GB}$, where $\tau_n=\tau_p=\tau_{GB}$ in grain boundaries.

If the beam current is 100 pA and beam energy is 5 keV with back scattering coefficient of 0.15, the generation rate in three-dimension system is about $2.9\times10^{26}cm^{-3}/s$. In our simulation, the grain size L is 4 μm. Thus, the equivalent 2D generation rate is estimated to be about 1.8×10^{24} cm^{-3}/s.

For grain boundaries which lead to local depletion or inversion (positively charged for p-type absorber), as shown in Figure 4.1 (a), there is a large enhancement of signal close to the grain boundary, which is consistent with previous experimental observations and numerical simulations [107]. When electron-hole pairs are generated in the depletion region near the grain boundary, electrons can travel in the depletion region to reach the CdS and then the contact. Meanwhile, holes are swept into the p region within grains. Thus, we can conclude that a depletion region near grain boundary aids carrier collections in EBIC imaging experiment. The larger the band bending, the larger the EBIC signal enhancement we observe near the grain boundary as shown in Fig. 4.2 (a).

Table 4.1. Simulation parameters

Bulk Parameters	**CdTe**	**CdS**	**ZnTe**	**SnO_2**
Layer Thickness (μm)	4	0.05	0.05	0.05
Bandgap (eV)	1.5	2.4	2.3	3.6
Electron affinity (eV)	4.4	4.5	3.5	4.8
Doping density (cm^{-3})	p, $5x10^{14}$	n, 10^{17}	p, 10^{17}	n, 10^{17}
$\varepsilon/ \varepsilon_0$	10.6	10	7.4	9
N_C (cm^{-3})	$7.8x10^{17}$	$2.2x10^{18}$	$2.2x10^{18}$	$2.2x10^{18}$
N_V (cm^{-3})	$1.8x10^{19}$	$1.8x10^{19}$	$1.8x10^{19}$	$1.8x10^{19}$
τ_n (ns)	1	10	1	0.1
τ_p (ns)	1-1000	10^{-4}	3	100
μ_n (cm^2/Vs)	320	100	320	100
μ_p (cm^2/Vs)	40	25	40	25

The surface recombination has a large influence on the EBIC signal response. Increased surface recombination would result in reduced EBIC signal as shown in Fig. 4.2 (b), because more generated carriers recombine at the top CdTe surface before they are able to be collected. The maximum collection efficiency for 0.25 eV band bending is about 90% when top surface recombination velocity is small (10^4 cm/s), indicating most of the carriers are collected by probe. The large collection efficiency is because the generation level in the simulation was below the threshold for high level injection effects. When the generation level is high enough, the electrical field in the depletion region will be screened due to the large carrier concentrations and the collection efficiency will drop [106].

For grain boundaries which lead to local accumulation (negatively charged for p-type absorber), as shown in Figure 4.1 (b), the EBIC collection efficiency is very small. This is because there is no channel for minority carrier (electron) current flow in this situation and most of the generated carriers recombine before they reach the probe. The signal contrast between grain boundary region and grain interior is also small. For CdTe with unpassivated grain boundaries, reduction of EBIC signal near grain boundaries is observed because of the increased grain boundary recombination.

Table 4.2. Band bending corresponding to grain boundaries charge density at Y=1 µm (Figure 4.1) for CdTe with 5×10^{14} cm^{-3} p type doping

Band Bending (eV)	**Charge Density (cm^{-3})**
-0.11	-10^{18}
0.10	2.1×10^{17}
0.24	3.6×10^{17}
0.58	6.0×10^{17}
0.94	8.4×10^{17}

4.2 SOLAR CELL SIMULATION

To understand grain boundary impact on CdTe solar cell performance, we conducted further numerical simulation with the same absorber structure plus added ZnTe backside contact. The device structure is shown in Figure 4.4(a) and the device parameters are listed in Table I. AM 1.5 spectrum with an intensity of $1000W/m^2$ is defined for the illumination. The simulation results are shown in Fig. 4.3.

4.2.1 *Depleted Grain Boundary*

Introducing a depleted (positively charged for p-type) grain boundary alters the carrier distribution in the device, changing the recombination rate distribution which is directly related to I_{SC} and V_{OC}. The SRH recombination rate for midgap traps can be expressed as:

$$R_{SRH} = \frac{np - n_i^2}{\tau_p(n + n_i) + \tau_n(p + n_i)} \tag{4.3}$$

When

$$n(x)\tau_p = p(x)\tau_n \tag{4.4}$$

the recombination rate will reach local maximum, which is:

$$R_{SRH}{}^{\max} = \frac{n^2\tau_p/\tau_n - n_i^2}{2\tau_p n + (\tau_p + \tau_n)n_i} \tag{4.5}$$

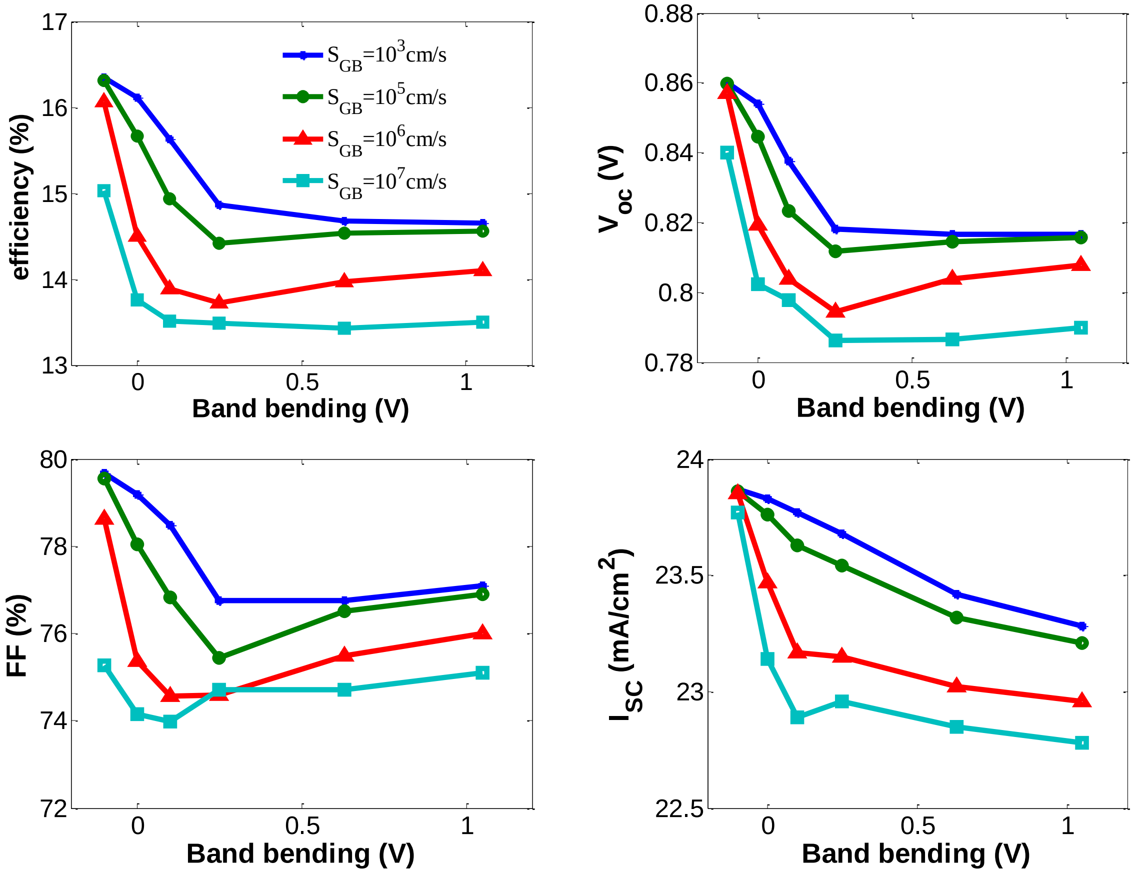

Figure 4.3. Simulated solar cell performance as function of band bending for different grain boundary recombination velocities (S_{GB}). Here positive band bending indicates positively charged (depleted) grain boundary and vice versa. A lifetime of τ_p =3 ns is used in CdTe grain interiors.

The carrier distribution in CdTe cell with depleted grain boundaries is shown in Fig. 4.4(b-c) and Fig. 4.5(b). Band bending brings electron and hole densities closer to each other. When the band bending is large enough, we can observe **local maximum recombination** near grain boundary. We define the recombination in the cell without band bending near grain boundary as reference recombination. Whether the local maximum recombination rate would be larger than the reference recombination rate is determined by the electron/hole density when Eq. (4.4) is satisfied. The larger their values when equation is satisfied, the larger the local recombination, as can be seen from Eq. (4.5).

(a)

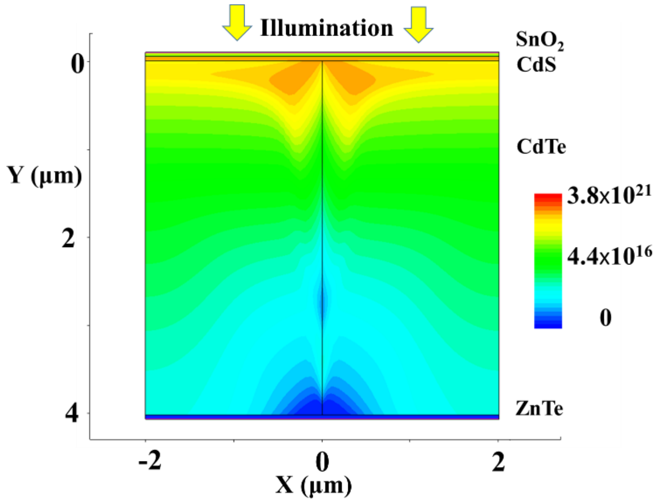

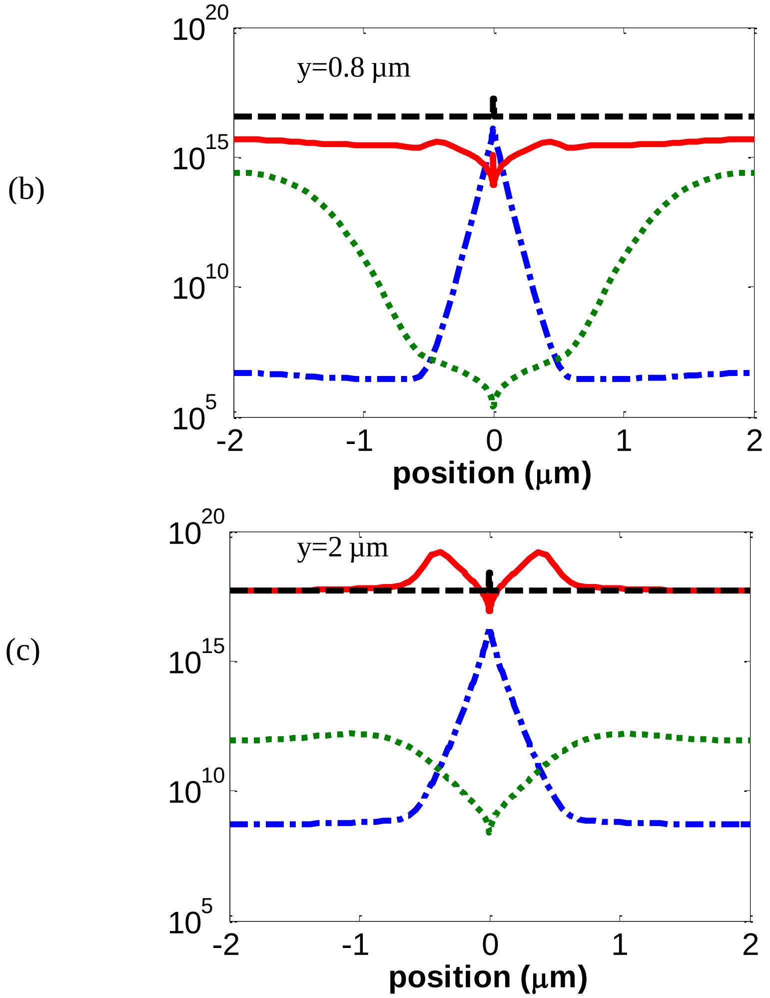

Figure 4.4. Recombination rate (cm^{-3}/s) and carrier density (cm^{-3}) plots for 0.63 eV band bending situation at short circuit condition. (a) is a contour plot of recombination within the simulated structure; (b) give distributions at cutline y=0.8 µm, and (c) is at y=2 µm (near CdS interface). In (b-c), red line is recombination rate, dashed line is reference recombination (no band bending), green line is hole density, and blue line is electron density. $S_{GB}=10^3$ cm/s and τ_p =3 ns in CdTe.

In short circuit situation, the recombination rate at depth 2um from the CdTe/CdS interface reaches local maximum value near the grain boundary (Fig. 4.4(b)). However, when band bending is large enough, the local maximum value is smaller than the reference recombination. This is because carrier concentrations are small (~10^7 cm^{-3}). In addition, the built-in electrical field attracts minority carriers (electrons) from grain interior (GI) to grain boundary (GB) region, which reduces the electron density and thus recombination in GI. The overall trend is that recombination is suppressed when introducing depleted grain boundaries at locations far enough from the CdTe/CdS interface. This is generally explained by carrier separation and leads to an increase in I_{sc} [108, 109].

However, when we move the cutline closer to the CdTe/CdS interface, the local maximum recombination will increase and eventually the overall recombination will be larger than the reference recombination (Fig. 4.4(c)). This is because the heavily doped CdS results in the inversion of adjoining CdTe region. Near the depleted grain boundary, the inversion region is expanded deeper into the absorber. The peak of electron density near the grain boundary broadens and rises near the CdTe/CdS interface. This will increase the electron and hole density when Equation (4.4) is satisfied, which leads to larger local maximum recombination. When the local maximum recombination is large enough, the overall recombination would be enhanced due to introducing depleted grain boundaries.

(a)

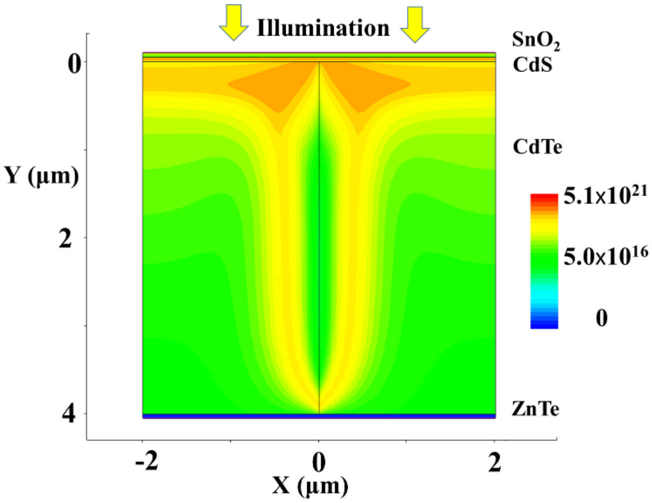

(b)

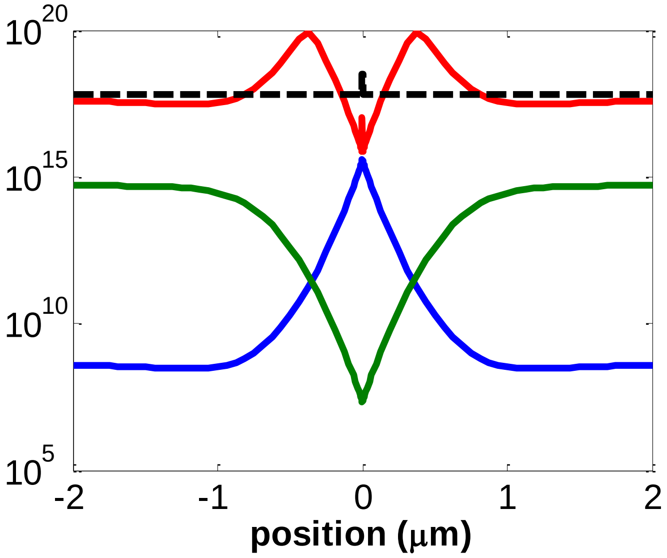

Figure 4.5. Recombination rate (cm^{-3}/s) and carrier density (cm^{-3}) plots for 0.63 eV band bending situation with 0.65 V applied voltage. (a) is a contour plot of recombination; (b) gives distributions at cutline y=0.2 μm. S_{GB}=10^{3} cm/s, τ_p =3 ns in CdTe. Lines are the same as in Fig 4.4

In summary, grain boundaries that lead to local depletion (e.g., positively charged for p-type material) enhance recombination in CdTe cell near the CdTe/CdS interface but suppress the recombination deeper inside absorber. Whether I_{SC} will increase or decrease depends on the balance between the two. For CIGS solar cell with typically heavier doping levels (>10^{16} cm^{-3}), the recombination enhancement region is shallower. Similar to previous research [108, 109], we find an increase of I_{SC} with large enough positive (depletion) band bending. However, in CdTe solar cells, the doping level is relatively low (10^{14}-10^{15} cm^{-3}), so the influence of CdS region extends deep into absorber film, and the depth of recombination enhancement region is larger than in heavier doping scenario. In this situation, we find larger band bending would actually make I_{SC} smaller (Fig. 4.3).

Similar methods can also be applied to analysis of the impact on V_{OC} and efficiency. When applying bias, more minority carriers (electrons) are injected into CdTe region, which raises electron density near grain boundary. When Equation (4.4) is satisfied, the electron and hole density are much larger than those in the short circuit situation, which also makes the local maximum recombination much larger (Fig. 4.5). In our simulation, the local maximum recombination become large enough to enhance the overall recombination, and thus the forward diode current. Combining the small reduction of I_{SC} with the substantial reduction of V_{OC}, results in significant drop in cell efficiency due to positively charged GBs.

Since the ratio between τ_p and τ_n is essential to determining the location of local maximum recombination, the choice of τ_p/τ_n in CdTe could also alter the device performance. $\tau_p/\tau_n \sim 1000$ is used in some previous device simulation [110], while a recent calculation [111] finds that the capture cross-section for electron and hole are on the same order ($\sim 10^{-13}$ cm^{-2}) for native point defects. Thus we conduct simulation using τ_p in CdTe ranging from 1ns to 1000ns while τ_n is fixed to be 1ns, as shown in Fig 4.6. The general trend of reduction of I_{SC} and efficiency with positively charged GBs is still observed in all the different τ_p situations, while the reduction of I_{SC} is significantly mitigated when τ_p is much larger than τ_n. There is almost no dependence of I_{SC} on band bending when $\tau_p \gg \tau_n$ in CdTe. The choices of τ_n and τ_p for SnO_2 and CdS are based on previous work [110].

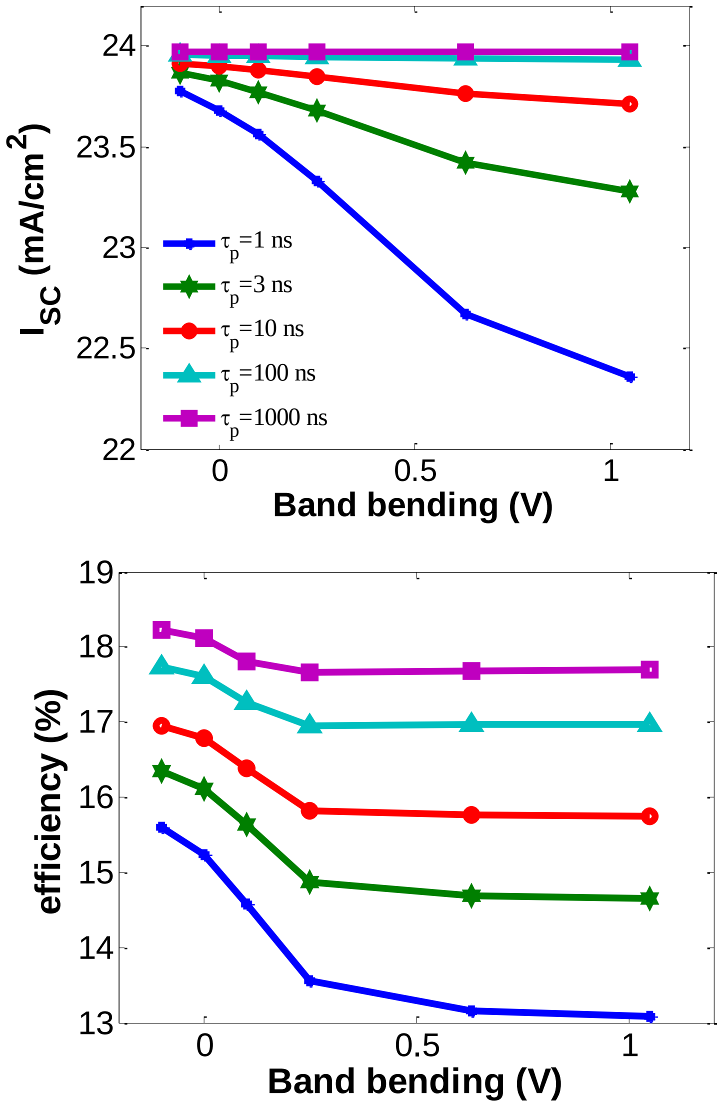

Figure 4.6. Simulated solar cell performance as function of band bending with different τ_p situations in CdTe. τ_n=1ns and $S_{GB}=10^3$ cm/s.

4.2.2 *Accumulated Grain Boundary*

As can be seen from Fig. 4.3 and Fig. 4.6, introducing accumulation (negatively charge) at grain boundaries can enhance the device performance. The upward band bending near the accumulation type grain boundaries would lead to a barrier for electrons to reach grain boundaries. Thus, excess recombination at the grain boundaries would be inhibited in this case, which is consistent with the result that more pronounced performance improvement is found in cells with less passivated grain boundaries. In addition, Accumulated grain boundaries effectively increase the overall doping level for CdTe absorber. Since the active doping level in CdTe is still smaller than the optimal value, increasing the effective doping by introducing accumulation type grain boundaries will also improve the cell performance.

4.3 CONCLUSION

TCAD simulations were conducted for both EBIC imaging and solar cell performance for the same CdTe absorber structure using positively and negatively charged grain boundaries. In the EBIC simulation, we observe signal enhancement near the depleted (positively charged) grain boundary, while solar cell simulations indicate reduction of I_{SC}, V_{OC} and cell efficiency under typical conditions. Based on analysis of the spatial variation in recombination, especially the magnitude and location of maximum recombination, we explain how the grain boundary impacts device performance. The reduction of I_{SC} is opposite that found in previous study of CIGS [108, 109]. This is explained by the large expansion of recombination enhancement region near the CdTe/CdS interface due to the low doping level in CdTe. On the other hand, there is no obvious signal enhancement near accumulated (negatively charged) grain boundaries but the cell performance is improved in this situation. Our study shows clearly that enhanced EBIC signals are not a good predictor of enhanced solar cell performance, and indicates that a passivation process which introduces negative rather than positive charge at grain boundaries could potentially enhance the performance of thin film photovoltaics with p-type absorber layers.

Chapter 5. COMPREHENSIVE MODEL FOR LIGHT INDUCED DEGRADATION IN SILICON SOLAR CELL

Light induced degradation (LID) is a severe problem in boron doped silicon solar cells [112]. Substantial efficiency degradation is seen (up to 10%) due to a decrease of bulk lifetime unpon light exposure as shown in Figure 5.1. A wide range of models have been proposed to explain this phenomenon, but none are fully satisfactory [26, 113-120]. The light induced degradation of boron doped silicon limits conversion efficiency improvements in solar cell. The lifetime degradation was traced at temperature from 20 ^{o}C to 140 ^{o}C while the lifetime would recover to its initial high value after annealing in the dark from 110 ^{o}C and 200 ^{o}C. The lifetime degradation process commonly has two stages: fast stage which happens within 100 seconds and a slow stage which takes up to 10 hours.

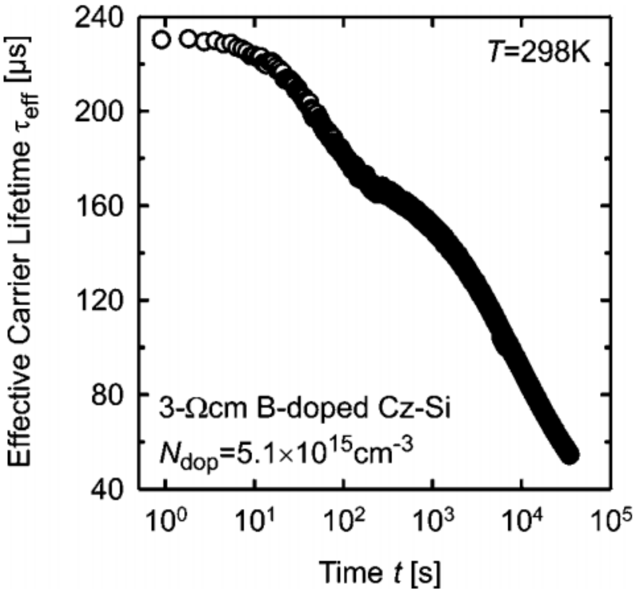

Figure 5.1. The experimental observation for light induced degradation in boron doped silicon solar cell. Reproduced from Ref. [115].

One of the most important parameter to characterize the LID is the normalized defect density，$N_{t,eff}$:

$$V_{th}\sigma N_{t,eff} = \frac{1}{\tau} - \frac{1}{\tau_0} = \left(\frac{1}{\tau_{LID}} + \frac{1}{\tau_0} \right) - \frac{1}{\tau_0} \tag{5.1}$$

Here, τ_0 is the lifetime at initial condition, τ is the lifetime during degradation, and τ_{LID} is lifetime limited by light induced recombination center. If we choose τ_{LID}~ 10^{-5} to 10^{-4} s as shown in Figure 5.1, σ ~ 10^{-14} cm^2 for a neutral defect, and V_{th} ~ 10^7 cm/s, we can estimate $N_{t,\mathrm{eff}}$ is on the order of 10^{11} to 10^{12} cm^{-3} for mid-gap neutral defect.

Initial models accounted for the apparent linear dependence of LID on B doping (as well as quadratic dependence on initial interstitial O) by postulating the formation of complexes between B_s and O_{2i} under light exposure [26, 113-117]. However, experiments using Si co-doped with B and P led to the conclusion that the degradation depends on the hole rather than the B concentration [121-123]. Several new models were proposed to account for the lack of a direct B-doping dependence, but the most widely cited [118-119] relies on the formation of boron interstitial complexes in concentrations that are inconsistent with the fact that (as evidenced by the high solubility of B) B_i complexes are highly unstable in in Si [139] and the proposed defect configurations have no support from *ab initio* calculation [120].

A recent study on Si co-doped with B and Ga has cast doubt on the linear dependence of LID on *p*, as the addition of Ga appears to leave LID unchanged despite the increase in hole concentration [124, 125]. In order to identify a possible explanation for this behavior, we use *ab initio* calculations to identify mechanisms and estimate parameters, leading to a new model which accounts for a wide range of experimental conditions in this chapter. We undertook a series of density functional theory (DFT) calculations which include complexes of not only O and B, but also Ga, leading to a model for LID that accurately accounts for both B/P and B/Ga co-doping. DFT calculations are used to obtain defect levels and transition barriers as well as to identify whether defects are localized recombination centers. The resulting model can match the lifetime for LID quantitatively by using the identified defects and critical parameters from DFT. This chapter is adapted from previous publication [126] and a manuscript to be submitted.

5.1 OXYGEN DIMER FORMATION AND DIFFUSION

We conducted a series of DFT calculation using the VASP code to explore the properties of LID related defects. The calculations for O_2 and BO_2 formation are generally consistent with previous work [26, 117, 127]. The binding energy for two interstitial oxygens to form an oxygen dimer is about -0.30 eV. The two most stable structures are "staggered" with neutral charge (O_2^{st0}) and "square" with double plus charge (O_2^{sq++}). As discussed in previous research [26, 117], light illumination can lead to charge state changes as well as reconfiguration of O_2 between staggered and square structures, which drives oxygen dimer diffusion as shown in Figure 5.2 and 5.3. The reconfiguration barriers are about 0.3 eV for step (3) and about 0.2 eV for step (5), which are much smaller than the normal diffusion barrier (~ 1 eV) in the dark.

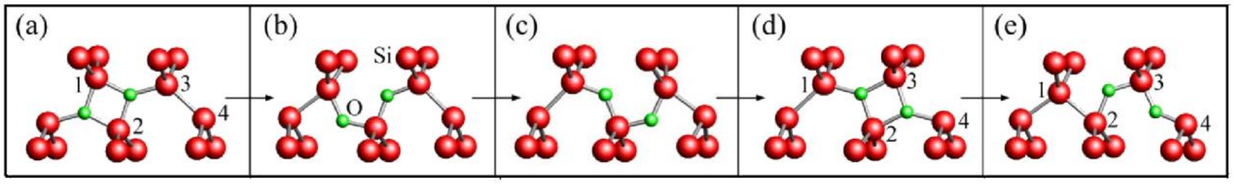

Figure 5.2. O_2 dimer (green) diffusion pathway along a <110> direction. (a) and (d) are the square structures. (b), (c) and (e) are staggered structures. Reproduced from Ref. [26].

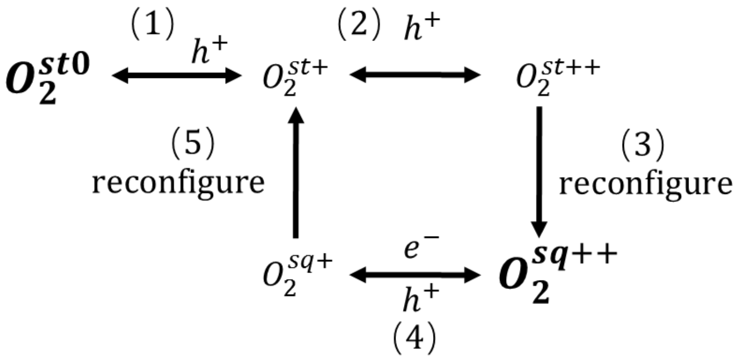

Figure 5.3. Schematic for oxygen dimer reconfiguration during light illumination.

We also calculate the difference of charge density at for oxygen dimers with difference charge states, as shown in Figure 5.4. By comparing the difference in charge density distribution between two charged states of a configuration, we find that O_2^{sq+}/ O_2^{sq++} is localized defects with defect level about 0.2 eV lower than conduction band minimum. For example, when O_2^{sq+} captures hole and become O_2^{sq++}, the previously free hole will be localized close to the O_2^{sq} structure as shown in Figure 5.4. Thus, O_2^{sq} can capture both electrons and holes ((4) in Figure 5.3) and can potentially work as recombination center. However, the hole capture cross-section for O_2^{sq+} is small because of Coulomb repulsion, so it is not expected to be an efficient recombination center. In contrast, O_2^{st0}/ O_2^{st+} is not a localized defect, because the difference in charge density is almost uniformly distributed throughout the system which is similar to a shallow acceptor behavior such as boron in silicon.

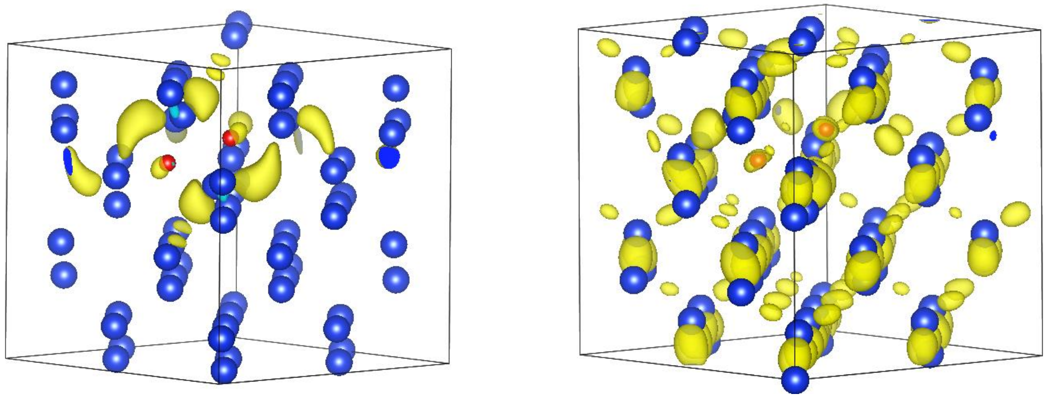

Figure 5.4. Charge density difference for oxygen dimer. The left figure is for square structure and the right figure is for staggered structure. The green red atoms are oxygen and the blue atoms are silicon.

We can write kinetic rate equations for reactions in Figure 5.3 as shown below where we use R$_1$ to R$_5$ to stand for the rates of the steps (1) to (5), respectively:

$$O_{st}^{0} \rightarrow O_{st}^{+} : R_1 = C_{O_{st}^{0}} V_{th} \sigma_0 p - C_{O_{st}^{+}} V_{th} \sigma_0 n_i e^{\left(\frac{E_i - E^t_{O_{st}}}{k_B T}\right)} \tag{5.2}$$

$$O_{st}^{+} \rightarrow O_{st}^{++} : R_2 = C_{O_{st}^{+}} V_{th} \sigma_{same} p - C_{O_{st}^{++}} V_{th} \sigma_{same} n_i e^{\left(\frac{E_i - E^t_{O_{st}}}{k_B T}\right)} \tag{5.3}$$

$$O_{st}^{++} \rightarrow O_{sq}^{++} : R_3 = f \times e^{-E^{reconf}_{O_{st}^{++}/O_{sq}^{++}}/k_B T} \left(C_{O_{st}^{++}} - C_{O_{sq}^{++}} e^{-\Delta E_{O_{st}^{++}/O_{sq}^{++}}/k_B T} \right) \tag{5.4}$$

$$O_{sq}^{++} \rightarrow O_{sq}^{+} : R_4 = C_{O_{sq}^{++}} V_{th} \sigma_{diff} n - C_{O_{sq}^{+}} V_{th} \sigma_{diff} n_i e^{\left(\frac{E^t_{O_{sq}} - E_i}{k_B T}\right)} - \left(C_{O_{sq}^{+}} V_{th} \sigma_{same} p - C_{O_{sq}^{++}} V_{th} \sigma_{same} n_i e^{\left(\frac{E_i - E^t_{O_{sq}}}{k_B T}\right)} \right)$$

(5.5)

$$O_{sq}^{+} \rightarrow O_{st}^{+} : R_5 = f \times e^{-E^{reconf}_{O_{sq}^{+}/O_{st}^{+}}/k_B T} \left(C_{O_{sq}^{+}} - C_{O_{st}^{+}} e^{-\Delta E_{O_{sq}^{+}/O_{st}^{+}}/k_B T} \right) \tag{5.6}$$

In above equations, V_{th} is the carrier thermal velocity ~ 10^7 cm/s, p is the hole concentration and n is the electron concentration, C_X is the concentration of X, E_i is the intrinsic Fermi level, E^t_X

is the defect level of X, $E^{\mathrm{reconf}}_{\mathrm{A/B}}$ is the reconfiguration barrier from A to B, $\Delta E_{\mathrm{A/B}}$ is the energy difference between A and B and f is the attempt frequency ~ 10^{12}/s. σ is the capture cross-section with $\sigma_0 \sim 10^{-14}$ cm^{-2}, $\sigma_{\mathrm{same}} \sim 10^{-16}$ cm^{-2} and $\sigma_{\mathrm{diff}} \sim 10^{-13}$ cm^{-2}. In steady state $R_1=0$ and $R_2=R_3=R_4=R_5$. Thus, we can get the steady state concentration of certain defects at different injection levels, as illustrated in Figure 5.5. The steady state analysis indicates another reason why the oxygen dimer is not a strong recombination center is because the nonlocalized defect O_2^{st0} is the dominant configuration during light illumination.

We also conduct continuum simulations for oxygen dimer formation based on previous modeling of oxygen redistribution and precipitation [37] and find that oxygen dimers are mostly formed during the cool down process from high temperature (> 700 ^{o}C) annealing. As can be seen in Figure 5.6, increasing the ramp rate during cool down, especially in the critical 500-600 ^{o}C range where O_i is still mobile, will reduce the final oxygen dimer concentration. Although there are some arguments about the role of oxygen dimer on LID [128-129], our model to be discussed in later section as well as previous study [130] indicates that LID is proportional to oxygen dimer concentration. Thus, a fast ramp down rate could be used to reduce the impact of LID.

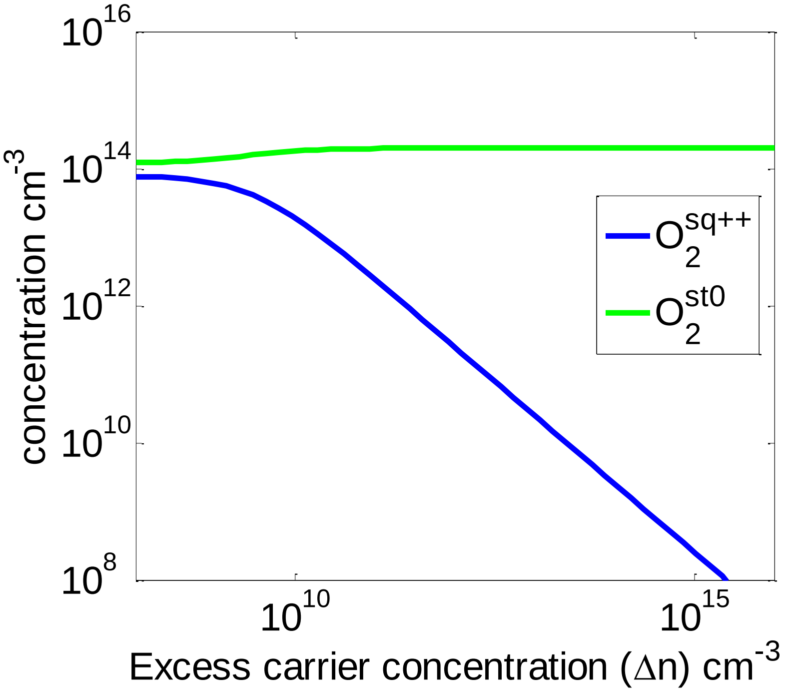

Figure 5.5. The concentration O_2^{sq++} and O_2^{st0} vs excess carrier concentration in steady state in intrinsic Si.

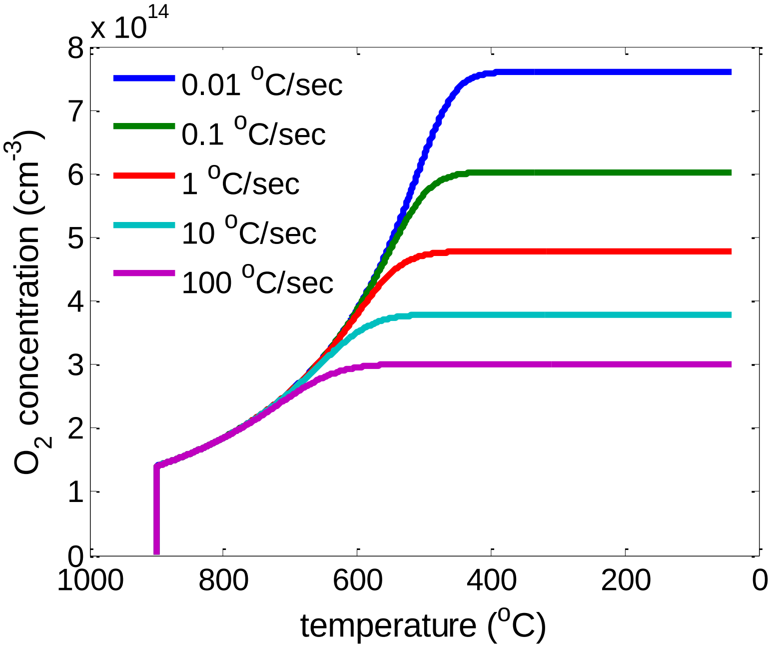

Figure 5.6. Oxygen dimer formation dependence on ramp down rate after annealing at 900 °C for 4 hours. The initial oxygen interstitial concentration is 6×10^{17} cm^{-3}.

5.2 BORON OXYGEN COMPLEXES

There are two possible routes for O_2 capture by substitutional B (or Ga). Using notation of Ref. [127] as illustrated in Figure 5.8, these are labeled A chain and B chain. The A chain is a <110> chain which contains a B_s (or Ga_s), and the B chain is a <110> chain adjacent to a B_s (or Ga_s). Calculations indicate that bistability of staggered and square structures still exists after capture by B_s (Figure 5.7), with a binding energy ($E^b_{B/O2}$) of about -0.42 eV in B chain and about -0.26 eV in A chain.

$$\begin{tikzcd}
\boldsymbol{BO_2^{st-}} \arrow[r, leftrightarrow, "{(6)\ h^+}", "e^-"'] & BO_2^{st0} \arrow[r, leftrightarrow, "{(7)\ h^+}"] & BO_2^{st+} \arrow[d, "{(8)\ \text{reconfigure}}"] \\
 & BO_2^{sq0} \arrow[u, "{(10)\ \text{reconfigure}}"] \arrow[r, leftrightarrow, "e^-", "{h^+\ (9)}"'] & \boldsymbol{BO_2^{sq+}}
\end{tikzcd}$$

Figure 5.7. Schematic for B/O complex reconfiguration during light illumination.

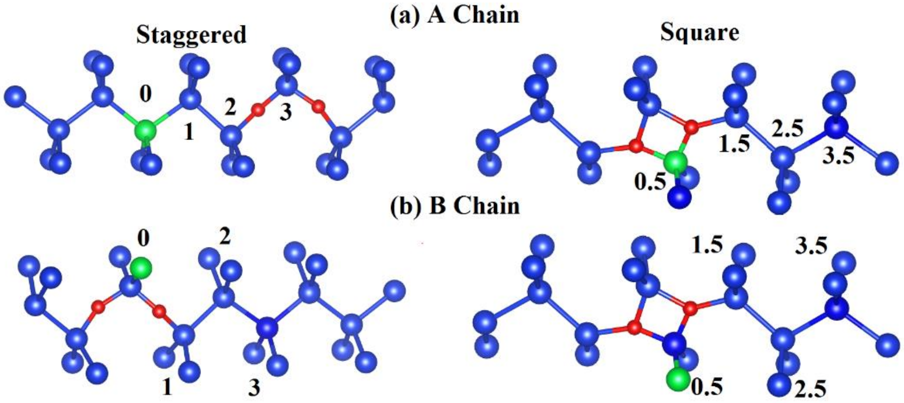

Figure 5.8. Diffusion of oxygen dimer approaching boron (or gallium) in A chain (a) and B chain (b).

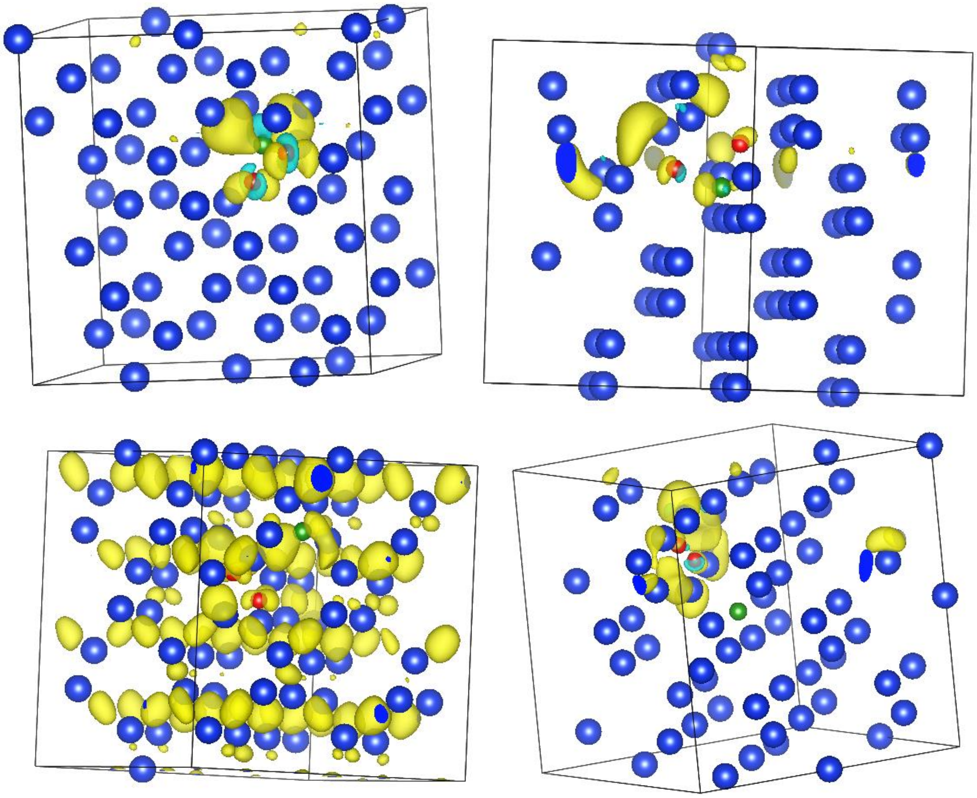

Figure 5.9. Charge density difference for BO2 complex. The upper two are for A chain and the lower are for B chain. The left are for staggered structures and the right are for square structures.

Since the binding energy of oxygen dimer with boron is stronger in B chain, most of the captured dimers are in B chain structure. At equilibrium, the concentration ratio between captured oxygen dimer (C_{BO2}) and free oxygen dimer (C_{O2}) can be expressed as:

$$\frac{C_{BO_2}}{C_{O_2}} = K_{BO_2} C_B, \text{ where } K_{BO_2} = \frac{4}{C_{Si}} e^{-E^b_{B/O_2}/k_B T} \tag{5.7}$$

In Equation (5.7), C_{Si} is the density of silicon lattice sites and 4 comes from the number of possible trap configuration in B chain. At room temperature, with doping $C_B = 10^{16}\text{cm}^{-3}$, the ratio, C_{BO2}/C_{O2}, is about 10, which indicates that most of the oxygen dimers get trapped in B chain. Thus, the equilibrium concentration of BO_2 is mostly determined by the initial oxygen dimer concentration and relatively independent of boron concentration.

Similar to the method used for oxygen dimer, we calculate the charge density difference for boron oxygen complexes as shown in Figure 5.9. We find that $B_sO_2^{sq}$ (both in A chain and B chain) are localized defects with defect level about 0.2 eV lower than conduction band minimum. While $B_sO_2^{st}$ in A chain is localized defect with defect level about 0.2 eV above valence band maximum, $B_sO_2^{st}$ in B chain (low left) is a non-localized defect.

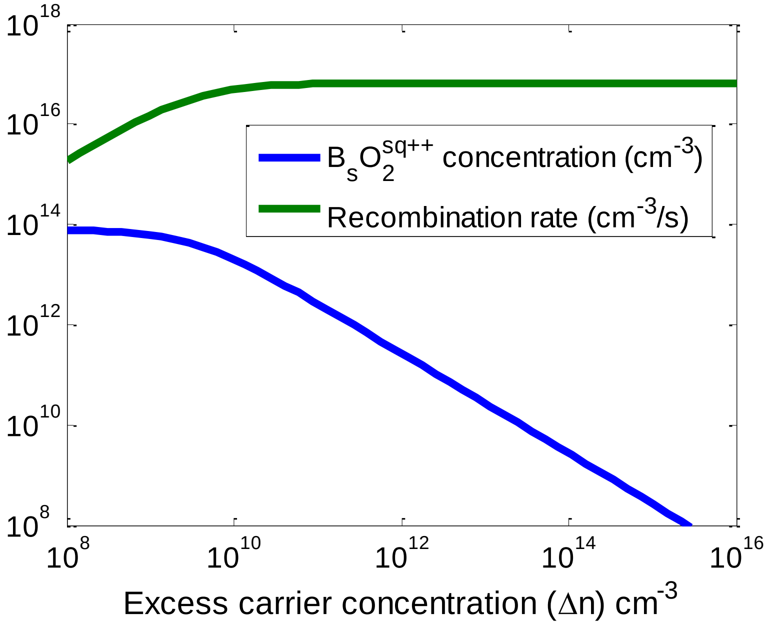

Figure 5.10. The concentration of $B_sO_2^{sq++}$ in B chain and related recombination rate caused by B_sO_2 in B chain vs excess carrier concentration in steady state.

For B chain, the reconfiguration barriers are about 0.25 eV for step (8) and about 0.18 eV for step (10), similar to previous research [26]. We also conducted steady state analyses as for oxygen dimer as shown in Figure 5.10, and find that the non-localized $B_sO_2^{st}$ is the dominant configuration under light illumination, while the concentration of $B_sO_2^{sq}$ is almost negligible. Thus, we believe that although oxygen dimers are mostly trapped in B chain, the associated concentration of localized defect during light illumination is so small that it cannot significantly contribute to LID by itself ((9) in Figure 5.7) or the recombination caused by $B_sO_2^{sq}$/$B_sO_2^{st}$ reconfiguration suggested by [26] ((7) - (10) in Figure 5.7).

For A chain, both staggered and square configurations are localized defects and can work as recombination center for LID. The reconfiguration barriers are about 0.7 eV for step (8) and about 0.12 eV for step (10); The latter value differs from the 0.78 eV barrier calculated in Ref [117]. Based on these calculations, we believe that B_sO_2 in A chain is the primary recombination center. Given the 0.16 eV higher calculated formation energy, the concentration of B_sO_2 in A chain should be about 1/400 of the total B_sO_2 concentration at room temperature. Thus, the density of LID defects (B_sO_2 in A chain) is on the order of 10^{12}cm^{-3}, which matches the typical experimental LID lifetime (10^{-5} to 10^{-4} s) given reasonable capture cross-section (~10^{-14}cm^{2}) and considering the relatively shallow defect level. At low light levels, B_sO_2 in B chain may contribute to the recombination, but under illumination with AM 1.5 spectrum, B_sO_2 in A chain should be the major recombination center. The relative energy and the transition barrier determines whether $B_sO_2^{sq}$ and $B_sO_2^{st}$ in A chain is the main recombination center at a given injection level. Generally speaking, stronger injection would make $B_sO_2^{st}$ more favorable in steady state, and thus more likely to be the primary recombination center.

Because the defect levels for both $B_sO_2^{sq}$ and $B_sO_2^{st}$ are close to band edges, standard trap-assisted recombination theory (Eq. (5.8)) predicts that the recombination rate is proportional to the hole concentration in low to moderately doped p type silicon under low level injection. Using the example of $B_sO_2^{st}$, if $n_i e^{(E_i-E_t)/k_BT} \gg p$:

$$
\begin{aligned}
U &= \frac{pn - n_i^2}{\tau_p(n + n_i e^{(E_t - E_i)/k_B T}) + \tau_n(p + n_i e^{(E_i - E_t)/k_B T})} \\
&\approx \frac{p_0 \Delta n}{\tau_n(n_i e^{(E_i - E_t)/k_B T})}
\end{aligned}
\tag{5.8}
$$

Thus the recombination rate should be proportional to pC_O^2, which is $C_B C_O^2$ for B doped and $(C_B - C_P)C_O^2$ for B/P compensated cases, consistent with previous observations in the absence of Ga [115, 121-123].

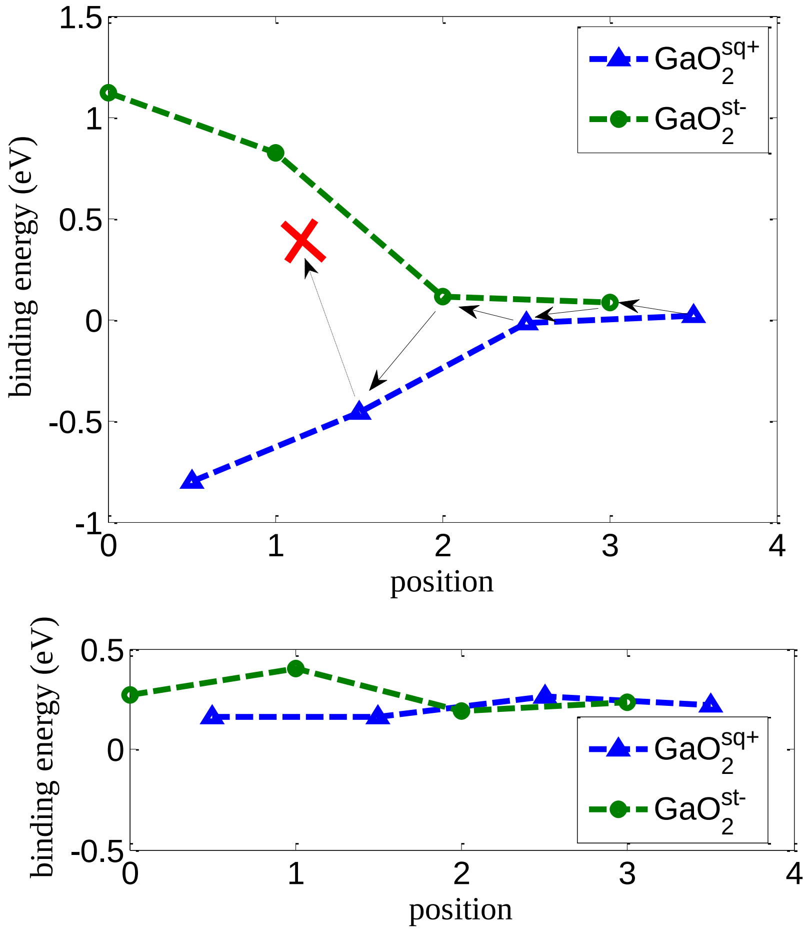

Figure 5.11. Plots of binding energies of Ga_sO_2 complexes in (a) A-chain and (b) B-chain, as a function of atomic distance between the O_2 and Ga, illustrated in Figure 6. The arrows show the diffusion path for oxygen dimer captured by Ga_s. The red cross indicates that O dimer is blocked from moving closer to Ga_s due to strong repulsion for square structure.

5.3 GALLIUM OXYGEN COMPLEXES

We also conduct DFT calculations for the interaction between substitutional Ga and interstitial O_2 dimers. The binding energy between Ga_s and O_2 as O_{2i} approaches is shown in Figure 5.11. We find no significant binding with Ga_s for O_{2i} along B chain. When oxygen dimers diffuse through A chain, there is about -0.46 eV binding ($E^b_{Ga/O2}$) for O_{2i} square structure at second nearest neighbor location. Note that the captured O_{2i} is prevented from moving closer to Ga because of large repulsive energy for staggered structure, presumably caused by compressive strain for the larger Ga atoms. This implies that after being captured by Ga_s, the oxygen dimer no longer retains its bistability, and since the $Ga_sO_2^{sq}$ is a shallow donor and also has smaller hole capture cross-section due to Coulomb repulsion, it cannot work as an effective recombination center.

5.4 MODEL FOR LID

We developed a continuum model to describe the formation kinetics of LID related defects. The involved reactions include:

$$O_i + O_i \leftrightarrow O_2 \tag{5.9}$$

$$B_s + O_2 \leftrightarrow BO_2 \tag{5.10}$$

$$Ga_s + O_2 \leftrightarrow GaO_2 \tag{5.11}$$

We conducted continuum simulation for p type silicon wafer with boron and gallium co-doping. The initial oxygen concentration is 6×10^{17} cm^{-3}. In the simulation, the wafer cools down from 1400 ^oC to room temperature with ramp rate of 2 $^oC/min$, then is held at room temperature for 5 h before light illumination is applied. As illustrated in Figure 5.12, the O dimer concentration increases significantly during the cool down process. Little changes in the dark due to slow O_{2i} diffusion, but binding to B and Ga is strong enough that once diffusion is activated by carrier generation, almost all the oxygen dimers get trapped by B_s or Ga_s. Thus, the acceptor/dimer concentration is the independent of the acceptor concentration.

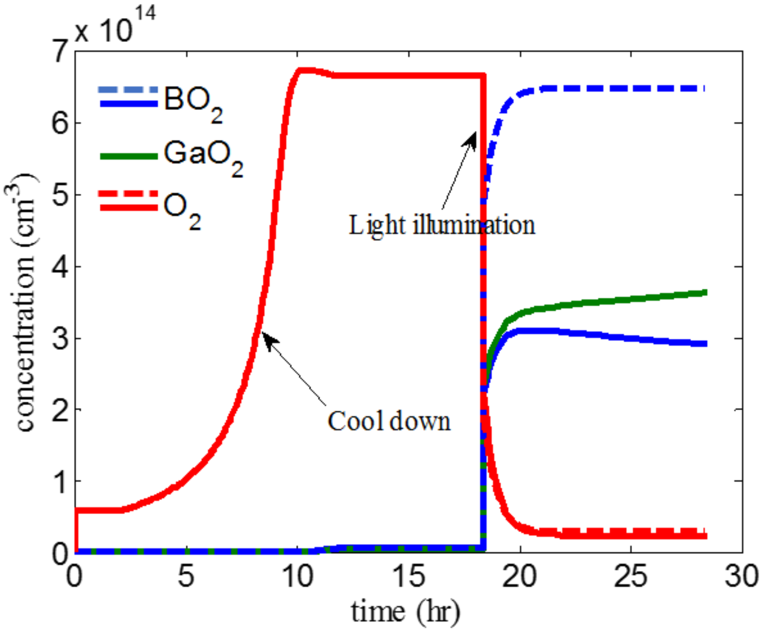

Figure 5.12. Concentration evolution of BO_2, GaO_2 and O_2 during annealing and light illumination. The solid line is for system with 10^{16} cm^{-3} B and 10^{16} cm^{-3} Ga co-doping, and the dashed line is for 2×10^{16} cm^{-3} B doped situation.

If there is B, but no Ga, in our simulation all the oxygen dimers would be trapped by B_s. In this case, the formation of BO_2 complex only depends on the oxygen dimer concentration after cool down and is independent of boron concentration. In the case of B/Ga co-doping we propose a model for LID in which B and Ga compete in the oxygen dimer trapping process. From DFT binding energies, we can estimate the O dimer capture effectiveness ratio between Ga and B (α) to be:

$$\alpha = \exp\left(\frac{E^b_{B/O_2} - E^b_{Ga/O_2}}{k_B T}\right)/2 \tag{5.12}$$

Here the factor of 2 comes from the fact that O_2 is trapped by B_s mostly in B chain, while for Ga_s it can only be captured in A chain. In our calculations, α is about 2 at room temperature and drops as T increases.

As discussed in Section 5.3, GaO_2 is not an effective recombination center. Thus, the concentration of effective recombination center for LID, $N_{\tau,\mathrm{eff}}$, can be expressed as:

$$N_{t,eff} \equiv \frac{1}{\tau_d} - \frac{1}{\tau_0} \propto pC_O{}^2 \frac{C_B}{\left(C_B + \alpha C_{Ga}\right)} \tag{5.13}$$

Here, τ_0 is the initial lifetime and τ_d is the lifetime after LID. For Ga/B co-doping, $p = C_B + C_{Ga}$. If we choose α = 1, then Equation (5.13) becomes $N_\tau \propto C_B C_O{}^2$. This explains the observation in B/Ga co-doped situation, where the LID related recombination rate appears to depend on boron concentration instead of hole concentration [124].

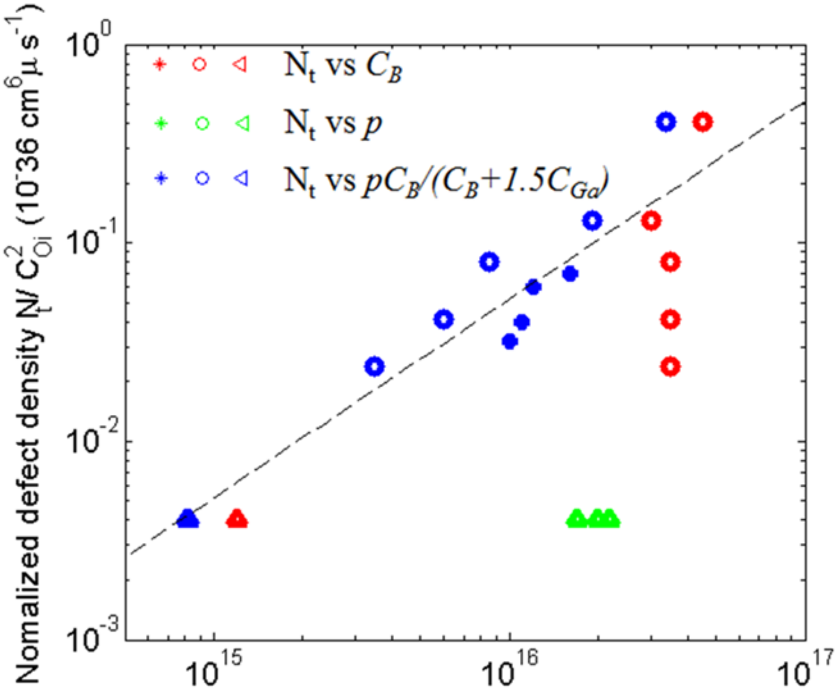

Figure 5.13. Normalized defect density vs C_B, p or $pC_B/(C_B+1.5C_{Ga})$. Stars are for B doping alone [113], circles are for B/P compensated doping [122] and triangles are for B/Ga co-doping [124]. The dashed line is guide to the eye.

In Figure 5.13, we plot normalized defect density data versus boron concentration, hole concentration (p) and our model, which predicts that LID normalized by O concentration squared [124] should be proportional to $pC_B/(C_B+\alpha C_{Ga})$. As can be seen, substantial deviations from linear behavior are seen in the dependence on both p and C_B, but our model can account for the full range of conditions including boron doping alone, B/P compensated doping and B/Ga co-doping.

5.5 CONCLUSION

Using DFT calculation we study the formation of LID related defects, including B/O and Ga/O complexes. Based on the results of these calculations, we propose a comprehensive model to explain experimental observation under the full range of conditions, including both B/P compensated doping and B/Ga co-doping. The key elements of our model are:

i. The trap density is independent of boron concentration because nearly all O_2 are trapped;
ii. The small fraction of O_{2i} captured by boron in A chain is the recombination center for LID;
iii. The hole dependence of recombination rate comes from the shallow defect level;
iv. Ga and B compete in O_{2i} capture process, with nearly compensating effects of increased hole concentration and reduced number of active traps, giving apparent dependence of LID on C_B rather p.

Chapter 6. SUMMARY AND FUTURE DIRECTIONS

In this thesis, we use the multiscale modeling framework to investigate the impact of defect formation in semiconductors on device performance. We conduct *ab initio* calculations to obtain critical parameters and verify mechanisms in defect formation at atomic scale. Then, we develop continuum models at device scale based on the parameters and fundamental insights extracted from atomic simulation. The developed models can be great guidance to optimize device performance and reduce costs. This chapter gives a brief summary of the primary achievements in this dissertation and suggests possible directions for future work.

6.1 SUMMARY

6.1.1 *Carbon Clustering and Associated Metal Gettering*

In Chapter 2, we have developed a moment based precipitation model for carbon based on a series of DFT calculations for different carbon clusters. We also use DFT to investigate the interactions between metal impurities and carbon clusters, which sets the basis for the metal gettering model. The carbon clustering model and metal gettering model together describe how detrimental metal impurities can be removed by the carbon precipitation process. The models can be implemented using commercial TCAD tools, such as Synopsis Sentaurus, and can be used to optimize the processes for advanced Si CMOS image sensors.

6.1.2 *Oxygen Precipitation*

We demonstrate a comprehensive oxygen precipitation model based on the reduced moment precipitation model (RKPM) framework in Chapter 3. In our oxygen precipitation model, we take into account the dynamic incorporation of point defects, the morphology evolution, and the doping dependency, as well as maintaining computational efficiency by using the moment based model. The simulation results are compared to a wide range of experimental data. The developed model can be used for low temperature annealing and fast ramp process to optimize the process conditions.

6.1.3 *Impact of Charged Grain Boundaries on CdTe Solar Cell*

In Chapter 4, we investigate the impact of the charged grain boundaries on EBIC simulation and device performance for CdTe solar cell. In contrast to previous claims, we find that the EBIC measurement is not predictive of device performance. We conduct recombination analysis for our simulation results and propose that passivation processes leading to accumulated type grain boundaries are beneficial to CdTe solar cell performance.

6.1.4 *Model for Light Induced Degradation in Silicon Solar Cell*

In Chapter 5, we conduct DFT calculations for the light induced degradation related defects. We study the formation and diffusion of oxygen dimers, the interaction of oxygen dimers with boron, gallium and phosphorus, and reconfiguration for boron/oxygen dimer complexes. We also investigate the charge density difference for defects with different charge states to identify localized defects. Based on this information from DFT calculations, we propose a comprehensive model which can match a wide range of experimental condition.

6.2 FUTURE DIRECTIONS

6.2.1 *Carbon/Oxygen Precipitation*

Carbon precipitation processes work as a sink for silicon interstitial, while oxygen precipitation ejects interstitials to account for compressive strain. If carbon precipitation and oxygen precipitation occur simultaneously, the two processes will interact with a positive feedback effect. It would be interesting to model carbon and oxygen precipitation together and study the impact each precipitation process has on the other.

6.2.2 *Modeling for CdTe Solar Cell*

There is great interest in diffusion and activation model for Cu in CdTe solar cell. Cu_{Cd} is an acceptor in CdTe and higher doping/activation of Cu would be benefit CdTe solar cell performance. There are proposed reaction/diffusion models for the Cu incorporation process [131]. The study of defects segregation in grain boundaries is also interesting. We can combine the kinetic models with our study of charged grain boundaries, and develop a comprehensive model for the impact of Cu doping/activation, defects segregation, and charged grain boundaries on the device performance.

6.2.3 *Light Induced Degradation*

We have developed a comprehensive model based on the DFT calculation for light induced degradation. We mostly focus on steady-state defect concentrations and propose three possible defects for light induced degradation: BO_2^{sq} and BO_2^{st} in A chain and BO_2^{sq} in B chain. Based on this conclusion, we can study the formation kinetics and injection dependency of LID. It has been reported that hydrogen can be used for the passivation for boron-oxygen defects [132]. It would also be interesting to study its origin and gain fundamental insight from the atomic scale using DFT.

6.2.4 *Study Diffusion Mechanism in Nanoscale*

It’s very important to study the diffusion mechanism at the atomic level. An accurate microscopic diffusion mechanism would increase the reliability of the macroscopic diffusion model. Also, diffusion in the nanoscale may be different from bulk diffusion. There may be great impacts of the surface and quantum confinement effects on nanoscale diffusion. In Ref. [25], we studied the diffusion mechanism of Mn2+ in CdMnSe quantum dot, and concluded that vacancy mediated diffusion is more likely than interstitial mediated diffusion. More DFT calculations at the atomic level are necessary to verify this finding.

6.3 FINAL CONCLUSIONS

This thesis presents a general framework for multiscale modeling. Based on *ab initio* calculations, we can develop continuum models for defect formation. The models can be implemented in processes and device simulations to optimize device performance and reduce costs. This multiscale modeling framework can be a powerful technique to deal with challenges in advanced integrated circuits and photovoltaic industries, and in exploring fundamental physics behind experimental observations.

BIBLIOGRAPHY

[1] M. Gordon. “Cramming more components onto integrated circuits”, *Electronics*, vol. 38, p.114, 1965.

[2] M. Gordon. “Progress in digital integrated electronics”. *IEDM Tech. Dig.,* p.11, 1975

[3] K. Suzuki, K. Suzuki, T. Tanaka, Y. Tosaka, H. Horie, and Y. Arimoto, “Scaling Theory for Double-Gate SOI MOSFET’s”, *IEEE Trans. Electron Devices*, vol. 40, p. 2326, 1993

[4] G. Shahidi, “SO1 Technology for the GHz Era”, *IBM J. Res. Dev*, vol. 46, p. 121 ,2002

[5] D. Hisamoto, W. Lee, J. Kedzierski, H. Takeuchi, K. Asano, C. Kuo, E. Anderson, T. King, J. Bokor, and C. Hu, “FinFET-a self-aligned double-gate MOSFET scalable to 20 nm”, *IEEE Trans. Electron Devices*. vol. 47, p. 2320, 2000

[6] N. Loubet, et al, “Stacked nanosheet gate-all-around transistor to enable scaling beyond FinFET”, *2017 Symposium on VLSI Technology*

[7] K. J. Kuhn, “Considerations for Ultimate CMOS Scaling”, *IEEE Trans. Electron Devices* vol. 59, p. 1813, 2012

[8] S. T. Dunham, *“*A Quantitative Model for the Coupled Diffusion of Phosphorus and Point Defects in Silicon*”, Journal of The Electrochemical Society*, vol. 139, p. 2628, 1992.

[9] S. T. Dunham, A. H. Gencer, and S. Chakravarthi, “Modeling of Dopant Diffusion in Silicon”, *IEICE Trans. Electron*. vol. E82C, p. 800, 1999.

[10] I. Yonenaga, K. Sumino and K. Hoshi, "Mechanical strength of silicon crystals as a function of the oxygen concentration," *Journal of Applied Physics*, vol. 56, p. 2346, 1984.

[11] B. Leroy and C. Plougonven, "Warpage of Silicon Wafers," *Journal of The Electrochemical Society*, vol. 127, p. 96, 1980.

[12] Kwon, Deok-Hwang, et al. "Atomic structure of conducting nanofilaments in TiO2 resistive switching memory." vol. 5, p. 148, 2010

[13] G. Kresse and J. Hafner, “*Ab initio* molecular-dynamics for liquid-metals”, *Phys. Rev. B*, vol. 47, pp. 558, 1993.

[14] G. Kresse and J. Furthmuller, “Efficient iterative schemes for *ab initio* total energy calculations using a plane-wave basis set”, *Phys. Rev. B*, vol. 54, p. 11169, 1996.

[15] R. O. Jones and O. Gunnarsson, “The density functional formalism, its applications and prospects”, *Reviews of Modern Physics*, vol. 61, p. 689, 1989

[16] D. S. Sholl and J. A. Steckel, *Density functional theory a practical introduction*. Hoboken, N.J.: Wiley, 2009

[17] G. Henkelman, B. P. Uberuaga, and H. Jonsson, “A climbing image nudged elastic band method for finding saddle points and minimum energy paths”, *J. Chem. Phys*., vol. 113, p. 9901, 2000

[18] G. Henkelman and H. Jonsson, “Improved tangent estimate in the nudged elastic band method for finding minimum energy paths and saddle points,” *Journal of Chemical Physics*, vol. 113, p. 9978, 2000.

[19] S. M. Sze and K. K. Ng, “Physics of semiconductor devices”, John wiley & sons, 2006.

[20] J. W. Christian, The Theory of Transformations in Metals and Alloys (Part I), 3rd ed., Oxford: Pergamon, 2002.

[21] J. D. Plummer, M. D. Deal, and P. B. Griffin, Silicon VLSI technology: fundamentals, practice, and modeling. Upper Saddle River, NJ: Prentice Hall, 2000

[22] X. Liu, W. Windl, K. M. Beardmore and M. P. Masquelier, “First-principles study of phosphorus diffusion in silicon: Interstitial- and vacancymediated diffusion mechanisms”, *Appl. Phys. Lett*, vol. 82, p. 1839, 2003

[23] S. T. Dunham and C. D. Wu, “Atomistic Models of Vacancy-Mediated Diffusion in Silicon”, *J. Appl. Phys*, vol. 78, p. 2362, 1996

[24] O. Pankratov, H. Huang, T. Rubia, and C. Mailhiot “As-vacancy interaction and ring mechanism of diffusion in Si”, Phys. Rev. B, vol. 56, p. 13172, 1997.

[25] P. Chakraborty, Y. Jin, C. J. Barrows, S. T. Dunham, and D. R. Gamelin, “Kinetics of Isovalent (Cd2+) and Aliovalent (In3+) Cation Exchange in Cd1–xMnxSe Nanocrystals”, *J. Am. Chem. Soc*., 2016

[26] M. Du, H. M. Branz, R. S. Crandall, and S. B. Zhang, “Bistability-Mediated Carrier Recombination at Light-Induced Boron-Oxygen Complexes in Silicon”, *Phys, Rev. Lett*, vol. 97, p. 256602, 2006.

[27] P. A. Stolk, H.-J. Gossmann, D. J. Eaglesham, D. C. Jacobson, C. S. Rafferty, G. H. Gilmer, M. Jaraíz, J. M. Poate, H. S. Luftman, and T. E. Haynes, “Physical mechanisms of transient enhanced dopant diffusion in ion-implanted silicon”, *J. Appl. Phys*, vol. 81, p. 6031, 1997

[28] N. E. B. Cowern, A. Cacciato, J. S. Custer, F. W. Saris, and W. Vandervorst, “Role of C and B clusters in transient diffusion of B in silicon” *Appl. Phys. Lett.*, vol. 68, p. 1150, 1996.

[29] C. H. Poon, A. See, Y. Tan, M. Zhou, and D. Gui, “Suppression of boron deactivation and diffusion in preamorphized silicon after nonmelt laser annealing by carbon co-implantation”, *J. Appl. Phys.*, vol. 103, p.084906, 2008.

[30] M. Uematsu, “Diffusion of co-implanted carbon and boron in silicon and its effect on excess self-interstitials”, *J. Appl. Phys.*, vol. 111, p. 073517, 2012.

[31] H. Wong, N. W Cheung, P. K. Chu, J. Liu, and J. W. Mayer, “Proximity gettering with mega‐electron‐volt carbon and oxygen implantations”, *Appl. Phys. Lett.*, vol. 52, p. 1023, 1988

[32] H. Wong, N. W. Cheung and P. K. Chu, “Gettering of gold and copper with implanted carbon in silicon”, *Appl. Phys. Lett.*, vol. 52, p. 889, 1988.

[33] W. Skorupa, R. Kögler, K. Schmalz, P. Gaworzewski, G. Morgenstern, and H. Syhre, “Iron gettering and doping in silicon due to MeV carbon implantation”, *Nucl. Instrum. Methods Phys. Res. B,* vol. 74, p.70, 1993

[34] Y. Jin and S. T. Dunham, “Modeling of Carbon Clustering and Associated Metal Gettering”, *ECS Transactions*, vol. 64, p.211, 2014

[35] S. T. Dunham, “Modeling of the Kinetics of Dopant Precipitation in Silicon”. *J. Electrochem. Soc*., vol. 142, p. 2823, 1995.

[36] I. Clejan and S. T. Dunham, “A reduced moment based model for precipitation kinetics and application to dopant activation in silicon”, *J. Appl. Phys.,* vol. 78, p. 7327, 1995

[37] B. C. Trzynadlowski and S. T. Dunham, “A reduced moment-based model for oxygen precipitation in silicon”, *J. Appl. Phys.,* vol. 114, p. 243508, 2013

[38] H.-W. Guo, S. T. Dunham, C.-L. Shih, and C. Ahn, in *Proceedings of the International Conference on Simulation of Semiconductor Processes and Devices*, 2006, pp. 71–74, 2006.

[39] G.H. Gilmer, T. Diaz de la Rubia, D.M. Stock, and H. Jaraiz, “Diffusion and interactions of point defects in silicon: molecular dynamics simulations”, *Nucl. Instrum. Methods Phys. Res. B*, vol. 102, p. 247, 1995.

[40] A. Ural, P.B. Griffin, and J.D. Plummer. “Self-Diffusion in Silicon: Similarity between the Properties of Native Point Defects”, *Phys. Rev. Lett*., vol. 83, p. 3454, 1999.

[41] F. Rollert, N. A. Stolwijk, and H. Mehrer, *Mater. Sci. Forum*, 38–41, 753, 1989.

[42] A. R. Bean and R. C. Newman, “The solubility of carbon in pulled silicon crystals” *J. Phys. Chem. Solids*, vol. 32, p. 1211, 1971.

[43] A. C. Tipping and R. C. Newman, “The diffusion coefficient of interstitial carbon in silicon”, *Semicond. Sci. Technol.*, vol. 2, p. 315, 1987.

[44] L. Pizzagalli, G. Cicero, and A. Catellani, “Theoretical investigations of a highly mismatched interface: SiC/Si(001)”, *Phys. Rev. B*, vol. 68, p. 195302, 2003.

[45] S. Isomae, T. Ishiba, T. Ando, and M. Tamura, “Annealing behavior of MeV implanted carbon in silicon” *J. Appl. Phys*., vol. 74, p. 3815, 1993.

[46] A.H. Gencer and S.T. Dunham, “A combined model for {311} defect and dislocation loop evolution: Analytical formulation of kinetic precipitation model”, *J. Appl. Phys.,* vol. 91, p. 2883, 2002.

[47] Schroder, D. K. "The concept of generation and recombination lifetimes in semiconductors." *IEEE Transactions on Electron Device,* vol. ED29, p.1336, 1982.

[48] J. S. Kang and D. K. Schroder, “Gettering in Silicon”, *J. Appl. Phys.*, vol. 65, p. 2974, 1989

[49] A. Borghesi, B. Pivac, A. Sassella and A. Stella, "Oxygen precipitation in silicon," *Journal of Applied Physics*, vol. 77, pp. 4169, 1995.

[50] F. Shimura, H. Tsuya and T. Kawamura, “Thermally Induced Defect Behavior and Effective Intrinsic Gettering Sink in Silicon Wafers”, *Journal of The Electrochemical Society*, vol. 128, p. 1579, 1981.

[51] W. Patrick, E. Hearn, W. Westdorp and A. Bohg, "Oxygen precipitation in silicon," *Journal of Applied Physics*, vol. 50, p. 7156, 1979.

[52] F. A. Ponce, T. Yamashita and S. Hahn, "Structure of thermally induced microdefects in Czochralski silicon after high-temperature annealing," *Applied Physics Letters*, vol. 43, p. 1051, 1983.

[53] T. Ono, G. A. Rozgonyi, C. Au, T. Messina, R. K. Goodall and H. R. Huff, "Oxygen Precipitation Behavior in 300 mm Polished Czochralski Silicon Wafers," *Journal of The Electrochemical Society*, vol. 146, p. 3807, 1999.

[54] H.-D. Chiou and L. W. Shive, “Test methods for oxygen precipitation in silicon*,” VLSI Sci. Technol.* 1985, 429

[55] R. Swaroop, N. Kim, W. Lin, M. Bullis, L. Shive, A. Rice, E. Castel, and M. Christ, “Testing for oxygen precipitation in silicon wafers,” *Solid State Technol*. vol. 3, p.85 ,1987.

[56] G. A. Hawkins and J. P. Lavine, “The effect of rapid thermal annealing on the precipitation of oxygen in silicon,” *J. Appl. Phys*. vol. 65, p. 3644, 1989.

[57] Q. Sun, K. H. Yao, H. C. Gatos, and J. Lagowski, “Effects of nitrogen on oxygen precipitation in silicon,” *J. Appl. Phys*. vol. 71, p. 3760, 1992.

[58] H. Abe, I. Suzuki, and H. Koya, “The effect of hydrogen annealing on oxygen precipitation behavior and gate oxide integrity in Czochralski Si wafers,” *J. Electrochem. Soc*. vol. 144, p. 306, 1997.

[59] D. Kashchiev, “Nucleation: Basic Theory with Applications”, Butterworth-Heinemann, Oxford, 2000.

[60] P. E. Freeland, K. A. Jackson, C. W. Lowe and J. R. Patel, “Precipitation of oxygen in silicon”, *Applied Physics Letters*, vol. 30, p. 31, 1977.

[61] N. Inoue, K. Watanabe, K. Wada, and J. Osaka, “Time-lag in nucleation of oxide precipitates in silicon due to high temperature preannealing”, *Journal of Crystal Growth*, vol. 84, p. 21, 1987.

[62] Frank S. Ham, “Theory of diffusion-limited precipitation”, *Journal of Physics and Chemistry of Solids*, vol.6, p.335, 1958

[63] Frank S. Ham, “Diffusion Limited Growth of Precipitate Particles”, *Journal of Applied Physics*, vol.30, p.1518, 1959

[64] K. Wada and N. Inoue, “Growth kinetics of oxide precipitates in Czochralski silicon”, *Journal of Crystal Growth*, vol. 71, p. 111, 1985

[65] S. M. Hu, “Growth law for disk precipitates, and oxygen precipitation in silicon”, *Journal of Applied Physics*, vol.48, p.115, 1986

[66] W. A. Tiller, S. Hahn and F. A. Ponce, “Thermodynamic and kinetic considerations on the equilibrium shape for thermally induced microdefects in Czochralski silicon”, *Journal of Applied Physics*, vol.59, p.3255, 1986

[67] W. A. Tiller and S. Oh, “The effect of Frenkel defect formation on spherical SiO2 precipitate growth in silicon wafers”, *Journal of Applied Physics*, vol.64, p.375, 1988

[68] J. Vanhellemont and C. Claeys, “A theoretical study of the critical radius of precipitates and its application to silicon oxide in silicon”, *Journal of Applied Physics*, vol.62, p.3960, 1987

[69] S. Kobayashi, "A model for oxygen precipitation in Czochralski silicon during crystal growth," *Journal of Crystal Growth*, vol. 174, p. 163, 1997.

[70] M. Schrems, in Oxygen in Silicon, Semiconductors and Semimetals, Vol. 42, F. Shimura, Editor, Academic Press, New York, 1994.

[71] S. Senkader, J. Esfandyari and G. Hobler, "A model for oxygen precipitation in silicon including bulk stacking fault growth," *Journal of Applied Physics*, vol. 78, p. 6469, 1995.

[72] B. G. Ko and K. D. Kwack, "Growth/dissolution model for oxygen precipitation based on the kinetics of phase transformations," *Journal of Applied Physics*, vol. 85, p. 2100, 1998.

[73] K. Sueoka, M. Akatsuka, M. Okui and H. Katahama, "Computer Simulation for Morphology, Size, and Density of Oxide Precipitates in CZ Silicon," *Journal of The Electrochemical Society*, vol. 150, p. G469, 2003.

[74] K. Sueoka, N. Ikeda, T. Yamamoto and S. Kobayashi, “Morphology and growth process of thermally induced oxide precipitates in Czochralski silicon”, *Journal of Applied Physics*, vol. 74, p. 5437, 1993.

[75] K. Sueoka, “Modeling of Internal Gettering of Nickel and Copper by Oxide Precipitates in Czochralski-Si Wafers”, *Journal of The Electrochemical Society*, vol. 152, p. G731, 2005.

[76] S. Chakravarthi and S. T. Dunham, “A simple continuum model for boron clustering based on atomistic calculations”, *J. Appl. Phys. vol.* 89, p. 3650, 2001

[77] F. R. N. Nabarro, “The Strains Produced by Precipitation in Alloys”, *Proceeding of the Royal Society A*, vol. 241, p. 519, 1940.

[78] J. D. Eshelby, “The determination of the elastic field of an ellipsoidal inclusion and related problems” *Proceeding of the Royal Society A*, vol. 124, p. 376, 1957

[79] J. K. Lee and W. C. Johnson, “Re-examination of the elastic strain energy of an incoherent ellipsoidal precipitate”, *Acta Metallurqica*, vol. 26, p.541, 1978

[80] S. Hahn, F. A. Ponce, W. A. Tiller, V. Stojanoff, D. A. P. Bulla and W. E. Castro Jr., “Effects of heavy boron doping upon oxygen precipitation in Czochralski silicon”, *Journal of Applied Physics*, vol. 64, p. 4454, 1988

[81] S. K. Bains, D. P. Griffiths, J. G. Wilkes, R. W. Series and K. G. Barraclough, “Oxygen Precipitation in Heavily Doped Silicon”, *Journal of The Electrochemical Society*, vol. 137, p. 647, 1990

[82] W. Wijaranakula, “Oxygen precipitation and defects in heavily doped Czochralski silicon”, *Journal of Applied Physics*, vol. 72, p. 2713, 1992

[83] K. Sueoka, M. Akatsuka, M. Yonemura, T. Ono, E. Asayama and H. Katahama, “Effect of Heavy Boron Doping on Oxygen Precipitation in Czochralski Silicon Substrates of Epitaxial Wafers”, *Journal of The Electrochemical Society*, vol. 147, p. 756, 2000

[84] Maria Jose Caturla, Mark D. Johnson and T. Diaz de la Rubia, “The fraction of substitutional boron in silicon during ion implantation and thermal annealing*”, Appl. Phys. Lett.* vol. 72, p. 2736, 1998

[85] Semiconductor Equipment and Materials International, Guide to Conversion Factors for Interstitial Oxygen in Silicon, San Jose, CA, 2002.

[86] M. Schrems, G. Hobler, M. Budil, H. Potzl, and J. Hage, “Calculation of internal gettering sites after double-step and CMOS-type thermal anneals”, *Microelectronic Engineering*, vol.15, p. 57, 1991

[87] Toshiaki Ono, Eiichi Asayama, Hiroshi Horie, Masataka Hourai, Masakazu Sano, Hideki Tsuya and Kiyomichi Nakai, “Behavior of Defects in Heavily Boron Doped Czochralski Silicon”, *Japanese Journal of Applied Physics*, vol. 36, p. L249, 1997

[88] J. C. Mikkelsen, "The Diffusivity and Solubility of Oxygen in Silicon," *MRS Proceedings*, vol. 59, 1985.

[89] S. Senkader, P. R. Wilshaw and R. J. Falster, “Oxygen-dislocation interactions in silicon at temperatures below 700°C:700°C: Dislocation locking and oxygen diffusion”, *Journal of Applied Physics*, vol. 89, p. 4803, 2001

[90] H. Bracht, N. A. Stolwijk and H. Mehrer, "Properties of intrinsic point defects in silicon determined by zinc diffusion experiments under nonequilibrium conditions," *Physical Review B*, vol. 52, p. 16542, 1995.

[91] H. Bracht, H. H. Silvestri, I. D. Sharp and E. E. Haller, "Self- and foreign-atom diffusion in semiconductor isotope heterostructures. II. Experimental results for silicon," *Physical Review B,* vol. 75, p. 035211, 2007.

[92] R. Hull, Properties of crystalline silicon, vol. 20, Institute of Engineering and Technology, 1999.

[93] A. Polian, V.-T. Dung and P. Richet, "Elastic properties of a-SiO2 up to 2300 K from Brillouin scattering measurements," *Europhysics Letters*, vol. 57, p. 375, 2002.

[94] N. Nakayama, H. Matsumoto, K. Yamaguchi, S. Ikegami and Y. Hioki, "Ceramic Thin Film CdTe Solar Cell", *Jpn. J. Appl. Phys*. vol. 15, p. 2281, 1976.

[95] R. W. Birkmire and E. Eser, "Polycrystalline Thin Film Solar Cells: Present Status and Future Potential", *Annu. Rev. Mater. Sci.* vol. 27, p.625, 1997.

[96] I. M. Dharmadasa, "Review of the CdCl2 Treatment Used in CdS/CdTe Thin Film Solar Cell Development and New Evidence towards Improved Understanding", *Coatings*, vol. 4, p.282, 2014.

[97] C. S. Jiang, H. R. Moutinho, R. G. Dhere, and M. M. Al-Jassim, "The Nanometer-Resolution Local Electrical Potential and Resistance Mapping of CdTe Thin Films", *Phot. IEEE J*. vol. 3, p. 1383, 2013.

[98] C. Li, Y. Wu, J. Poplawsky, Timothy J. Pennycook, N. Paudel, W. Yin, S. J. Haigh, M. P. Oxley, A. R. Lupini, M. Al-Jassim, S. J. Pennycook, and Y. Yan, "Grain-Boundary-Enhanced Carrier Collection in CdTe Solar Cells," *Phys. Rev. Lett*, vol. 112, p. 156103, 2014.

[99] I. Visoly-Fisher, S.R. Cohen, A. Ruzin, and D. Cahen, "How polycrystalline devices can outperform single-crystal ones: Thin film CdTe/CdS solar cells," *Adv. Mater.*, vol 16, p. 879, 2004.

[100] S. Smith, P. Zhang, T. Gessert, and A. Mascarenhas, "Near-field optical beam-induced currents in CdTe/CdS solar cells: Direct measurement of enhanced photoresponse at grain boundaries," *Appl. Phys. Lett*, vol. 85, p. 3854, 2004.

[101] M. Tuteja, P. Koirala, V. Palekis, S. MacLaren, C. S. Ferekides, R. W. Collins, and A. A. Rockett, "Direct observation of CdCl2 treatment induced grain boundary carrier depletion in CdTe solar cells using scanning probe microwave reflectivity based capacitance measurements", *J. Phys. Chem. C*, vol. 120, p. 7020, 2016

[102] Y. Jin and S. T. Dunham, Enhanced EBIC response but degraded solar cell performance for CdTe grain boundaries", in *Proc. IEEE 43rd Photovoltaic Spec. Conf.*, 2016. pp. 2188–2190

[103] Y. Jin and S. T. Dunham, “The impact of charged grain boundaries on CdTe solar cell: EBIC measurements not predictive of device performance”, *IEEE Journal of Photovoltaics*, vol. 7, p. 329 ,2017

[104] H. J. Leamy, “Charge collection scanning electron-microscopy”, *J. Appl. Phys*. vol. p. R53, 1982.

[105] C. J. Wu and D. B. Wittry, “Investigation of minority carrier diffusion lengths by electron bombardment of Schottky barriers” , *J. Appl. Phys.* vol. 49, p. 2827, 1978.

[106] P. M Haney, H. P Yoon1, P. Koirala, R. W Collins and N. B Zhitenev, “Electron beam induced current in the high injection regime”, *Nanotechnology*, vol. 26, p. 295401, 2015

[107] H. P. Yoon, P. M. Haney, D. Ruzmetov, H. Xu, M. S. Leite, B. H. Hamadani, A. A. Talin, and N. B. Zhitenev, “Local electrical characterization of cadmium telluride solar cells using low-energy electron beam,” *Sol. Energy Mat. Sol. Cells*, vol. 117, p. 499-504, 2013.

[108] W. K. Metzger and M. Gloeckler, “The impact of charged grain boundaries on thin-film solar cells and characterization,” *J. Appl. Phys*., vol. 98, p. 063071, 2005.

[109] M. Gloeckler, J. R. Sites and W. K. Metzger, “Grain-boundary recombination in Cu(In,Ga)Se2Cu(In,Ga)Se2 solar cells”, *J. Appl. Phys*., vol. 98, p. 113704, 2005.

[110] M. Gloeckler, A. L. Fahrenbruch, and J.R. Sites, “Numerical Modeling of CIGS and CdTe Solar Cells: Setting the Baseline,” in *Proc. 3rd World Conf. Photovolt. Energy Convers*., Osaka, Japan, 2003, p. 491.

[111] C. Buurma, S. Krishnamurthy, and S. Sivananthan, “Shockley-Read-Hall lifetimes in CdTe”, *J. Appl. Phys.*, vol. 116, p. 013102, 2016.

[112] J. Lindroos and H. Savin, “Review of light-induced degradation in crystalline silicon solar cells”, *Sol. Energy Mater Sol. Cells*, vol. 147, p.115, 2016

[113] J. Schmidt and K. Bothe, “Structure and transformation of the metastable boron- and oxygen-related defect center in crystalline silicon,” *Phys. Rev. B*., vol 69, p. 034107, 2004.

[114] K. Bothe, R. Sinton, and J. Schmidt, “Fundamental Boron–Oxygen-related Carrier Lifetime Limit in Mono- and Multicrystalline Silicon”, *Prog. Photovolt: Res*. Appl., vol. 13, p. 287, 2005.

[115] K. Bothe and J. Schmidt, “Electronically activated boron-oxygen-related recombination centers in crystalline silicon,” *J. Appl. Phys.*, vol. 99, p. 013701, 2006.

[116] D. W. Palmer, K. Bothe and J. Schmidt, “Kinetics of the electronically stimulated formation of a boron-oxygen complex in crystalline silicon”, *Phys. Rev. B*., vol 76, p. 035210, 2007.

[117] J. Adey, R. Jones, D.W. Palmer, P. R. Briddon and S. Oberg, “Degradation of Boron-Doped Czochralski-Grown Silicon Solar Cells”, *Phys, Rev. Lett,* vol. 93, p. 055504-1, 2004

[118] V. V. Voronkov and R. Falster, “Latent complexes of interstitial boron and oxygen dimers as a reason for degradation of silicon-based solar cells”, *J. Appl. Phys.* vol. 107, p.053509, 2010

[119] V. V. Voronkov and R. Falster, “Light-Induced Boron-Oxygen Recombination Centers in Silicon: Understanding their Formation and Elimination”, *SOLID STATE PHENOM*. vol. 205-206, p.3, 2014.

[120] V. V. Voronkov and R. Falster, “The nature of boron-oxygen lifetime degrading centres in silicon”, *Phys. Status Solidi C*. vol. 13, p.727, 2016.

[121] D. Macdonald, F. Rougieux, A. Cuevas, B. Lim, J. Schmidt, M. Di Sabatino, and L. J. Geerligs, “Light-induced boron-oxygen defect generation in compensated p-type Czochralski silicon”, *J. Appl. Phys*. vol. 105, p. 093704, 2009

[122] J. Geilker, W. Kwapil, and S. Rein, “Light-induced degradation in compensated p- and n-type Czochralski silicon wafers”, *J. Appl. Phys*. vol. 109, p.053718, 2011

[123] B. Lim, F. Rougieux, D. Macdonald, K. Bothe, and J. Schmidt, ”Generation and annihilation of boron–oxygen-related recombination centers in compensated p- and n-type silicon”, *J. Appl. Phys*. vol. 108, p.103722, 2010

[124] M. Forster, E. Fourmond, F. E. Rougieux, A. Cuevas, R. Gotoh4, K. Fujiwara, S. Uda, and M. Lemiti, “Boron-oxygen defect in Czochralski-silicon co-doped with gallium and boron”, *Appl. Phys. Lett,* vol. 100, p.042110, 2012

[125] M. Forster, P. Wagnera, J. Degoulange, R. Einhaus, G. Galbiati, F. E. Rougieux, A. Cuevasd, E. Fourmond, “Impact of compensation on the boron and oxygen-related degradation of upgraded metallurgical-grade silicon solar cells”, *Sol. Energ. Mat. Sol. Cells,* vol. 120, pp.390, 2014

[126] Y. Jin and S. Dunham, “Interaction of O2i Dimers with Ga in Si and Implications for a Comprehensive Model of Light-Induced Degradation”, in *Proc. IEEE 43rd Photovoltaic Spec. Conf.,* 2017.

[127] X. Yu, P. Chen, X. Chen, Y. Liu, and D. Yang, “Ab-initio calculation study on the formation mechanism of boron-oxygen complexes in c-Si”, *AIP Advances,* vol. 5, pp. 077154, 2015

[128] L. I. Murin, E. A. Tolkacheva, V. P. Markevich, A. R. Peaker, B. Hamilton, E. Monakhov, B. G. Svensson, J. L. Lindström, P. Santos, J. Coutinho, and A. Carvalho, “The oxygen dimer in Si: Its relationship to the light-induced degradation of Si solar cells?”, *Appl. Phys. Lett,* vol. 98, p. 182101, 2011

[129] V. V. Voronkov, R. Falster, K. Bothe, and B.Lim, “Light-induced lifetime degradation in boron-doped Czochralski silicon: are oxygen dimers involved?”, *Energy Procedia*, vol. 38, p. 636, 2013

[130] P. Chen, X. Yu, X. Liu, X. Chen, Y. Wu, and D. Yang, “Experimental evidence of staggered oxygen dimers as a component of boron-oxygen complexes in silicon”, *Appl. Phys. Lett*, vol. 102, p. 082107, 2013

[131] D. Krasikov and I. Sankin, “Defect interactions and the role of complexes in the CdTe solar cell absorber”, *J. Mater. Chem. A*, vol. 5, p.3503, 2017

[132] B. J. Hallam, S. R. Wenham, P. G. Hamer, M. D. Abbott, A. Sugianto, C. E. Chan, A. M. Wenham, M. G. Eadie. And G. Xu, “Hydrogen passivation of BO defects in Czochralski silicon”, *Energy Procedia*, vol. 38, p. 561, 2013

[133] T. Mura. Micromechanics of defects in solids. Springer Science & Business Media, 2013.

[134] A. J. Cohen, P. Mori-Sánchez, and W. Yang, “Insights into Current Limitations of Density Functional Theory”, *Science*, vol. 321, p. 792, 2008

[135] K. Burke, “Perspective on density functional theory”, *J. Chem. Phys*, vol. 136, p. 150901, 2012

[136] E. S. Kryachko, and E. V. Ludeña, “Density functional theory: Foundations reviewed”, *Physics Reports*, vol. 544, p. 123, 2014

[137] S. V. Koveshnikov, and G. A. Rozgonyi, “Iron Diffusivity in Silicon: Impact of Charge State” *Appl. Phys. Lett*., vol. 66, p. 860, 1995.

[138] D. Macdonald, and L. J. Geerligs, “Recombination Activity of Interstitial Iron and Other Transition Metal Point Defects in P- and N-Type Crystalline Silicon” *Appl. Phys. Lett*., vol. 85, p. 4061, 2004

[139] W. Windl, M. M. Bunea, R. Stumpf, S. T. Dunham, and M. P. Masquelier, “First-Principles Study of Boron Diffusion in Silicon”, Phys. Rev. Lett., vol. 83, p. 4345, 1999

APPENDIX A:

GROWTH AND DISSOLUTION RATE FOR DIFFUSION LIMITED PRECIPITATION

The precipitation process can be described using the kinetic rate equations:

$$\frac{\partial f_n}{\partial t} = R_n - R_{n+1} \qquad n = 2,\ 3\dots\ \dots \tag{A.1}$$

$$R_n = g_{n-1} f_{n-1} - d_n f_n \tag{A.2}$$

where g_n is the growth rate from size *n* to *n*+1, d_n is the dissolution rate from size *n* to *n*-1 and f_n is the concentration of size *n* precipitate.

The concentration of solute specie, *C*, is governed by the species conservation equation:

$$\nabla^2 C = 0 \tag{A.3}$$

In spherical coordinate, it becomes:

$$\frac{\partial}{\partial r}\left(r^2 \frac{\partial C}{\partial r} \right) = 0 \tag{A.4}$$

with boundary conditions:

$$C\left(r = \infty \right) = C_\infty \tag{A.5}$$

$$C\left(r = r_n \right) = C_n^i \tag{A.6}$$

where r_n is the radius of the size *n* precipitate and C_n^i is the solute concentration near the precipitate/matrix interface and $C_\infty = f_1$ is the bulk solute concentration.

The solution for equation (A.4) - (A.6) is:

$$C\left(r \right) = C_\infty + \frac{r_n \left(C_n^i - C_\infty \right)}{r} \tag{A.7}$$

The solute diffusion flux at the interface is:

$$\frac{\partial n}{\partial t} = 4\pi r_n^2 D \left.\frac{\partial C}{\partial r}\right|_{r=r_n} = 4\pi r_n D\left(C_\infty - C_n^i\right) = g_n - d_{n+1} \tag{A.8}$$

where *D* is the diffusivity of the solute. Thus, the growth rate can be expressed as:

$$g_n = 4\pi r_n D C_\infty \tag{A.9}$$

The dissolution rate can be obtained by using the equilibrium condition where the growth rate and dissolution rate are balanced:

$$g_{n-1} f_{n-1}^* - d_n f_n^* = 0 \tag{A.10}$$

Here f_n^* is the equilibrium concentration of size n precipitate with the expression:

$$f_n^* = C_S \exp\left(\frac{-\Delta G_n}{k_B T}\right) \tag{A.11}$$

with ΔG_n as the free energy change upon the formation of size *n* precipitate discussed in section (1.2.1). Combining equation (A.10) and (A.11), the dissolution rate is:

$$d_n = g_{n-1} \exp\left(\frac{\Delta G_n - \Delta G_{n-1}}{k_B T}\right) \tag{A.12}$$

APPENDIX B:

CALCULATION FOR STRAIN ENERGY IN INCOHERENT OBLATE SPHEROID INCLUSION

The method we use to calculate the strain energy for oblate spheroid oxygen precipitate in silicon matrix is based on the work by Lee and Johnson [79]. There result is:

$$\frac{W^*}{V} = \frac{1}{2}\varepsilon^2 \frac{K^* c^0}{K^* + c^0} \tag{B.1}$$

where W^* is the strain energy, V is the volume of the precipitate, K^* is the bulk modulus of the precipitate and c^0 is termed as compression modulus with the expression:

$$c^0 = \frac{K\left[\left(S_{1111} + S_{1122} - 1\right)\left(1 - S_{3333}\right) + 2S_{1133}S_{3311}\right]}{\left(S_{1111} + S_{1122} - 1\right)\left(S_{3333} - 2/3\right) + 2\left(S_{3333} - S_{1133} - S_{3311} - 1\right)/3 - 2S_{1133}S_{3311}} \tag{B.2}$$

where S_{ijkl} is the Eshelby tensor [78, 133]. In the case of oblate spheroid inclusion with the principal half axes a_1, a_2 and a_3 (a_1=a_2, a_3/a_1=β), the Eshelby tensor can be expressed as [133]:

$$S_{1111} = \frac{3}{8\pi\left(1-\nu\right)} a_1^2 I_{11} + \frac{1-2\nu}{8\pi\left(1-\nu\right)} I_1, \tag{B.3}$$

$$S_{1122} = \frac{1}{8\pi\left(1-\nu\right)} a_2^2 I_{12} - \frac{1-2\nu}{8\pi\left(1-\nu\right)} I_1, \tag{B.4}$$

$$S_{1133} = \frac{1}{8\pi\left(1-\nu\right)} a_3^2 I_{13} - \frac{1-2\nu}{8\pi\left(1-\nu\right)} I_1, \tag{B.5}$$

$$S_{1111} = \frac{a_1^2 + a_2^2}{16\pi\left(1-\nu\right)} I_{12} + \frac{1-2\nu}{16\pi\left(1-\nu\right)} \left(I_1 + I_2\right), \tag{B.6}$$

$$S_{3333} = \frac{3}{8\pi\left(1-\nu\right)} a_3^2 I_{33} + \frac{1-2\nu}{8\pi\left(1-\nu\right)} I_3, \tag{B.7}$$

$$S_{3311} = \frac{1}{8\pi\left(1-\nu\right)} a_1^2 I_{13} - \frac{1-2\nu}{8\pi\left(1-\nu\right)} I_3, \tag{B.9}$$

where ν is the Poisson ratio. All the other non-zero components can be obtained by cyclic permutation (1,2,3). Here the I terms are defined in terms of standard elliptic integrals. The expression for oblate spheroid is:

$$I_1 = I_2 = \frac{2\pi a_1^2 a_3}{\left(a_1^2 - a_3^2\right)^{3/2}} \left\{ \cos^{-1}\frac{a_3}{a_1} - \frac{a_3}{a_1}\left(1 - \frac{a_3^2}{a_1^2}\right)^{1/2} \right\}, \tag{B.10}$$

$$I_3 = 4\pi - 2I_1, \tag{B.11}$$

$$I_{11} = I_{22} = I_{12} = \frac{\pi}{a_1^2} - \frac{I_1 - I_3}{4\left(a_3^2 - a_1^2\right)}, \tag{B.12}$$

$$I_{13} = I_{23} = \frac{I_1 - I_3}{a_3^2 - a_1^2}, \tag{B.13}$$

$$I_{33} = \frac{1}{3}\left(\frac{4\pi}{a_3^2} - 2I_{13}\right) \tag{B.14}$$

VITA

Ph.D. **Electrical Engineering**, University of Washington, Seattle, WA, USA (2017)

B.S. **Optical Information Science and Technology**, Xi’an Jiaotong University, Xi’an, Shaanxi, China (2012)